NONCONTACT SEISMOCARDIOGRAM SIGNAL DETECTION USING MICROWAVE DOPPLER RADAR

A Dissertation
Presented to
The Academic Faculty

By

Zongyang Xia

In Partial Fulfillment
of the Requirements for the Degree
Doctor of Philosophy in the
School of Electrical and Computer Engineering

Georgia Institute of Technology

May 2020

NONCONTACT SEISMOCARDIOGRAM SIGNAL DETECTION USING MICROWAVE DOPPLER RADAR

Approved by:

Dr. Ying Zhang, Advisor
School of Electrical and Computer Engineering
Georgia Institute of Technology

Dr. Gregory David Durgin
School of Electrical and Computer Engineering
Georgia Institute of Technology

Dr. Omer T. Inan
School of Electrical and Computer Engineering
Georgia Institute of Technology

Dr. Andrew F. Peterson
School of Electrical and Computer Engineering
Georgia Institute of Technology

Dr. Yang Wang
School of Civil and Environmental Engineering
Georgia Institute of Technology

Date Approved: December 19, 2019

Try not to become a man of success, but rather try to become a man of value.

Albert Einstein

To my wife Xiaojing, our upcoming little one, and my family.

ACKNOWLEDGEMENTS

First of all, I would like to express my sincere gratitude to my advisor, Dr. Ying Zhang, for her kind guidance and support throughout my PhD program. Her kindness, patience and enthusiasm helped me to complete the program successfully. I'm honored to join the team and feel lucky to work with Dr. Zhang. This is a beautiful memory in my life.

I would like to thank Dr. Greg Durgin, Dr. Omer T. Inan, Dr. Andrew Peterson, and Dr. Yang Wang for serving on my dissertation committee. Their insightful comments and suggestions have inspired me a lot. I really appreciate the effort and the time they spent on my dissertation.

My sincere thanks also goes to Dr. Tomas E. Brewer and Dr. Allen Robinson, who supported and instructed me to work as a graduate teaching assistant. Thank James Steinberg and Kevin Pham for the equipments and the support in my research work.

Thank my colleagues in the Sensors and Intelligent Systems Lab, including Xiangmin Wei, Zhenhua Xie, Qianao Ju, Ruizhi Chai, Fan Liu, Geng Sun, Manzhan Gu, Yen-Pang Lai, Ayca Ermis, Taeyong Shin, Liangliang Chen, Tun Liu, Hao Cui, Cheng Cheng, Mi Zhou and many others. It is great to work with all of them. Thanks for the discussions and the contributions to my research. Thank Andrew Carek, Md. Mobashir Hasan Shandhi and Cheng Qi for the cooperation of research works. I would also like to thank my friends Yuzheng Liu, Xinwei Chen, Zhen Wang, Liangbei Xu and Long Gao. I enjoy the days we spent together, and all the fun we have had.

Most of all, I would like to thank my family: my parents, my elder sister, my elder brother, and my wife. Thanks for the great support in pursuing my doctorate degree spiritually and financially. Their endless and deep love encourages and empowers me to move forward. I owe a lot of gratitudes to them. Special thanks to my wife Xiaojing Shao and our upcoming little one. It is their companion that supports me throughout writing this thesis.

TABLE OF CONTENTS

LIST OF TABLES

LIST OF FIGURES

LIST OF ABBREVIATIONS

AC	Aortic Valve Closure
ADC	Analog to Digital Converter
AO	Aortic Valve Open
BBI	Beat to Beat Interval
BCG	Ballistocardiogram
CFT	Complex Fourier Transform
CW	Continuous Wave
DAQ	Data Acquisition Unit
ECG	Electrocardiogram
FIR	Finite Impulse Response
FMCW	Frequency Modulated Continuous Wave
ICG	Impedance Cardiogram
IF	Intermediate Frequency
LDV	Laser Doppler Vibrometry
LO	Local Signal
LPF	Loop Filter

LVET	Left Ventricular Ejection Time
PEP	Pre-ejection Period
PFD	Phase Frequency Discriminator
PID	Proportional-Integral-Derivative
PLL	Phase Locked Loop
PRAE	Peak of RAE Signal
PRDH	Peak of RDH Signal
RAE	Envelope of Radar Acceleration Waveform
RAW	Radar Acceleration Waveform
RCG	Radarcardiogram
RDH	Radar Displacement Signal of Heartbeat
RMSD	Root Mean Square Deviation
SCG	Seismocardiogram
$\mathbf{SCG_{DV}}$	Dorso-Ventral SCG
SFCW	Stepped Frequency Continuous Wave
SNR	Signal to Noise Ratio
SNS	Sympathetic Nervous System
STCW	Single-Tone Continuous Wave
STD	Standard Deviation
STI	Systolic Time Interval

SYNC	Synchronization Signal
UWB	Ultrawideband
VCO	Voltage Controlled Oscillator

SUMMARY

With a growing interest in developing the non-contact detection of vital sign such as the cardiac signals, the microwave Doppler radar system has been a promising remote sensing technique. How to acquire an accurate and reliable cardiac signal and what kind of signal can be acquired from the radar system becomes a problem. The objective of the thesis is to design a microwave Doppler radar system with high signal quality, reduced interference, and explore and extract the cardiac signal features from the radar signal.

A noise suppression scheme and a clutter removal strategy are investigated to improve the performance of a microwave Doppler radar system for detecting an accurate and reliable cardiac signal. It is demonstrated that the proposed noise suppression scheme consisting of dual carriers and a phase locked loop could reduce the noise level and improve the signal to noise ratio by 12 dB. In addition, the clutter removal strategy through a frequency modulated continuous wave radar system is implemented for improving the signal accuracy.

Further investigations on what kind of cardiac signals can be captured by the radar system are conducted, which demonstrate that the radar acceleration waveform (RAW) exhibits a high similarity to seismocardiogram (SCG) in morphology and timing features within the frequency band 18-35 Hz and prove the effectiveness of RAW in representing SCG features. In addition, to achieve complete non-contact detection and monitoring of cardiac signals, a method is developed to independently extract cardiac features from RAW without using a contact electrocardiogram (ECG) sensor as that conventional SCG feature extraction methods rely on.

The investigations have demonstrated that a robust, reliable and accurate cardiac signal detection and monitoring can be realized with a complete non-contact system based on microwave Doppler radar. The improved system is promising for the applications in health care, physical measurement and biomedical monitoring, and may provide a new enabling technology for disease diagnosis and evaluation in the future.

CHAPTER 1
INTRODUCTION

The growing interest in developing health monitoring systems has attracted lots of attentions in the daily health care and medical diagnosis. In addition to the traditional contact measurement approach, there is an increased need for comfortable and unobtrusive detection devices and less professional skills required to operate, especially for the patients and customers who prefer simple and easy operations.

1.1 Background and Motivation

With the development of remote sensing techniques, non-contact systems are designed to provide convenient measurements of health information without requiring the expertise skills or seeing a doctor. Various sources could be utilized to remotely acquire the cardiac information from human subject, such as lasers, cameras, ultrasounds and radars, which are promising for the non-contact detection of cardiac signals. The advances of wireless technology and on-board system make these non-contact systems be suitable for practical applications in small size and at a low cost.

Lots of attentions are paid to microwave Doppler radar system for cardiac signal detection, which is referred to remote sensing of cardiac signals using microwave Doppler radar. Due to the ability to penetrate through non-metal obstacles, microwave Doppler radars are able to achieve excellent privacy and unobtrusiveness during detection.

Compared with conventional contact systems, the non-contact radar system still faces challenges in system reliability, signal accuracy, and the capability of acquiring effective cardiac information.

1. **System reliability and signal accuracy:** The radar system is expected to detect an effective signal relying on the radar reliability and signal accuracy. Radar noise, inter-

ference, and other problems resulting from the detection principle play important roles in signal reliability and accuracy. The development of microwave Doppler radar system is necessary to reduce noise and interference which are the critical issues for an accurate and effective signal detection.

2. **Effective cardiac signal:** As an effective and efficient non-contact approach, the radar system is desired to capture effective cardiac information in addition to respiration and heartbeat rates. Different from the contact system that detects a desired signal from a specified location, radar system acquires human cardiac activity from an area of human skin surface. Studies need to be conducted to investigate what cardiac information can be extracted from the radar signal. Additionally, the algorithms for automatically extracting critical cardiac features need to be developed for estimating the cardiac condition and predicting health condition of a human subject.

The objective of the research is to overcome the above-mentioned challenges to achieve non-contact detection of cardiac signal using microwave Doppler radar system, which can enable the complete non-contact detection and evaluation of cardiac healthiness.

1.2 Related Work

The non-contact cardiac detection of human subjects has attracted lots of attention for the past several decades and it is still a promising technique in the future applications. In this chapter, a brief overview for the research topic is presented in the following parts: (1) non-contact cardiac detection systems; (2) challenges of microwave Doppler radar; and (3) cardiac information detection.

1.2.1 Non-contact Cardiac Detection Systems

Various wireless solutions have been developed to achieve the non-contact detection of cardiac signals. In this section, we compare them to choose the approach that better suits for the cardiac detection. The non-contact systems to be discussed include laser Doppler

vibrometry (LDV) and microwave Doppler radar.

Laser Doppler Vibrometry

LDV has been used to remotely measure the cardiac information with high accuracy and the high frequency of the lasers provides extremely high resolution [1, 2]. Thus, LDV can be a very good approach for the non-contact detection of cardiac information. However, the commercial LDV equipment makes it a relatively expensive technology. Additionally, the laser technology suffers from the fact that the light cannot penetrate through obstacles, which makes it unable to detect the cardiac activity under the clothes or behind obstacles.

Microwave Doppler Radar

For achieving non-contact detection, the radar system also attracts the attention, due to its capability of remote sensing and penetration through obstacles [3, 4]. This provides the radar system the advantage of eliminating obtrusiveness for patients and working under environments with obstacles. Multiple radar systems are developed to implement the cardiac signal detection, such as single-tone continuous wave (STCW) [5], stepped frequency continuous wave (SFCW) [6], frequency modulated continuous wave (FMCW) [7, 8] and impulse-based ultrawideband (UWB) [9] radar systems. These systems utilize the Doppler effect of microwave signals on the human chest wall, and they are called microwave Doppler radars. Since the cardiac activities of human subject cause vibrations on the skin surface, especially the chest wall where vibrations are more obvious, the microwave Doppler radar systems could acquire the cardiac information through detecting these vibration signals.

As the chest wall vibrations can represent the vital sign signals including the respiration and the cardiac activities, the most obvious information that can be extracted from the microwave Doppler radar is the respiration and heartbeat rates [10, 11, 12]. Droitcour *et al.* have analyzed the detection of heartbeat rate from the Doppler radar signals [13, 14].

During the reflection on the chest wall, the phase of microwave signals are changed by the reflection and surface vibration. Generally, the reflection from a surface introduces a constant change of phase, but the surface vibration periodically modulates the phase. The phase demodulation of microwave signal produces a baseband signal or the radar displacement signal that could exhibit the surface vibration, thus the cardiac activities.

The traditional demodulation process adopts the small angle approximation [15], which can provide a good representation of cardiac signal. However, this brings the null problem [16], which means the signal from the small approximation might be zero at some distances. To overcome the null problem, complex Fourier transform [17] and arctangent demodulation [18] are developed with the demodulator performing the I/Q demodulation, which could stably exhibit the cardiac signal from any distance.

Compared with LDV, microwave Doppler radar system could be a promising technique for remote sensing of cardiac signals, especially the capability of penetrating obstacles, providing a non-contact detection with privacy and unobtrusiveness.

1.2.2 Challenges of Microwave Doppler Radar System

The significant challenges involved in the radar system are the translation of oscillator phase noise and clutter interference. The quality and accuracy of the weak cardiac signal is easily influenced by the noise and interference. These two challenges in the radar system are discussed: (1) the noise issue of radar system and (2) clutter interference in the radar detection.

Noise Issue of Radar System

Noise performance of the non-contact cardiac signal depends on the phase noise of the microwave carrier signal and the receiver noise. Droitcour *et al.* indicated the range correlation effect on residual phase noise is obvious in the short range [15] and could reduce the noise influence. However, this approach is not effective for long distance detection, as

the phase coherence between the received and local wave signals is significantly decreased, especially under hostile environment.

The phase-locked loop (PLL) is another promising method to suppress noise, and a vital sign sensor based on PLL in combination with the body proximity effect has been proposed [19, 20]. It can effectively enhance the detection sensitivity by suppressing the phase noise of the received microwave signal, and reliably detect the cardiac signal in extreme and hostile environments. However, large temperature variations during detection may influence the detection accuracy and its working range is limited to several centimeters.

According to the above discussion, noise performance in the cardiac signal detection remains to be a problem for the microwave Doppler radar system. Especially for the long range detection, the detection sensitivity and reliability are significantly influenced by the noise.

Clutter Interference in Radar Detection

In addition to the noise issue, the microwave Doppler radar system suffers from the clutters which are the microwave signals reflected from the backgrounds. They deteriorate the efficiency of power amplifier at the receiver, and degrade the signal quality and accuracy [18, 21, 22], which may even lead to loss of the capability of tracking the signals.

Narrow band Doppler high-pass filters are proposed to mitigate the stationary clutter [23]. However, the high requirement on the filters lead to high complexity in the design.

Negative feedback scheme can cancel the clutters automatically. The scheme based on microprocessor control unit is robust and automatic but might be limited to the continuous wave radar systems [24]. A clutter canceler consisting of an adjustable attenuator and phase shifter is implemented for a continuous wave radar system operating at 60 GHz [21]. The clutter cancellation enhances the detecting sensitivity at distances of 1 and 2 meters. However, the clutter canceler needs to be manually adjusted each time before the detection, which is inconvenient in practical applications.

The range discrimination enables the FMCW radar to have the range-isolation capability [23], and the radar can separate signal from clutters reflected from other distances. But clutters from the same distance of signals cannot be removed, and they might have an obvious effect on the signal quality, which needs to be evaluated to determine the influence.

Clutter interference is still a challenge for the microwave Doppler radar system, and a system with automatic control and good clutter removal performance is desired to improve the detection accuracy.

1.2.3 Extraction of Cardiac Information

Based on the improved microwave Doppler radar system, radar displacement signal can be successfully and accurately detected. Further analysis can be implemented to explore more detailed information from radar displacement signal. In this section, we demonstrate the cardiac information detection in two parts: (1) cardiac information from radar signal; and (2) independent feature extraction.

Exploration of Cardiac Signals from Radar

The exploration of radar displacement signal reveals that it has the potential to demonstrate more cardiac information, such as the conventional ballistocardiogram (BCG), impedance cardiogram (ICG) and SCG. Though radar displacement signal is theoretically confirmed to represent information related to cardiac activities, the relationship between radar displacement signal and the contact sensor signal needs to be verified.

Geisheimer and Greneker measured the displacement cardiography using high sensitive radar and obtained the body motion caused by the beating heart [25]. The radar output signal named radarcardiogram (RCG) has nearly all useful information below 30 Hz, which is the same band of BCG signal. However, they have low similarity in morphology and display different features.

Besides BCG, Thijs *et al.* compared radar displacement signal obtained from a contin-

uous wave Doppler radar sensor with an ICG to analyze the mechanical activity of heart [26]. The radar displacement signal and ICG show similarity of feature point locations, and even better similarity of feature points can be achieved between ICG and the derivative of radar displacement signal. Further assessment of radar and ICG signals indicates the feasibility of representing ICG using radar displacement signals. But the radar sensor still needs to be positioned directly on the body surface, and there are substantial morphological differences between radar displacement signal and ICG.

A big step for analyzing radar displacement signal is finding its relationship with SCG. The radar displacement signal contains the displacement of chest wall induced by heartbeat, while SCG exhibits local vibrations of chest wall in response to heartbeat. As SCG is an acceleration signal, the second derivative of radar displacement signal may represent the similar SCG feature. Mazlouman [27] and Tavakolian [28] reported that the differentiation of the radar displacement signal, which was recorded by a Doppler radar system operating at 2.45 GHz and 10 centimeters away from the chest wall, has a close relationship to the SCG measured using an accelerometer after band pass filtered between 4 Hz and 20 Hz. Based on the morphology comparison between the radar acceleration waveform (RAW, the differentiated radar displacement signal) and SCG, they claimed that, with further development, it would be possible to extract all SCG features from the RAW, which would enable hemodynamic parameter extraction from either the amplitude or timings of radar signal. In addition, they claimed that S1 and S2 sounds of the phonocardiograph signal, which represents systolic and diastolic phases, correspond to similar complexes on the radar displacement signal. Although no further thorough investigation was presented to verify some claims in [27] and [28], Mazlouman and Tavakolian have shown that microwave Doppler radar has the potential to acquire the SCG-like signals that may be used to extract the SCG feature to evaluate the cardiac activity.

Though RAW is claimed to have high similarity to SCG, further investigation is needed to verify its effectiveness in representing SCG.

Standalone Feature Extraction

The claimed similarity of RAW to SCG indicates that microwave Doppler radar may acquire SCG characteristics remotely, and motivates the investigation of independently extracting SCG feature from RAW to achieve complete remote sensing of cardiac conditions. Traditional analysis of SCG requires the R peaks of electrocardiogram (ECG) as reference points [29, 30, 31] to segment SCG beats and extract the features. ECG is an important reference for RAW analysis, but it requires contact measurement.

To achieve the complete non-contact detection of SCG features from RAW, ECG should not be used as the reference. Khosrow-Khavar and Laurin *et al.* designed a delineation algorithm that could automatically detect specific fiducial points of SCG without using the ECG R-peak as the reference point [32, 33, 34, 35]. These fiducial points are indicators of the cardiac states and can be used to estimate the cardiac timing features [36]. But the complexity and sensitivity of SCG bring difficulty to robust and reliable extraction of the features, thus the algorithm disregards the low quality cardiac cycles before extracting fiducial points. However, for the RAW from the radar system, many cardiac cycles have relatively poor quality, especially under the involuntary body movements. Thus, the delineation algorithm may have limited performance for the RAW and fail to recognize many fiducial points.

The standalone feature extraction from RAW without concurrent ECG remains to be a significant challenge due to the relatively low signal quality of RAW. To achieve a complete non-contact detection, a robust and reliable delineation algorithm needs to be developed.

1.3 Research Objective and Main Contribution

Based on the discussions above, the non-contact detection of SCG using the microwave Doppler radar still faces challenges in the system performance and the acquisition of the cardiac features. It is desired to design a robust and reliable Doppler radar system and

develop a method to automatically extract cardiac features from the radar baseband signal.

In this thesis, the hardware design and the signal processing methods are developed to improve the system detection performance and to achieve the remote cardiac feature acquisition, respectively. The following contributions are claimed for the thesis.

1) A noise suppression scheme is designed to reduce the noise in the radar system and the microwave transmission path. A PLL and dual carriers are adopt to complete the noise extraction and suppression. The noises are suppressed through one carrier, then the other carrier can detect the signals with low-noise. Experimental analysis shows the scheme improves the signal to noise ratio (SNR) by about 12 dB at 10-Hz frequency offset, and increases the detection distance.

2) Clutter removal strategies are discussed and experimentally demonstrated to eliminate the clutters which contain no effective information but degrade the signal quality. The FMCW radar can significantly remove clutters with an increased frequency bandwidth, which narrows the range resolution and isolates the clutters outside the resolution range. At the bandwidth of 4 GHz, the spectrum and the transient cardiac signals can clearly demonstrate the cardiac features, such as the heartbeat rates and the systolic and diastolic profiles.

3) An investigation is conducted to experimentally verify the similarity of RAW to SCG. In the frequency band 18-35 Hz, the RAW and the dorso-ventral SCG (SCG_{DV}) have cross correlation coefficients over 0.90 for 5 of 8 subjects, representing high similarity in morphology. Additionally, the RAW can correctly provide the location of the aortic valve opening (AO) point, and estimate the decrease of pre-ejection period (PEP) due to physiological perturbation.

4) A delineation algorithm is developed to extract the SCG feature from RAW without concurrent ECG, so that the completely non-contact detection and analysis of SCG can be achieved. Instead of ECG, a radar displacement signal of heartbeat (RDH) is derived to locate the systolic profiles and search for the AO point. The RDH-based approach can

detect the AO with an average detection ratio of 79%. The left ventricular ejection time (LVET) and beat to beat interval (BBI) can also be estimated from the RDH-based approach with high accuracy.

1.4 Organization of the Thesis

The organization of the thesis is as follows: Chapter 2 demonstrates a noise suppression scheme for the microwave Doppler radar system in the cardiac detection; Chapter 3 discusses the effectiveness of RAW in representing SCG; Chapter 4 illustrates the standalone SCG feature extraction from RAW without concurrent ECG. Finally, the clutter effect on the RAW and the scheme for clutter removal are analyzed and experimentally verified in Chapter 5. And the conclusions and the future work are listed in Chapter 6.

CHAPTER 2

NOISE SUPPRESSION FOR ACCURATE RADAR SIGNALS

A single-tone microwave Doppler radar system could penetrate through the non-metal obstacles, and provide remote sensing of the vital sign signals such as the heartbeat and respiration signals. The simple structure and high detection resolution enhance its practicability in the applications. Additionally, remote sensing brings great convenience for the signal detection and eliminates the obtrusiveness during the detection. However, the detected signals are subject to interference and degradation due to the phase noise of the microwave carrier in the radar system. It is desired to design a noise suppression scheme to improve the detection sensitivity and the signal quality, and thus enable the radar system to work at a long distance.

The rest of this chapter is organized as follows. Section 2.1 analyzes the vital sign detection through a microwave Doppler radar, and the principle of the phase locked loop. Section 2.2 discusses the design of the noise suppression scheme. Section 2.3 shows the mathematical analysis of the noise suppression scheme in the time and frequency domain, which demonstrates the theoretical validation of the system. The experimental results are evaluated in Section 2.4, and the detection performance of the noise suppression scheme is given. Section 2.5 concludes the chapter.

2.1 Radar Detection of Vital Signs and the Phase Locked Loop

2.1.1 Microwave Radar Detection of Vital Signs

A basic microwave Doppler radar system consists of a microwave signal generator, a transmitter antenna, a receiver antenna, and a demodulator, as shown in Fig. 2.1. The microwave

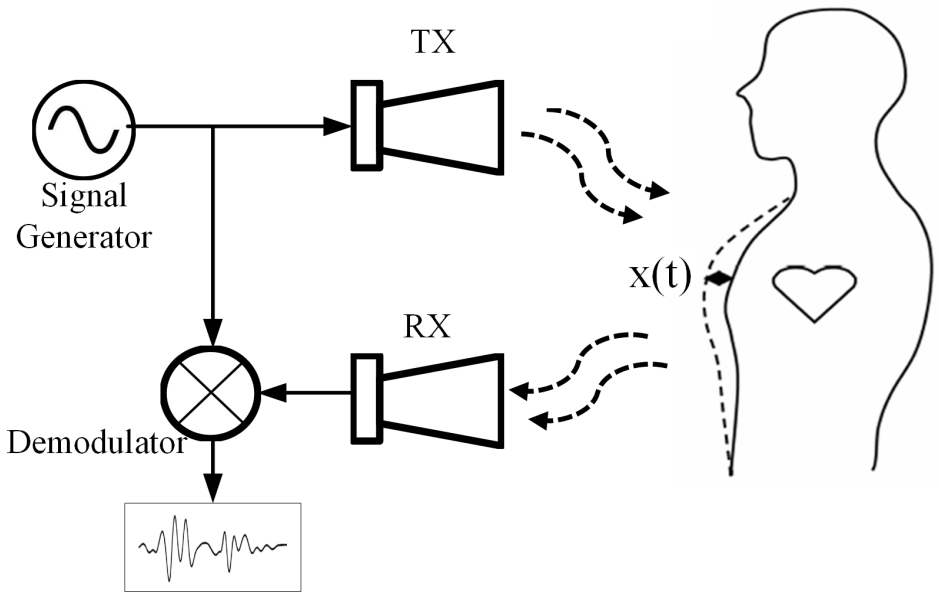

Figure 2.1: Basic structure of microwave Doppler radar system. TX, transmitter antenna; RX, receiver antenna; x(t), chest wall displacement.

signal generator can generate a microwave signal,

$$v_{TX}(t) = sin[\omega_c t + \phi(t)] \tag{2.1}$$

where, ω_c and ϕ represent the angular frequency and phase of the microwave signal, respectively.

This microwave carrier signal is transmitted to the human subject, and gets reflected on the chest wall surface. The reflected microwave signal is received by the receiver antenna. There is a time delay between the received and transmitted microwave signals, which is introduced by the transmission path. Assuming the average distance between the radar antenna and the human subject is d_0, and the time-varying chest wall displacement is $x(t)$, the time delay should be

$$\tau = \frac{2[d_0 + x(t)]}{c} \tag{2.2}$$

where, c is the light speed in the vacuum. The distance is doubled due to the back and forth transmission of the microwave signals. With equations 2.1 and 2.2, the received microwave

signal can be obtained and expressed as

$$v_{RX}(t) = A_{RX} cos[\omega_c(t-\tau) + \phi(t-\tau)] \tag{2.3}$$

where, A_{RX} and $\phi(t-\tau)$ are the amplitude and the phase of the received microwave signals, respectively.

Then the received microwave signals $v_{RX}(t)$ are mixed with the local signal $v_{TX}(t)$ in the demodulator, and the beat signals are generated.

$$\begin{aligned} v_B(t) = & A_{RX}\{sin[2\omega_c t - \omega_c\tau + \phi(t) + \phi(t-\tau)] \\ & + sin[\omega_c\tau + \phi(t) - \phi(t-\tau)]\} \end{aligned} \tag{2.4}$$

The first term represents the high frequency components at the mixer output, which should be filtered out to get the baseband signal. A low pass filter is applied to remove the first term in equation 2.4, and let the low frequency baseband term pass through. Thus, the baseband radar signal can be written as

$$\begin{aligned} v'_B(t) &= A_{RX} sin[\omega_c\tau + \phi(t) - \phi(t-\tau)] \\ &= A_{RX} sin\{2\pi f_c \frac{2[d_0 + x(t)]}{c} + \phi(t) - \phi(t-\tau)\} \\ &= A_{RX} sin\{\frac{4\pi[d_0 + x(t)]}{\lambda_c} + \phi(t) - \phi(t-\tau)\} \end{aligned} \tag{2.5}$$

where, f_c and λ_c are the frequency and wavelength of the microwave signal, respectively.

The phase of $v'_B(t)$ represents the chest wall vibration signal or the vital sign signal, and the phase demodulation of the baseband radar signal can generate the vital signs including the cardiac signals.

$$\begin{aligned} \phi_v(t) &= \frac{4\pi x(t)}{\lambda_c} + \frac{4\pi d_0}{\lambda_c} \\ &= \phi_x(t) + \phi_{d0} \end{aligned} \tag{2.6}$$

where, $\phi_{d0} = 4\pi d_0/\lambda_c$ is the phase introduced by the average distance between the antenna and the chest wall surface. The phase term $\phi_x(t) = 4\pi x(t)/\lambda_c$ exhibits the displacement signal on the chest wall surface, which can represent the vital signs of the human subjects.

The above analysis has demonstrated that the microwave Doppler can achieve the remote sensing of the vital signs through the microwave Doppler effect on the human subject. Thus, the chest wall vibrations caused by the respiration and the cardiac activities are acquired from the phase the microwave signals. Therefore, the microwave Doppler radar system can provide an effective detection of the cardiac signals without any contact to the human subject.

2.1.2 The Phase Locked Loop

The above analysis reveals that the vital signs exist in the phase of the microwave signals, thus the noises that affect the signal quality are the phase noises. To reduce the noise influence, phase locked loop (PLL) should be an effective approach.

A PLL is a negative feedback circuit that synchronizes the output signal with a reference [37]. The fundamental structure of a PLL includes a phase frequency detector (PFD), a loop filter (LPF) and a voltage controlled oscillator (VCO), as shown in Fig. 2.2. The phases of the reference and feedback signals are compared, and the PFD produces an error voltage signal $v_e(t)$ which is proportional to the phase difference. The LPF filters out the high frequency components and noises in $v_e(t)$, and output a control voltage $v_c(t)$, which drives the VCO and thus controls the VCO phase to be equal to that of the reference signal. The adjustment of the VCO phase continues until the phase difference between the VCO and reference signal is a constant, at which time the PLL is locked. In the lock state of PLL, the phase and the frequency of the VCO output track those of the reference, but phase lock does not mean zero phase error.

The synchronous process of the PLL in Fig. 2.2 is mathematically analyzed. The

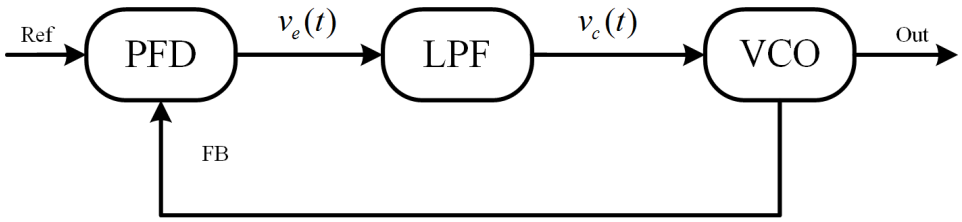

Figure 2.2: Basic structure of phase locked loop. Ref, reference signal; PFD, phase frequency divider; LPF, loop filter; VCO, voltage controlled oscillator; FB, feedback signal.

reference and VCO output signals can be expressed as

$$v_{ref}(t) = v_r sin(\omega_r t + \phi_r) \tag{2.7}$$

$$v_{out}(t) = v_o cos(\omega_o t + \phi_o) \tag{2.8}$$

where, v_r and v_o are the amplitudes, ω_r and ω_o exhibit the angular frequencies, and ϕ_r and ϕ_o represent the phases. Here, the VCO output is directly fed back to the PFD without adding a frequency divider, the feedback signal is the same as the VCO output. The phase of the feedback signal is then compared with that of the reference, and the PFD produces an error signal proportional to their phase difference. Generally, an analog PFD works as a multiplier, thus the error signal can be represented as

$$\begin{aligned} v_e(t) = K_d\{&sin[\omega_r + \omega_o)t + (\phi_r + \phi_o)] \\ &+ sin[(\omega_r - \omega_o)t + (\phi_r - \phi_o)]\} \end{aligned} \tag{2.9}$$

where, K_d is the gain of the PFD and it is an important factor that affects the loop gain. The voltage error signal includes a high frequency component and a low frequency term. The phase difference exists in the low frequency term, thus the low frequency term is desired.

To remove the high frequency component in equation 2.9, the voltage error signal is filtered by the LPF, and a control voltage for the VCO is obtained,

$$v_c(t) = K_d\{sin[\omega_r - \omega_o)t + (\phi_r - \phi_o)]\} \tag{2.10}$$

The control voltage $v_c(t)$ is somewhat proportional to the phase difference when the frequency difference is small. If $\omega_r < \omega_o$, it controls the VCO to gradually decrease its frequency and vice versa. The frequency adjustment may take several periods, which stands for the lock time. After completing the locking process, the VCO output signal has the same frequency as the reference.

$$v_{out}(t) = v_o cos(\omega_r t + \phi'_o) \tag{2.11}$$

where, ϕ'_o is the phase of VCO output after the locking process. By combining 2.10 and 2.11, the control voltage $v_c(t)$ becomes a constant voltage, and it can be expressed as

$$v_{cr}(t) = K_d[sin(\phi_r - \phi'_o)] \tag{2.12}$$

where, ϕ_r and ϕ'_o are the initial phases of the reference and VCO output signals.

According to the characteristics of VCO, its output angular frequency is a function of control voltage as exhibited in ω_v.

$$\omega_v = \omega_o + K_v v_c(t) \tag{2.13}$$

where, K_v is the VCO sensitivity. A high control voltage contributes to a large frequency adjustment. In the locking process, the output frequency of VCO is adjusted to be equal to ω_r, thus the control voltage $v_{cv} = (\omega_r - \omega_o)/K_v$. It shows the control voltage is determined by the frequency deviation between the VCO and the reference. Also, the control voltage in equation (2.12) represents v_{cr} at frequency ω_r, so $v_{cv} = v_{cr}$.

$$\phi'_o = \phi_r - sin^{-1}(\frac{\omega_r - \omega_o}{K_d K_v}) \tag{2.14}$$

Equation (2.14) contains an arcsine term, which means $\omega_r - \omega_o$ should be less than $K_d K_v$.

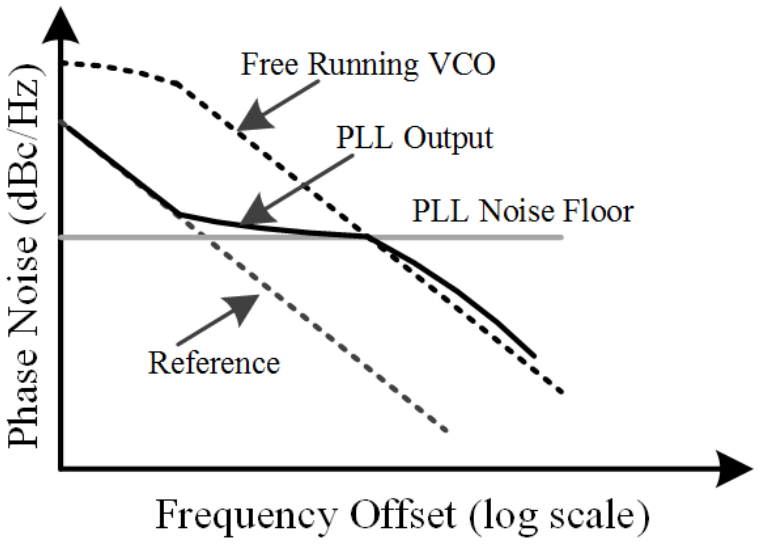

Figure 2.3: Phase noise in the phase locked loop.

When the frequency difference exceeds $K_d K_v$, the loop loses the tracking function, and become unlocked. Thus, $|\omega_r - \omega_o| \leq K_d K_v$ defines the lock-in range of a PLL.

Keep the frequency difference within the lock-in range. When the phase error $\phi_r - \phi'_o$ is quite small, equation (2.12) can be simplified to a linear function through the small angle approximation.

$$v_{cr} = K_d(\phi_r - \phi'_o) \tag{2.15}$$

This is the linear model of PFD, and the phase error totally determines the control voltage, thus the frequency and phase of VCO. Once locked, phase error is a fixed value. If the reference signal has a very high phase stability, the VCO can be stabilized at the same level.

In the frequency domain, phase locked loop is a low pass filter for the reference, but a high pass filter for the VCO. Thus, the VCO output signal has an in-band spectrum similar to the reference and an out-of-band spectrum determined by VCO [38]. As shown in Fig. 2.3, the noise of the PLL output comes from reference, free running VCO and the PLL noise floor, among which the noise floor is determined by the performance of the PFD and the other devices in the loop.

An ideal VCO output or PLL output has a loop bandwidth set at the intersection of the free running VCO and the PLL noise floor, which is shown in Fig. 2.3. At the frequencies lower than this intersection point, the PLL suppresses the free running VCO noise and allows the reference and the PLL noise to pass through, but maintains VCO noise and reduces floor noise outside the loop bandwidth. Generally, the in-band noise level of the VCO output signal is the most important performance of the PLL output. As the reference noise and the PLL floor noise determine the in-band noise level, a good reference and a high-quality PFD should be selected for the design.

2.2 Design of Noise Suppression Scheme

The vital sign detection using continuous wave (CW) Doppler radar involves transmitting a microwave signal which is phase modulated by the chest surface displacement, and then receiving and demodulating the reflected wave to obtain the vital sign information. In the detection process, residual phase noise and path noise contaminate the received wave, reducing the quality of the phase information. Here the residual phase noise which is due to the deterioration of phase coherence between the received and local waves, affects the beat signal, so we consider it as the phase noise of the received wave for the convenience of analysis. As the vital sign information is contained in the phase of the reflected wave, phase noise should be suppressed to extract a low-noise vital sign signal. Considering the received wave as a free running VCO which has a high phase noise level, we can phase lock it to a low noise highly stable reference. Noise within the loop bandwidth can be suppressed, as the PLL is a high pass filter to the free running VCO. But since the vital sign signal is also within the loop bandwidth, the PLL suppresses the desired signal as well as the noise if a single carrier is used. To achieve the goal of extracting the vital sign signal and reducing the noise at the same time, we introduce a dual-carrier scheme. The concept is to some extent similar to the idea in phase stabilized radio over fiber (RoF) [39, 40], in which one carrier is for the stabilization of the transmission path, while the other one

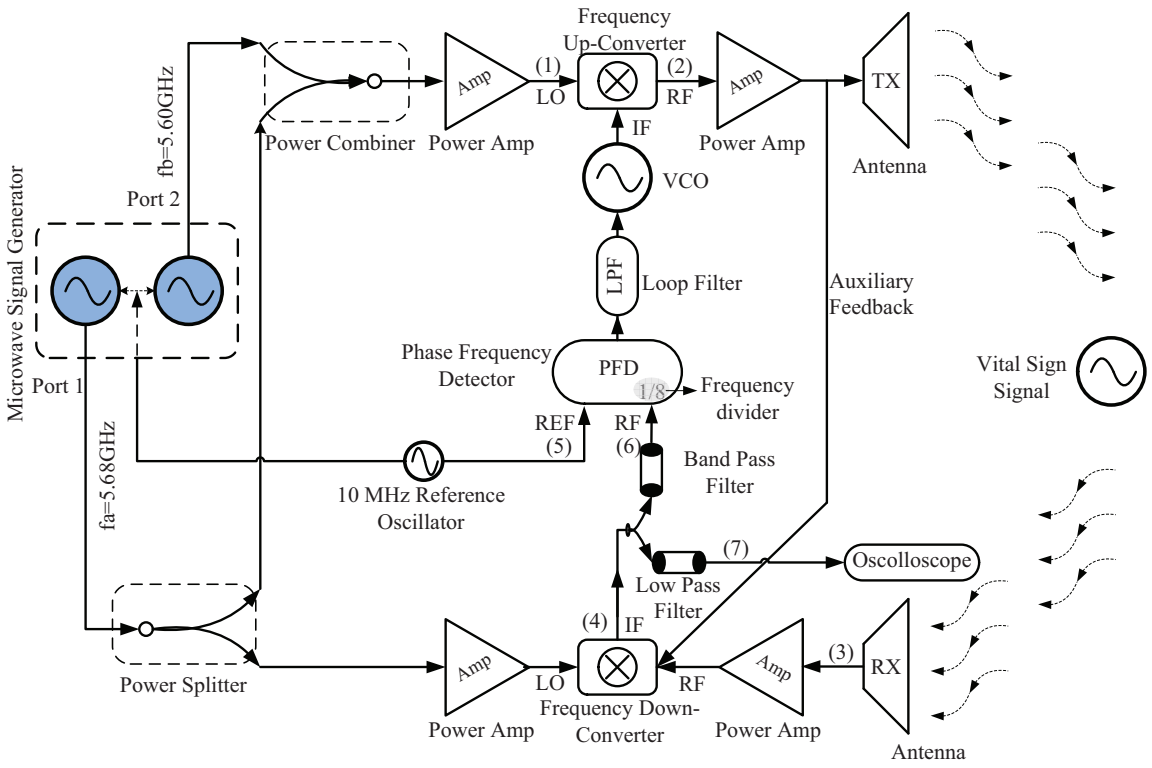

Figure 2.4: Experimental setup for noise suppression in vital sign detection. PFD, phase frequency detector; LPF, loop filter; VCO, voltage controlled oscillator; Amp, power amplifier; TX, transmitter; RX, receiver.

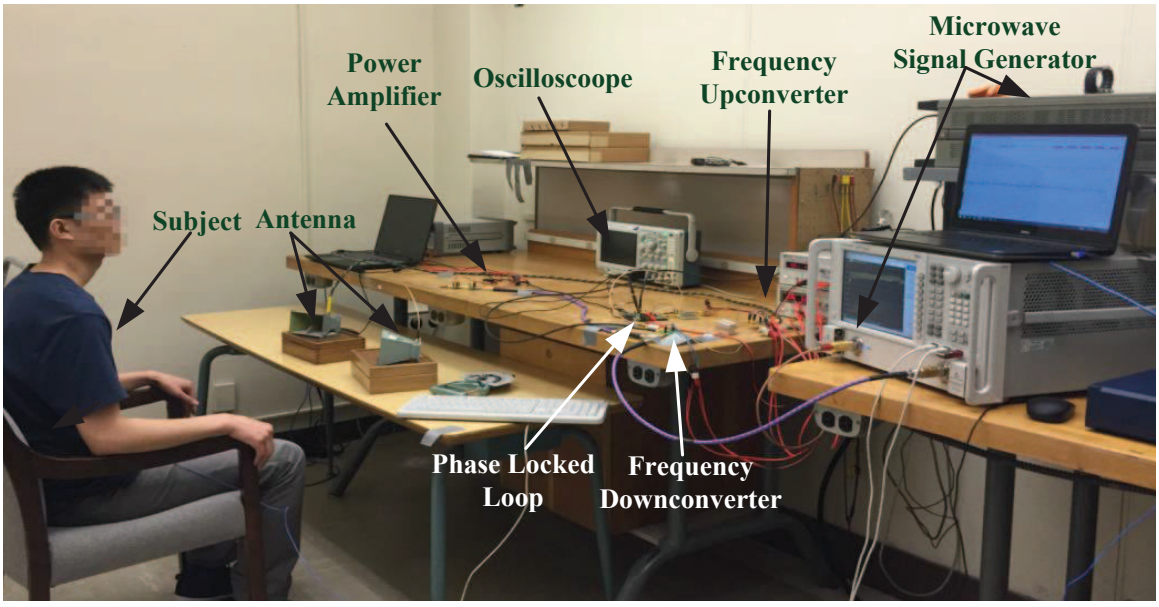

Figure 2.5: Experimental setup for the vita sign detection.

transmits the signals.

Based on the RoF and PLL theory [39, 40, 37, 38], a dual-carrier noise suppression scheme is designed to reduce the phase noise, as shown in Fig. 2.4, and the experimental measurement is shown in Fig. 2.5. It consists of microwave signal sources, power amplifiers, frequency converters, antennas, a phase frequency discriminator, a loop filter, and a VCO. The microwave signal generator (HP 83622B) and PNA network analyzer (Agilent N5222A) are phase locked to a 10-MHz reference signal and generate 5.60 and 5.68-GHz microwave signals, respectively. These two signals are then power combined and directed to the local signal (LO) port (point 1) of an I/Q frequency up-converter (Hittite HMC925LC5), whose intermediate frequency (IF) signal is provided by an 80-MHz VCO. After frequency up-converted by 80 MHz, they are amplified and split to two branches. One branch is transmitted by the TX antenna, modulated by the vital sign signal, and then received by RX antenna (point 3). The other one is directed to the auxiliary feedback path, which is introduced for auxiliary phase lock to ensure the stability of vital sign detection. It provides a power level around -18 dBm, which is the minimum power required to lock the loop when there is no RX received signal. The effect of the auxiliary is discussed in Appendix A.1. Microwave signals of two branches are combined and mixed with the local 5.68-GHz microwave signal, and down-converted to 80 MHz and low frequency signals (point 4), as well as their phase noise including residual phase noise and path noise. The PLL locks the 80-MHz beat signal to the same reference signal (point 5) as PNA network analyzer and microwave signal generator, during which process the PLL controls the V-CO's phase to make the 80-MHz beat signal having a stable phase. It means the VCO pre-cancels the residual phase noise and path noise in the transmitted carriers, so the 80-MHz beat signal and its corresponding received 5.76-GHz carrier have a low phase noise but contain no vital sign information for it's considered as path noise. This process provides a clean transmission path for the 5.68-GHz carrier, and its demodulation with the 5.68-GHz local signal provides a low-noise vital sign signal (point 7). Here, all the devices are discrete components and the parameter values can be adjusted according to the characteristics

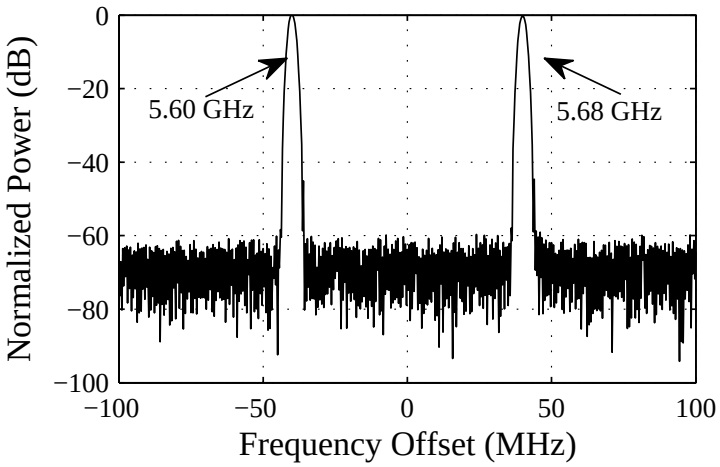

Figure 2.6: Measured phase locked microwave signals.

of the devices. The detailed analysis of our design is presented in section 2.3.

2.3 Mathematical Analysis of the Noise Suppression Scheme

2.3.1 Time Domain Analysis

The microwave signals from signal generator and network analyzer can be expressed as

$$v_1(t) = sin(2\pi f_a t + \phi_a) + sin(2\pi f_b t + \phi_b) \tag{2.16}$$

where f_a and f_b are 5.68 and 5.60 GHz, respectively, while ϕ_a and ϕ_b are their corresponding phases. The two signals are amplified and adjusted to have the same power at the LO port (point 1) of frequency up-converter, as shown in Fig. 2.6.

Then the microwave signals are mixed with the 80-MHz VCO signal to get the frequency up-converted signals at the RF port (point 2),

$$\begin{aligned} v_2(t) = & \, sin[2\pi(f_a + f_v)t + (\phi_a + \phi_v)] \\ & + sin[2\pi(f_b + f_v)t + (\phi_b + \phi_v)] \end{aligned} \tag{2.17}$$

where f_v is 80 MHz and ϕ_v represents the phase of VCO. After being amplified, they are

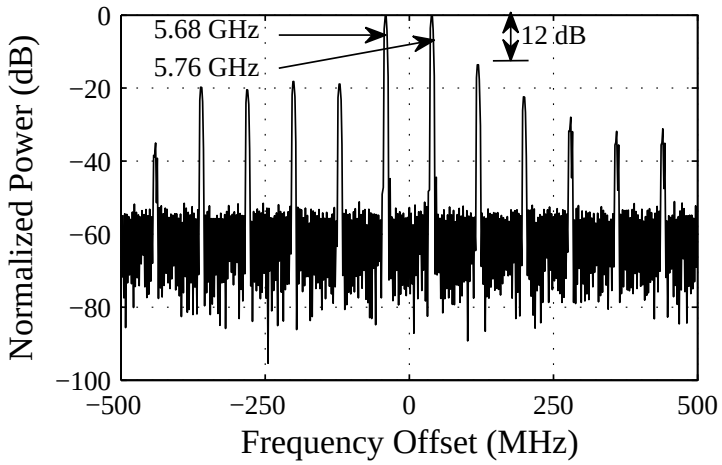

Figure 2.7: Measured frequency up-converted microwave signals.

transmitted through the TX antenna, and the spectrum is shown in Fig. 2.7. Due to the properties of VCO and the frequency up-converter, there are many unwanted sidebands around the desired 5.76 and 5.68 GHz. They are spreading in the span of about 2.5 GHz, with space of 80 MHz. Through adjusting the power level and delay/phase at LO (point 1) and IF ports of frequency up-converter, the ratio between carrier and unwanted sidebands can reach 12 dB. When mixed with 5.68-GHz local signal in the frequency down-converter (Hittite HMC951LP4E), both 5.76 and 5.60-GHz signals can produce the 80-MHz beat signal which is fed back to lock the loop (point 6). Thus the 5.60-GHz sideband component has influence on the system performance, but the -20 dB ratio to 5.76-GHz signal significantly reduces such an effect. The higher order sidebands have no influence on the performance of our system, as the band pass filter will filter out their corresponding beat signals. Thus, we will focus on the 5.68 and 5.76-GHz signals and neglect the sidebands in the following analysis.

After being transmitted through a horn antenna, the microwave signals are phase modulated by the vital sign signal, including the heartbeat and respiration. Assuming the displacement of human chest is $x(t)$, it will contribute to a delay of $\tau_x = 2x(t)/c$ or a phase of $\varphi = 2\pi f \tau_x = 4\pi x(t)/\lambda$, where c is the speed of electromagnetic wave and λ is the wavelength. Thus, we can detect the vital sign signal through analyzing the phase of received

microwave signals.

The microwave signals received by the RX antenna (point 3) contain vital sign signal as well as noise,

$$\begin{aligned} v_3(t) = & \, cos[2\pi(f_a + f_v)(t+\tau) + (\phi_a + \phi_v + \varphi_n)] \\ & + cos[2\pi(f_b + f_v)(t+\tau) + (\phi_b + \phi_v + \varphi_n)] \end{aligned} \tag{2.18}$$

where $\varphi_n = \varphi_{pa} + \varphi_{rd}$, φ_{pa} and φ_{rd} represent the path noise and residual phase noise respectively, $\tau = \tau_x + \tau_0$ and $\tau_0 = 2d_0/c$ is ascribed to the average distance d_0 between the chest and the antenna. The received signals have a low power level, so a low noise power amplifier (LNA, Hittite HMC902LP3) is required here. After amplification, they are combined with the auxiliary path signals. The auxiliary path signals help to improve the locking performance of the system, especially when the amplified received signals are a little lower than -18 dBm, which is required to produce a -10 dBm minimum feedback signal (point 6) for the PFD. The effect of the auxiliary path on the extraction of vital sign signals is analyzed in Appendix A. If the amplified received signal is over -18 dBm, the auxiliary path is generally not necessary. Then the combined microwave signals are mixed with a 5.68-GHz local signal split from the PNA network analyzer, producing beat signals at the frequency down-converter IF port (point 4).

$$\begin{aligned} v_4(t) = & \, sin[2\pi f_v t + 2\pi(f_a + f_v)\tau + \phi_v + \varphi_n] \\ & + sin[2\pi(f_b - f_a + f_v)t + 2\pi(f_b + f_v)\tau \\ & + (\phi_b - \phi_a + \phi_v + \varphi_n)] \end{aligned} \tag{2.19}$$

where $f_b - f_a + f_v$ equals to 0. The beat signals are split to two branches, one of which is directed to a low pass filter with a cut-off frequency of 20 kHz to extract the vital sign signal (point 7). The other branch passes through a 58-82 MHz band pass filter and all

the harmonics of 80 MHz are filtered out. Only the 80-MHz beat signal corresponding to the first term of $v_4(t)$ is fed back to the PFD (point 6), where it is divided to 10 MHz and discriminated with the 10-MHz reference (point 5).

$$v_5(t) = sin(2\pi f_{ref} t + \phi_{ref}) \tag{2.20}$$

where f_{ref} and ϕ_{ref} are the frequency and phase of the reference oscillator, respectively. The PFD discriminates their phase difference and outputs an error signal. It is filtered by the loop filter and then drives the VCO to produce an 80-MHz IF signal (point 6), whose phase is pre-adjusted to cancel the noise and achieve a low noise 80-MHz beat signal. When the loop is locked, the phase relationship between $v_5(t)$ and the first term of $v_4(t)$ should be

$$[2\pi(f_a + f_v)\tau + \varphi_n] + \phi_v = 8\phi_{ref} \tag{2.21}$$

With equation (2.21), the beat signal $v_4(t)$ can be rewritten as

$$\begin{aligned} \tilde{v_4}(t) = & \, sin(2\pi f_v t + 8\phi_{ref}) + sin[2\pi(f_b - f_a + f_v)t \\ & + 2\pi(f_b - f_a)\tau + (\phi_b - \phi_a + 8\phi_{ref})] \end{aligned} \tag{2.22}$$

Through phase locking the 80-MHz beat signal (point 6) to the reference signal provided by the low-noise reference oscillator (point 5), the PLL controls the VCO to pre-adjust its phase. Thus the phases of the transmitted carriers are adjusted for canceling the residual phase noise and path noise. As a result, the phase noises of both beat terms shown in $\tilde{v_4}(t)$ are suppressed to the level of the reference.

Passing the beat signals through the low pass filter, we can filter out the 80-MHz beat signal (point 6), and obtain the time domain vital sign signal (point 7) in the oscilloscope. Combined with $f_b - f_a + f_v = 0$ and $\tau = \tau_x + \tau_0$, the second term of $\tilde{v_4}(t)$ represents vital

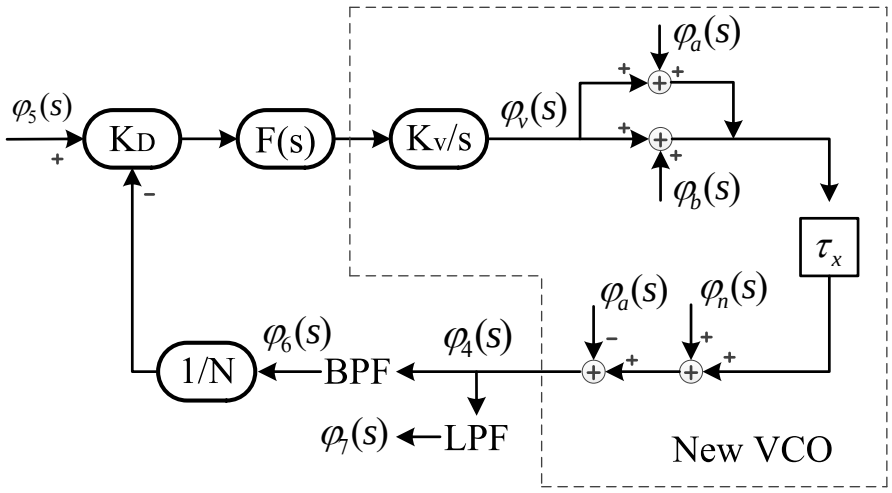

Figure 2.8: Linear frequency domain model. K_D, gain of PFD; F(s), transfer function of LPF; K_v, gain of VCO; $\varphi_a(s)$, phase of carrier a; $\varphi_b(s)$, phase of carrier b; $\varphi_6(s)$, feedback signal.

sign signal,

$$v_7(t) = sin\{[2\pi(f_b - f_a)[\frac{2d_0}{c} + \frac{2x(t)}{c}] + (\phi_b - \phi_a + 8\phi_{ref})]\} \quad (2.23)$$

Here, d_0 is constant and ϕ_{ref} is low-noise in the system. As both 5.60 and 5.68-GHz signals are phase locked to the 10-MHz reference, $\phi_b - \phi_a$ has a noise level similar to that of $8\phi_{ref}$. Therefore the noise in $v_7(t)$ is suppressed when the loop is locked, resulting in low noise in the vital sign signal.

2.3.2 Frequency Domain Analysis

For better understanding of the noise suppression mechanism, Fig. 2.4 is simplified to a linear frequency domain model, as shown in Fig. 2.8. The noise and vital sign signals are contained in the frequency down-converted signals $\varphi_4(s)$. After the band and low-pass filtering, the feedback signal (noise information) $\varphi_6(s)$ and vital sign signal $\varphi_7(s)$ are

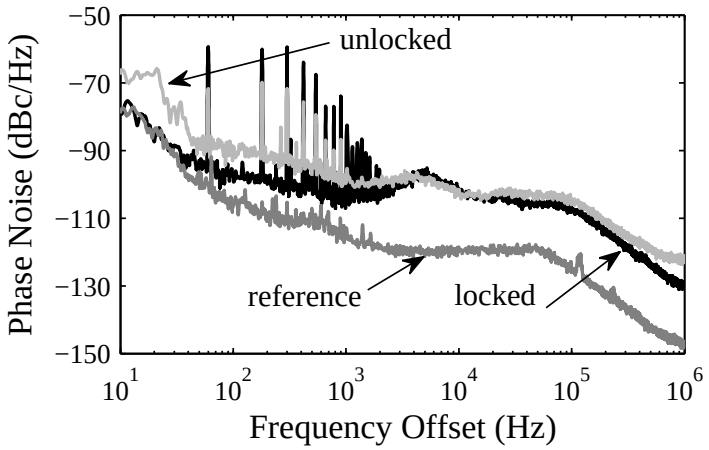

Figure 2.9: Measured phase noise spectrum of the beat signal and reference.

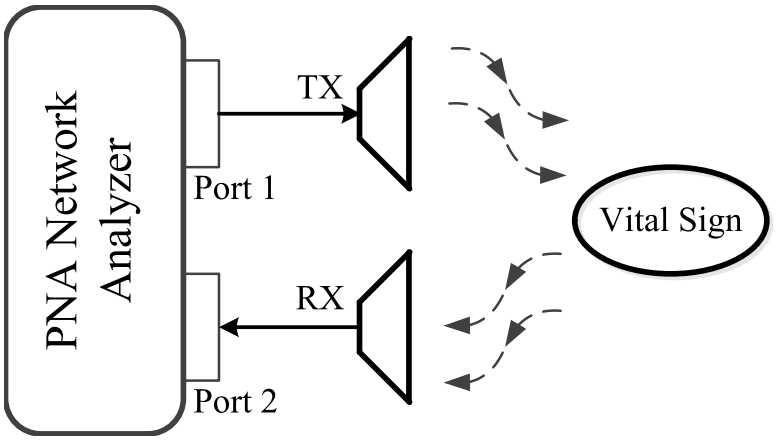

Figure 2.10: Scheme of direct vital sign detection. TX, transmitter antenna; RX, receiver antenna.

obtained, where $\varphi_6(s)$ and $\varphi_7(s)$ correspond to carrier a and b respectively.

$$\varphi_6(s) = [\varphi_v(s) + \varphi_a(s)]e^{-s\tau_x} - \varphi_a(s) + \varphi_n(s) \tag{2.24}$$

$$\varphi_7(s) = \varphi_6(s) + [\varphi_b(s) - \varphi_a(s)]e^{-s\tau_x} \tag{2.25}$$

where, $\varphi_a(s) = A\varphi_5(s)$, $\varphi_b(s) = B\varphi_5(s)$, A and B are the frequency ratio between their carriers and reference respectively, for carrier a and b are locked to the reference signal $\varphi_5(s)$. In Fig. 2.8, the feedback signal is also locked to $\varphi_5(s)$, and $\varphi_6(s) = N\varphi_5(s)$. Thus

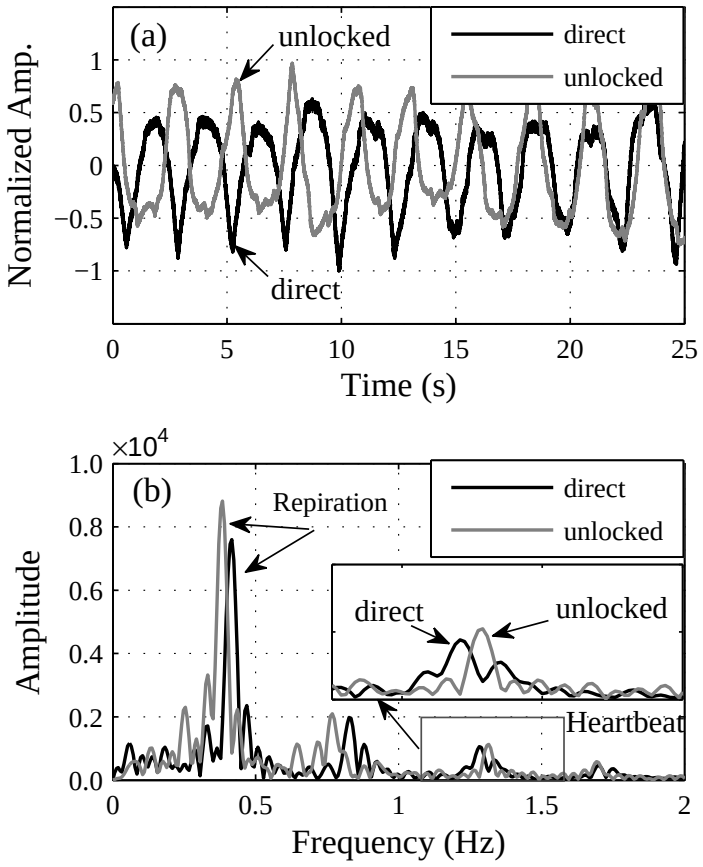

Figure 2.11: Vital sign signals with direct (black line) and unlocked system (gray line).

the transfer function between the vital sign signal and reference, $H(s) = \varphi_7(s)/\varphi_5(s)$, can be written as

$$H(s) = N + (B - A)e^{-s\tau_x} \tag{2.26}$$

Therefore, the noise performance of vital sign signal is determined by that of the reference signal, and the path and residual phase noise are suppressed. Besides, the vital sign is extracted as shown in (2.26). The transfer function of the noise is very complex, but it can be seen in Fig. 2.8, $\varphi_n(s)$ is the noise of new VCO (NVCO). In the PLL, it is high frequency passed and get suppressed in the low-frequency vital sign signal. Thus the noise and vital sign signal are suppressed and extracted through carrier *a* and *b*, respectively.

Due to the very low frequency of vital sign signal, it is hard to exhibit the perfor-

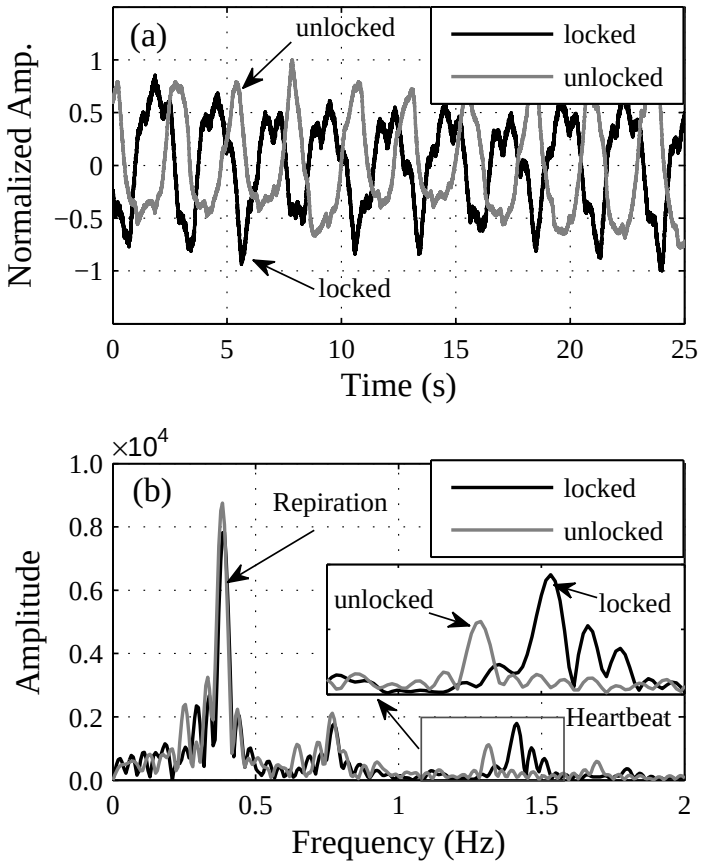

Figure 2.12: Vital sign signals with locked (black line) and unlocked system (gray line).

mance of phase noise suppression through the spectrum of (2.23). The 80-MHz feedback beat signal, which is the first term of (2.22), is used to demonstrate the noise suppression performance as it has the same suppression ratio as the vital sign signal. Its phase noise spectrum measured with a spectrum analyzer (Agilent E4440A) is shown in Fig. 2.9. As a comparison, the phase noise spectra of the reference and the beat signal of an unlocked system are also given. The unlocked system is a modified system in Fig. 2.4 by connecting the RF port of PFD to VCO output instead of the down-converted signal and disconnecting the auxiliary feedback.

Fig. 2.9 shows that the 80-MHz beat signal of the locked system, which is a new VCO to the loop, has a suppressed phase noise within the 10-kHz loop bandwidth and exhibits a

noise level that is about 12-dB lower than the unlocked case at 10-Hz frequency offset. Up to 50-Hz frequency offset, it is stabilized to the reference signal and has almost the same noise level. At a frequency offset of more than 10 kHz, which is the loop bandwidth determined through the method in [41], the noises are not suppressed due to PLL's high-pass characteristics for the NVCO signal. It demonstrates that the PLL successfully suppresses residual phase noise and path noise, which facilitates detection of a clean vital sign signal.

2.4 Experimental Evaluation

2.4.1 Noise Performance of the System Devices

To verify that our system devices introduce no extra noise, the measurement result of the unlocked system, which is a modified design in Fig. 2.4 as mentioned before, is compared with that collected by a direct vital sign detection system shown in Fig. 2.10. In the direct measurement scheme, the PNA network analyzer transmits a microwave signal, receives and demodulates the reflected signal, and then displays a time domain vital sign signal. Transmitting power in port 1 of the network analyzer is approximately 6 dBm, and the antenna is about 50 cm away from the human subject. A time domain signal of 25 seconds is recorded and analyzed in the frequency domain, represented by black lines in Fig. 2.11. With the same transmit power and detection distance, the vital sign detected with the unlocked system is exhibited by gray lines in Fig. 2.11.

In the time domain, respiration is obvious, but the heartbeat which is superimposed on the respiration signal, is hard to recognize. Using the Fast Fourier Transform, we can represent the vital sign signal in frequency domain as shown in Fig. 2.11(b). The respiration frequency through direct measurement scheme is 0.41 Hz, and the unlocked case has a respiration frequency of 0.38 Hz. The frequency difference is due to the status of the subject, as the experiments are not conducted at the same time. The heartbeat, not as obvious and strong as the respiration signal, has a frequency around 1.3 Hz. As shown in the inset of Fig. 2.11(b), amplitude and frequency of heartbeat in two schemes are

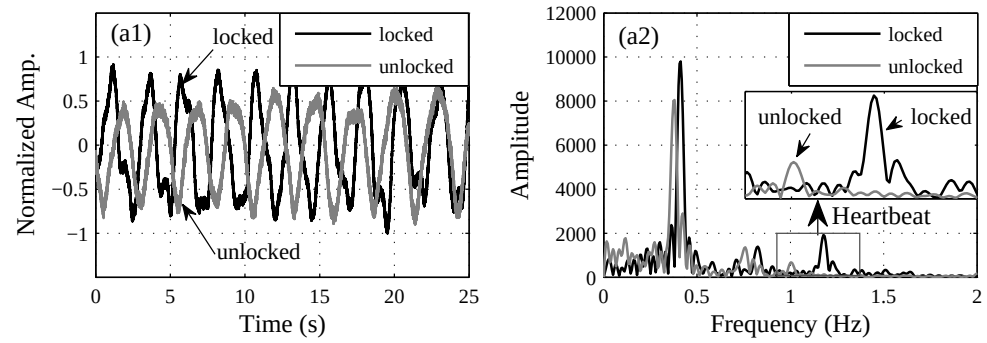

(a) 100 cm

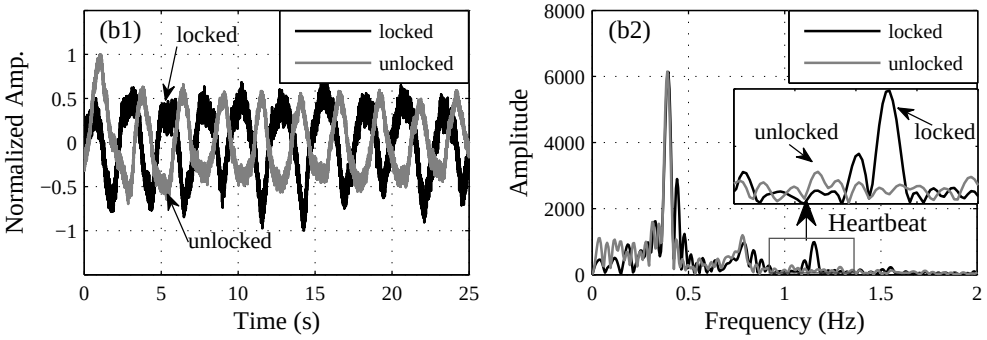

(b) 150 cm

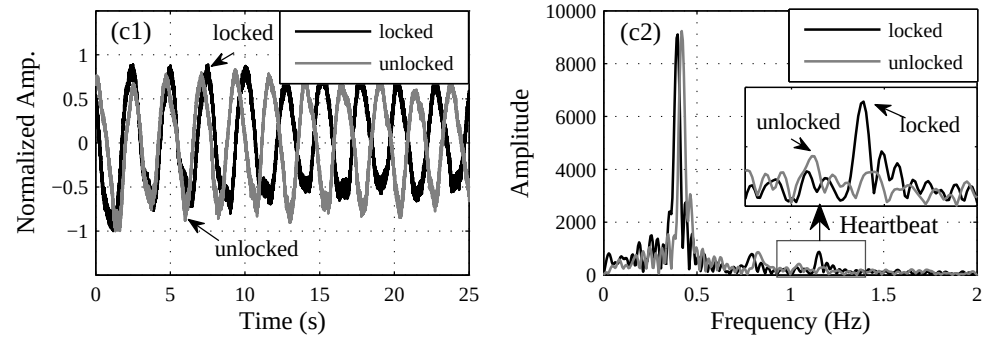

(c) 200 cm

Figure 2.13: Vital sign signals in time and frequency domain at 100 cm, 150 cm and 200 cm, with locked system in black lines and unlocked system in gray lines.

almost the same. Given the results of vital sign measurements from the unlocked system and the direct detection are similar, the additional system components in our design do not introduce obvious extra noise.

Then we compare the unlocked system with our loop-locked design shown in Fig. 2.4. With the same transmit power and detection distance of Fig. 2.11, the vital sign measure-

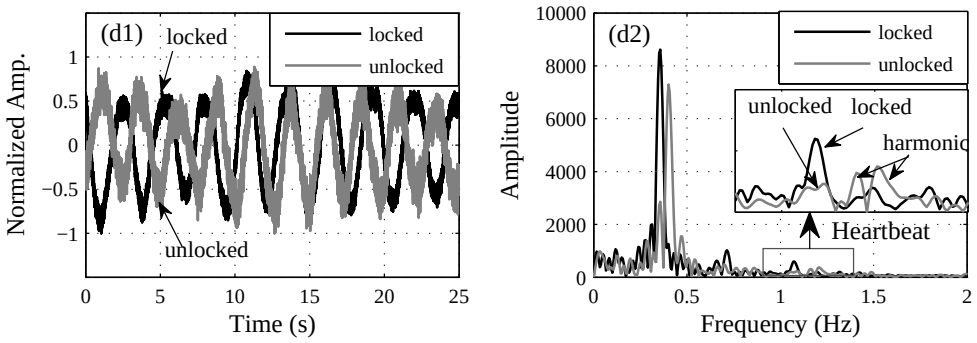

(a) 250 cm

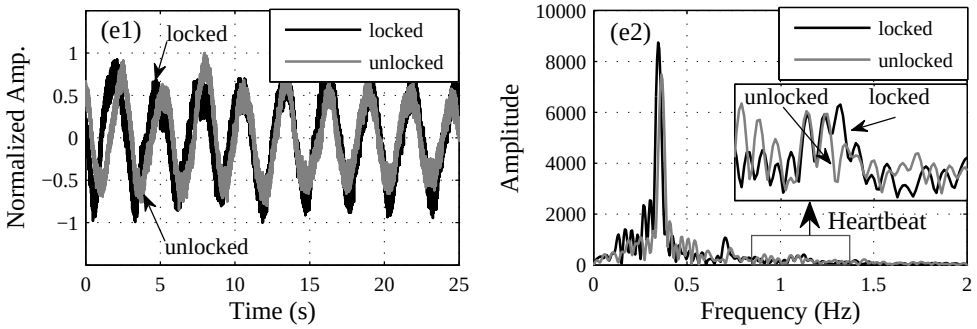

(b) 300 cm

Figure 2.14: Vital sign signals in time and frequency domain at 250 cm and 300 cm, with locked system in black lines and unlocked system in gray lines.

ment results from both systems are represented in Fig. 2.12. Except the vital sign signals have slightly different frequencies, the respiration rate from the locked system is quite similar to that of the unlocked case and their amplitudes are similar which might be due to the condition of the subject. When the loop is locked, uncorrelated phase noise is suppressed. Thus, a clearer heartbeat is obtained, meaning there is less possibility of inaccuracy in detection.

2.4.2 Detection Performance of the System

In order to further explore the detection performance of the locked system, we extend the measurement distance to 100 cm, 150 cm, 200 cm, 250 cm and 300 cm without changing the transmit power. As shown in Figs. 2.13 and 2.14, the results of locked system are represented in black lines while those of unlocked system in gray lines. The time domain signal

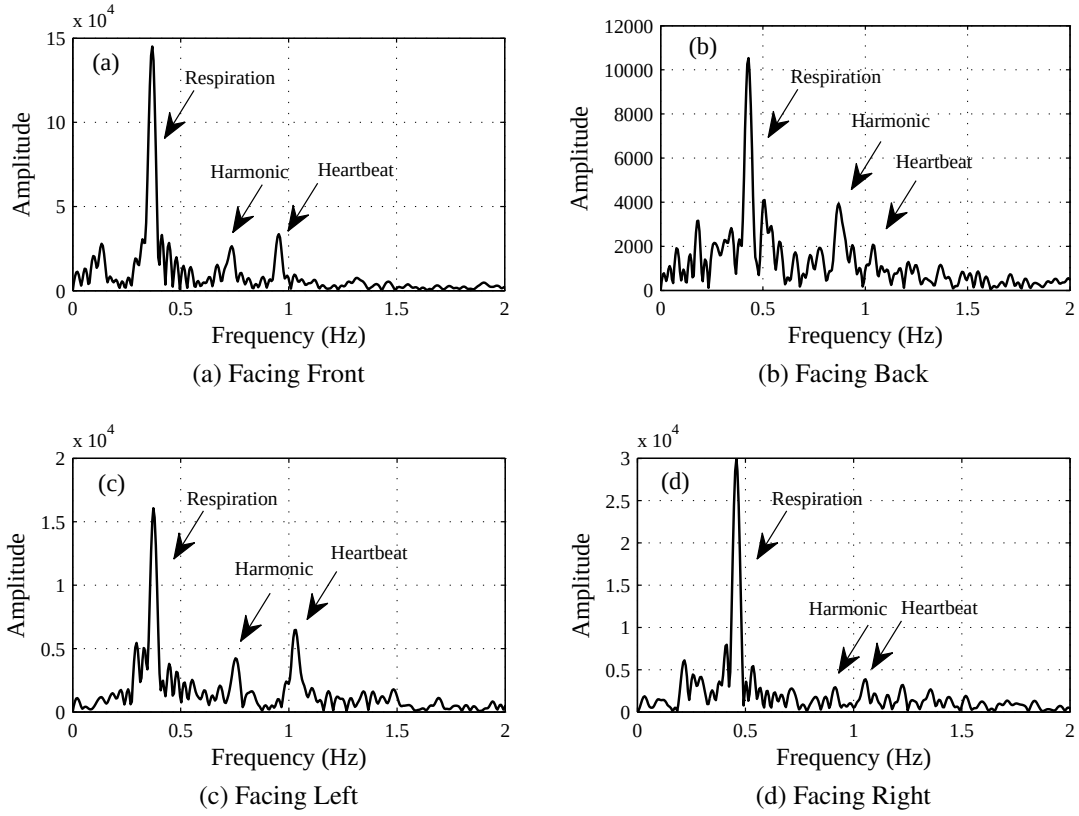

Figure 2.15: Vital sign detection at four orientations.

exhibits the periodical fluctuation, which is the respiration with heartbeat superimposed on it. The respirations of both locked and unlocked systems are around 0.4 Hz and even overlapping in Fig. 2.13 (b2). For the heartbeat, the locked system has a clear frequency component at about 1.2 Hz, which slightly changes at different detecting distances. As the measurement of unlocked system is conducted at a different time, the heartbeat frequency detected is around 1.0 Hz.

Figs. 2.13 and 2.14 show that the heartbeat can be detected by the unlocked system at a distance of 100 cm, but it is hard to recognize when the distance exceeds 150 cm. However, the locked system can still detect the heartbeat at 250 cm. At 300 cm, a quite rare wave is reflected back to the loop, therefore heartbeat is severely noise-influenced and hard to detect. As respiration has a much larger displacement than heartbeat, both systems can still detect it at 300 cm.

Vital sign detection in four physical orientations is also conducted with the same experimental setup as that for Fig. 2.12. During the detection, the subject changes the orientation to let the antenna face the front, back, left and right side of the subject. Measurement results for the four orientations are shown in Fig. 2.15. Respiration can be easily detected in all four orientations. For heartbeat signal, it can be detected obviously when facing front and left (Fig. 2.15 (a) and (c)). When the antenna faces the back and right side of the subject, the heartbeat signal is very weak (Fig. 2.15 (b) and (d)) due to the less effective reflective area. The back side signal as shown in Fig. 2.15 (b) has the worst noise level.

2.5 Conclusion

In this chapter, a dual-carrier vital sign detection system with a noise suppression scheme based on PLL is designed to automatically reduce the residual phase noise and path noise. Through the phase discrimination between one carrier's beat signal and the low-noise reference signal in the PFD, the noises are extracted and then suppressed in the PLL, providing a clean transmission path for the other carrier. Therefore, the vital sign signal contained in the phase of the second carrier can be obtained with low noise.

Experiments with locked and unlocked system have been carried out to compare the noise and detection performance. The results show that our system can effectively suppress the residual phase noise and path noise, improving the SNR by about 12 dB at 10-Hz frequency offset, and significantly increase the detection distance of the weak heartbeat signal. The successfully demonstrated detection distance for heartbeat is at least 250 cm, more than double the distance of the unlocked system. In addition, experiments are conducted to demonstrate effective measurements of vital sign in four physical orientations.

CHAPTER 3
INVESTIGATION OF SEISMOCARDIOGRAM SIGNAL FROM RADAR SIGNAL

In the previous chapter, a dual-carrier vital sign detection system with a noise suppression scheme based on PLL is designed to automatically reduce the noise influence in the microwave Doppler radar system. After suppressing the noise and obtaining a high quality signal, an investigation is conducted to explore what type of cardiac signal can be captured by the radar system. The theoretical analysis of the radar detection principle shows that the radar system acquires the vibration activity of the chest wall, which indicates a similarity to the SCG signal that records precordial vibrations and reflects the heart contraction and blood ejection behavior of human subjects. Thus, an exploration of the similarity between the radar signal and the SCG signal is presented in this chapter.

The rest of the chapter is organized as follows. Section 3.1 shows the theoretical analysis of the radar signal and the experimental setup. The experimental results are analyzed in Section 3.2, illustrating the similarity between radar signal and SCG signal. Section 3.3 demonstrates the radar signal could estimate the SCG features with high accuracy, such as the time shift of fiducial points under perturbation. Section 3.4 concludes the chapter.

3.1 Theoretical Analysis and Experimental Setup

3.1.1 Theoretical Analysis of Radar Signal

Microwave Doppler radar system is an effective approach to acquire the vital sign information, such as the rates of respiration and heartbeat [10, 11], from precordial vibrations. Through a quadrature demodulation structure, the baseband I and Q radar displacement

signals are acquired and can be expressed using Taylor expansion.

$$\begin{aligned} B_I(t) = E_0[2\pi f_d t - \frac{1}{3!}(2\pi f_d t)^3 + \cdots]cos\phi \\ + E_0[1 - \frac{1}{2!}(2\pi f_d t)^2 + \cdots]sin\phi \end{aligned} \tag{3.1}$$

$$\begin{aligned} B_Q(t) = -E_0[2\pi f_d t - \frac{1}{3!}(2\pi f_d t)^3 + \cdots]sin\phi \\ + E_0[1 - \frac{1}{2!}(2\pi f_d t)^2 + \cdots]cos\phi \end{aligned} \tag{3.2}$$

where E_0 is the amplitude, f_d is the Doppler frequency shift, and ϕ is a constant phase introduced by reflection and average distance between radar and chest wall surface. Here, $2\pi f_d t$ is the cardiac signal we desire to obtain from radar system, and it can be rewritten as $4\pi[x(t)]/\lambda$, where $x(t)$ represents the displacement of chest wall vibration and λ is the wavelength of microwave signal.

Both I and Q signals contain the harmonics that could introduce further interference to the radar waveforms, change its morphology, and affect the SCG features. In addition to harmonics, signal distortion occurs in the harmonic terms, as the vibration includes activities of heartbeat and respiration.

Since SCG represents the acceleration of chest wall activity, the second derivative of radar baseband signal is extracted to obtain RAW for better comparison with SCG. As shown in Fig. 3.1, after each ECG R peak, RAW has one obvious peak as well as the dorso-ventral SCG (SCG_{DV}), and the peak exhibits a similar change of magnitude as SCG_{DV}, which can be easily seen from the magnitudes of each peak. Compared with ECG, both RAW and SCG_{DV} contain multiple high frequency components within each heartbeat and exhibit a high similarity.

However, the high frequency components of SCG_{DV} and radar have difference in magnitude shown in Fig. 3.1. According to (3.1) and (3.2), the radar system could introduce

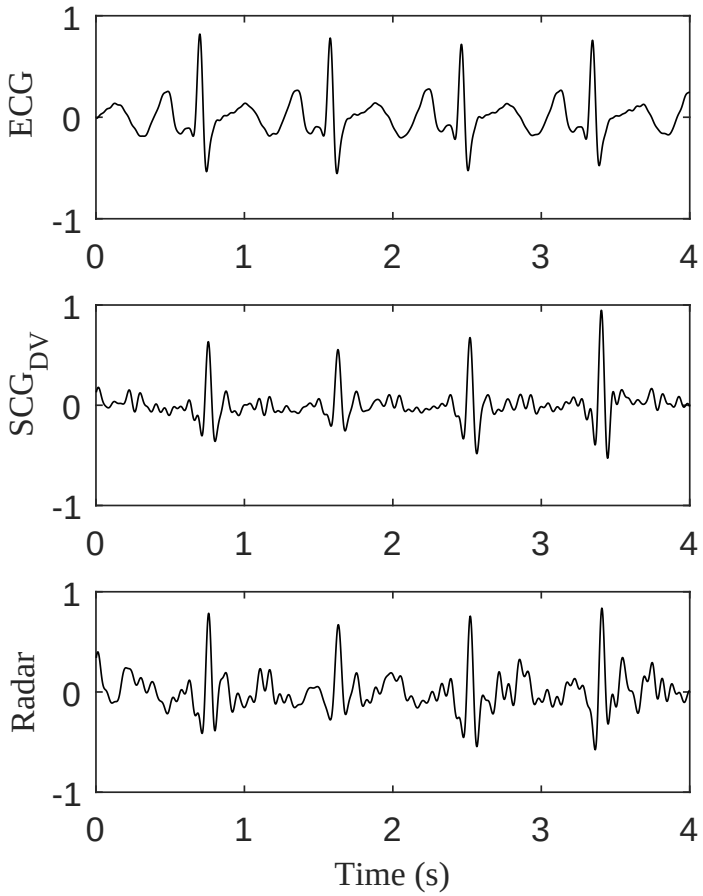

Figure 3.1: Time domain ECG, SCG and RAW signals.

additional harmonics and signal distortion, which can affect the morphology of RAWs. Thus, the RAWs can be influenced by signal harmonics and distortion.

To reduce the effect of interference on RAW, (3.1) and (3.2) are further analyzed. Low order harmonics centered at the lower frequency band have large magnitudes, and high order harmonics located in higher frequency band have pretty small magnitudes. Therefore, the cardiac signals are less affected by interference at a higher frequency band wherein the analysis might provide a better similarity between SCG and RAW.

3.1.2 Experimental Setup

A microwave Doppler radar system is set up to acquire a radar displacement signal, consisting of a microwave signal generator (Agilent N5222A), horn antennas (A-INFO LB-20180-SF), an I/Q frequency downconverter (Hittite HMC951LP4E), and a data acquisition unit (DAQ, Analog Devices AD7770). A 5.8 GHz microwave carrier signal with a power level of 6 dBm is generated and transmitted to human subjects facing the antenna. The transmitting and receiving antennas are positioned at the same level with a 50 centimeter distance, along their respective antenna boresights, from a mid-sternum point of a human subject where the contact SCG sensor is attached. The human subject faces the midpoint of the line segment connecting the antennas with the mid-sternum point located approximately on the perpendicular bisector of the line segment. Due to the beamwidth of the antennas, the microwave reflection occurs on the entire upper chest wall surface, and the precordial vibrations on the surface are introduced to the phase of microwave carrier signals. The I/Q frequency downconverter transfers the chest vibrations contained in the microwave carrier signal to baseband quadrature radar displacement signals that are sampled by the data acquisition unit at a rate of 1000 samples/second.

The contact sensor system consists of a high-resolution accelerometer (356A32, PCB Piezotronics, Depew, NY, USA) for 3-axis SCG and a BN-RSPEC for electrocardiogram (ECG). The accelerometer was placed on the mid-sternum, about 7.5 cm to both ends [42], respectively, and the positions of contact sensors are shown in Fig. 3.2. In addition, M-P150WSW DAQ (BioPAC systems, Inc., Goleta, CA, USA) was adopted to sample the contact SCG and ECG signals with sample rates of 1000 samples/second. To simultaneously acquire contact sensor signals and radar displacement signals, the data acquisition units of radar system and contact sensor system are synchronized, as shown in the experimental setup block diagram in Fig. 3.2.

Eight healthy subjects (male, 29$\pm$4 years, 175$\pm$10 cm, 75$\pm$10 kg) participated in the experiment after being informed of the experimental procedures and signing the consent

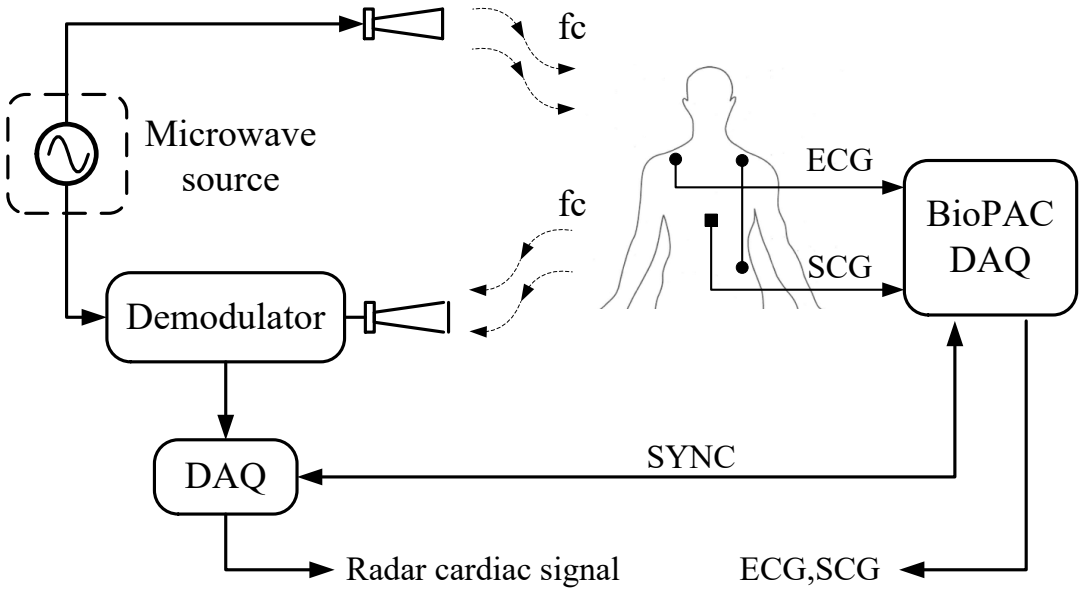

Figure 3.2: Block diagram of the radar and contact sensor system. f_c-carrier frequency; DAQ-data acquisition unit; SYNC-syncronization signal; ECG-electrocardiogram; SCG-seismocardiogram.

form (approved by the Georgia Tech Institutional Review Board). At the beginning of the test, the cardiac signals of each subject were obtained while the subject sat still on a chair for 120 seconds, as shown in Fig. 3.3. Then a 90-second exercise stepping up and down a 21.6-cm wooden frame as quickly as possible was implemented to perturb the physiology of the subject. Subsequently, the subject sat still for 120 seconds for recording the signal in the recovery state, as the cardiovascular system returned from the perturbed state back to rest. Since artificial body movements interrupt the acquisition of cardiac signals, subjects were asked to remain still and reduce activities such as gestures and body movements during data acquisition. SCG, ECG, and radar displacement signals were recorded simultaneously; the ECG was used as a reference for heart beat segmentation, and for calculation of pre-ejection period (PEP).

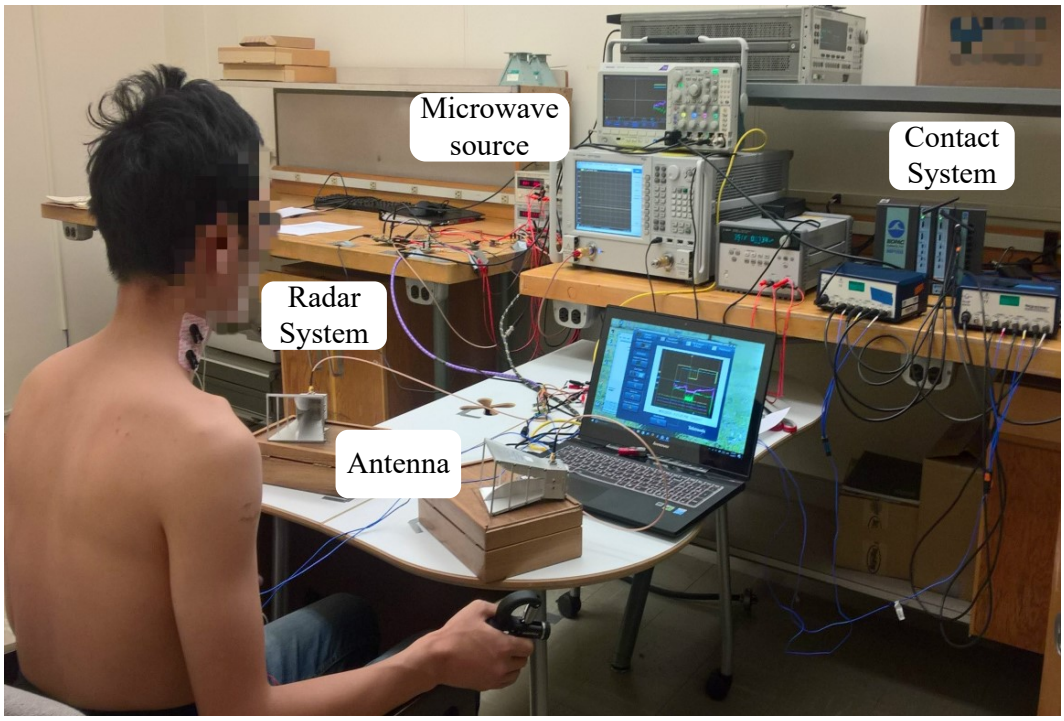

Figure 3.3: Photo of system setup for detecting the cardiac signals.

3.2 Experimental Evaluation

3.2.1 Signal Processing of Radar Signal

After arctangent demodulation [18], which is adopted to reduce the harmonics and signal distortion in (3.1) and (3.2), the RAW is compared with SCG_{DV}. Before the comparison, to improve the quality of the cardiac signals, bandpass filters are applied to ECG, SCG and RAW signals for removing out-of-band interference and noise. The bandpass filters applied to ECG, SCG and RAW signals are finite impulse response (FIR) filters (Kaiser window) with a passband of 3-45 Hz, 0.8-35 Hz and 0.8-35 Hz, respectively. Then the SCG and RAW are segmented into beats using the ECG R-peaks as reference. Beats of SCG and RAW signals are averaged to reduce the effect of random noise. The ensemble averages of ECG, SCG, and RAW over 110 seconds in the rest state are shown in Fig. 3.4 (a) for a representative subject.

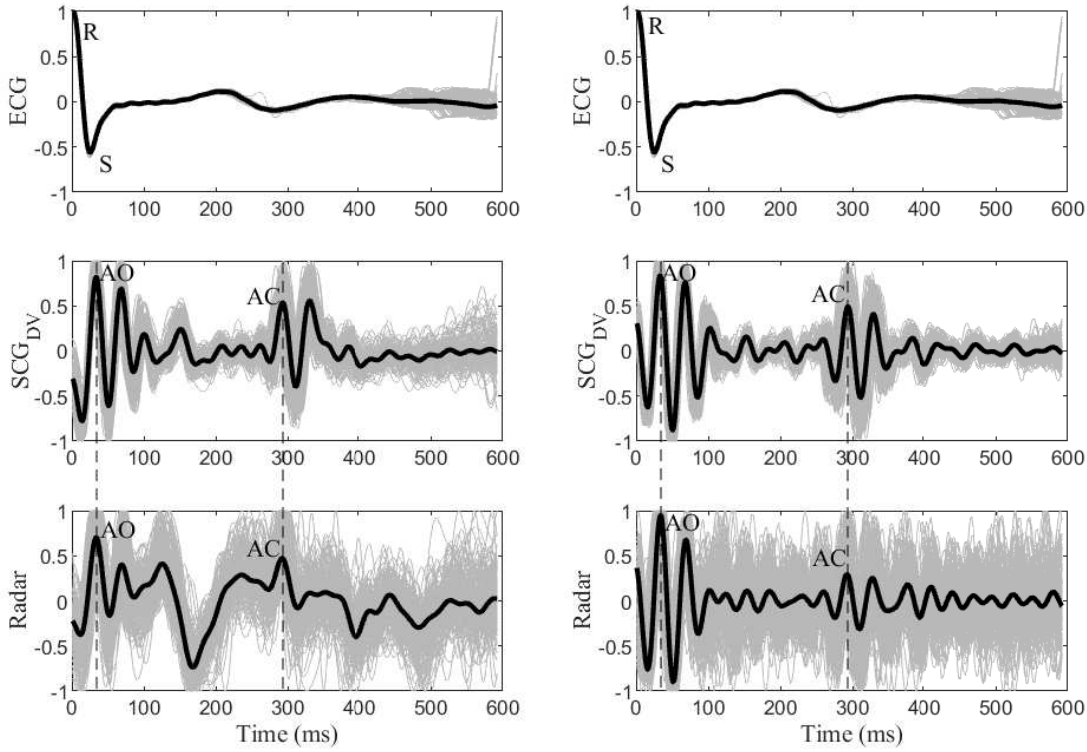

(a) 0.8-35 Hz

(b) 18-35 Hz

Figure 3.4: Cardiac waveforms for subject 1.

Since the interference from harmonics and signal distortion mainly exists in the lower frequency band, as indicated by the theoretical analysis of radar displacement signals in Section 3.1.1 and confirmed by the RAW in Fig. 3.4 (a), SCG and RAW signals are also bandpass filtered by the FIR filter with a passband of 18-35 Hz, and the corresponding ensemble averages of the waveforms over the 110 seconds are shown in Fig. 3.4 (b).

From Fig. 3.4, we can see that the morphologies of SCG_{DV} in the 0.8-35 Hz and 18-35 Hz frequency bands are different and more obvious differences for RAW in the two frequency bands can be observed. Additionally, an improvement of similarity in morphology between SCG_{DV} and RAW in 18-35 Hz is observed, which implies the interference of harmonics and signal distortion in the lower frequency band of RAW. Although the arctangent demodulation approach is adopted to reduce the harmonics and signal distortion, the dif-

ficulty in accurately determining the DC offset for arctangent demodulation decreases the performance of this approach and makes it infeasible to completely eliminate the harmonics and signal distortion.

In addition, the morphologies of SCG_{DV} and RAW have a high similarity in the 18-35 Hz frequency band as shown in Fig. 3.4. It is expected that this frequency band might be less affected by radar interference and more reliable for analyzing cardiac activity using radar signals. However, before using this frequency band for further analysis, it needs to be verified that important cardiac features of interest remains in the higher frequency band, such as the systolic time intervals (STIs) that are determined by the locations of points corresponding to aortic valve opening (AO) and aortic valve closing (AC).

3.2.2 Effectiveness of Fiducial Point Determination in 18-35 Hz

We first evaluate the locations of SCG_{DV} AO ($AO_{SCG_{DV}}$) and SCG_{DV} AC ($AC_{SCG_{DV}}$) of the ensemble averaged SCG_{DV} waveform in both frequency bands relative to the R point of ECG. For 7 out of 8 subjects, the locations of $AO_{SCG_{DV}}$ and $AC_{SCG_{DV}}$ are identified for waveforms in both the 0.8-35 Hz and 18-35 Hz frequency bands. The results are shown in Table 3.1. For subject 4, only the $AO_{SCG_{DV}}$ locations are provided since the $AC_{SCG_{DV}}$ are too weak to be identified in both frequency bands.

The paired-t test for $AO_{SCG_{DV}}$ and $AC_{SCG_{DV}}$ in Table 3.1 gives the two-tailed P values of 0.44 and 0.29, respectively, which indicates there is no statistically significant difference for their locations determined from waveforms in 18-35 Hz and 0.8-35 Hz, wherein 0.8-35 Hz is a typical band used for SCG analysis. All eight subjects have $AO_{SCG_{DV}}$ in 18-35 Hz located within 2 ms of those in 0.8-35 Hz. Similarly, in 18-35 Hz, $AC_{SCG_{DV}}$ for 6 out of the 7 subjects who show clear $AC_{SCG_{DV}}$ are located within 2 ms of those in 0.8-35 Hz, and subject 2 has a deviation of 4 ms. This indicates that SCG_{DV} in 18-35 Hz can be used to effectively estimate the locations of fiducial points and STIs for the healthy young subjects in this study. This is further confirmed by previous researchers who have claimed that SCG

over 18 Hz may be related to closure of cardiac valves and the flow of blood through or near the heart [43, 44].

We then manually analyzed the RAW AO (AO_{RAW}) and RAW AC (AC_{RAW}) locations of the ensemble averaged RAW waveform for both frequency bands, and the results are also included in Table 3.1. In 0.8-35 Hz, six of the eight subjects have the corresponding AO_{RAW} located within 2 ms of $AO_{SCG_{DV}}$, and the AC_{RAW} of four subjects are within 2 ms of $AC_{SCG_{DV}}$. Additionally, the AC_{RAW} for subject 4 cannot be identified, similar to the $AC_{SCG_{DV}}$ of this subject. This indicates that the RAW in 0.8-35 Hz may be used to effectively estimate the SCG fiducial points and analyze the cardiac activity if low-frequency interference can be removed. But the location of AO_{RAW} still has deviations over 3 ms for two subjects, and that of AC_{RAW} deviates over 3 ms for two subjects. For subject 6, the RAW fails to display an AC_{RAW} corresponding to $AC_{SCG_{DV}}$, which might be ascribed to radar noise.

After the signals are bandpass filtered using the 18-35 Hz band, seven out of the eight subjects have AO_{RAW} within 2 ms of $AO_{SCG_{DV}}$, and only subject 3 has a location deviation over 3 ms. Even though AC_{RAW} are still not easily identified for subjects 4 and 6, the location deviations of AC_{RAW} from the corresponding $AC_{SCG_{DV}}$ for 5 of 8 subjects are within 2 ms, and for subject 2 it is reduced to 4 ms from 10 ms. These results show that RAWs in 18-35 Hz have improved signal quality in determining fiducial points, in addition to better representation of the morphology. Therefore, we will use this frequency band for the following signal analysis in this chapter.

3.2.3 Similarity between RAW and SCG_{DV}

To further analyze the similarity between RAW and SCG_{DV}, the cross-correlation coefficients are calculated between their ensemble averages of all beats for eight subjects, and the results are shown in Table 3.2. It shows that five subjects can achieve cross correlation coefficients over 0.9, two subjects are within the range of 0.8-0.9, and subject 3 has a coefficient of 0.72. Thus, the RAW has a high similarity to SCG_{DV} and can effectively represent

Table 3.1: The AO and AC locations of SCG_{DV} and RAW at 0.8-35 Hz and 18-35 Hz (unit: ms).

Subject	AO 0.8-35		AO 18-35		AC 0.8-35		AC 18-35	
	SCG_{DV}	RAW	SCG_{DV}	RAW	SCG_{DV}	RAW	SCG_{DV}	RAW
No.1	34	34	33	34	293	292	294	293
No.2	35	42	33	34	292	302	293	297
No.3	28	24	29	25	326	323	328	330
No.4	35	36	36	37	NA	NA	NA	NA
No.5	40	41	38	39	322	322	322	323
No.6	38	36	38	36	344	NA	344	NA
No.7	49	50	50	50	332	333	332	330
No.8	43	44	42	42	317	318	316	315

Table 3.2: Evaluation of cross correlation and AO location.

Subject	Cross Correlation	Mean		STD		RMSD	N
		SCG_{DV}	RAW	SCG_{DV}	RAW		
No.1	0.92	33	34	1.52	2.19	1.47	162
No.2	0.83	33	35	0.68	0.87	1.95	124
No.3	0.72	29	25	1.18	1.61	4.18	141
No.4	0.95	36	36	1.11	1.73	1.17	137
No.5	0.96	38	39	1.12	1.57	1.58	125
No.6	0.86	38	36	0.83	1.93	3.46	129
No.7	0.94	49	50	0.96	1.64	1.25	113
No.8	0.93	42	42	0.60	1.18	1.05	126

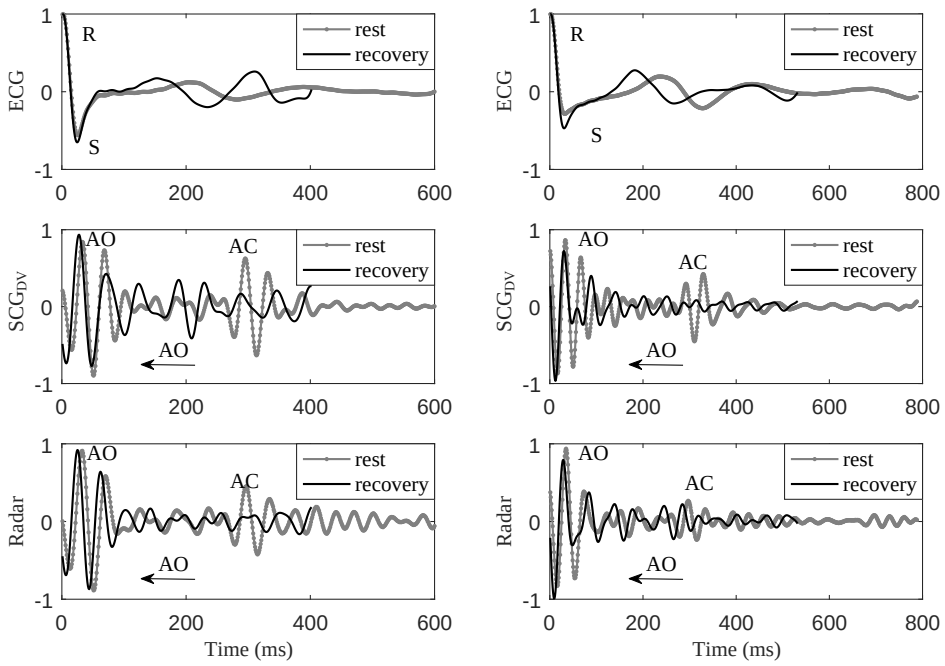

(a) subject 1

(b) subject 2

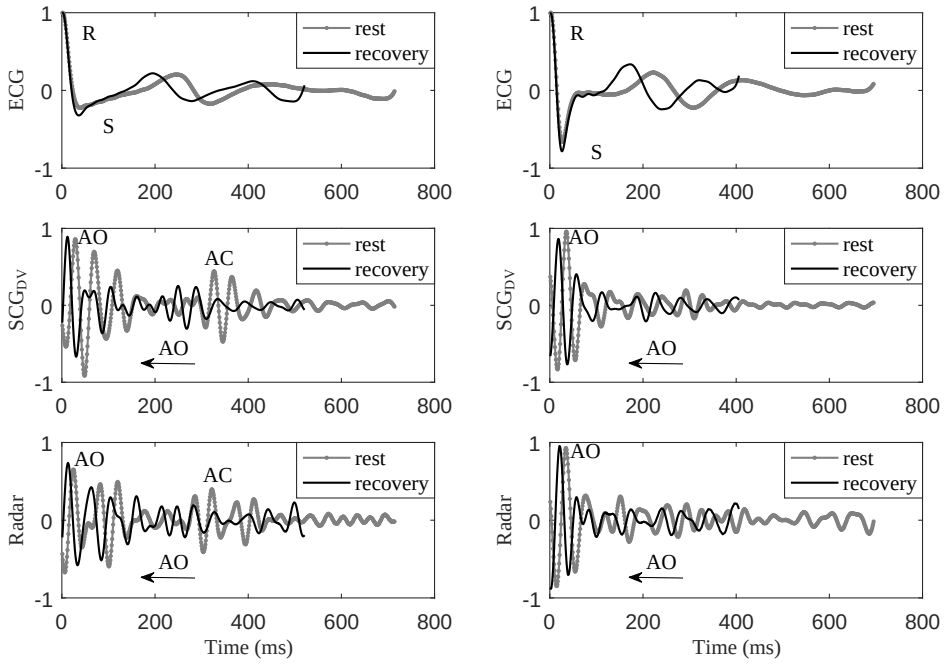

(c) subject 3

(d) subject 4

Figure 3.5: Cardiac waveforms before and after perturbation for subjects 1-4.

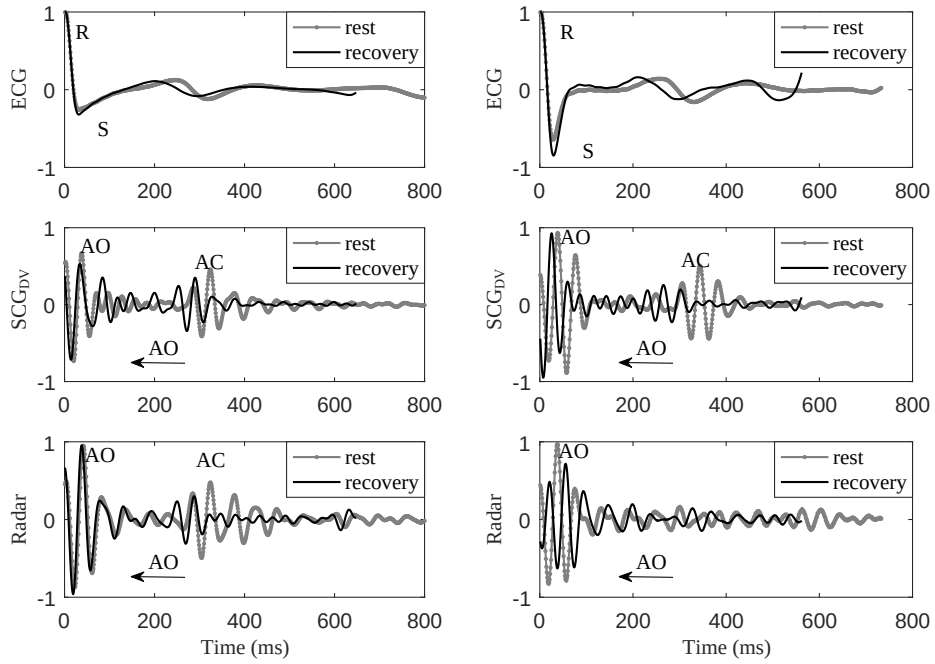

(a) subject 5

(b) subject 6

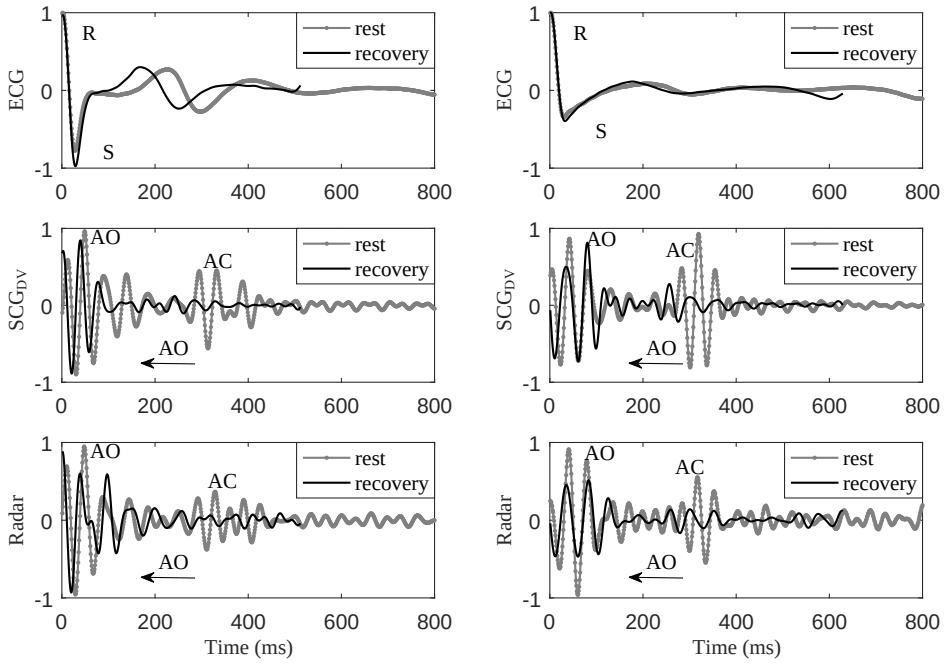

(c) subject 7

(d) subject 8

Figure 3.6: Cardiac waveforms before and after perturbation for subjects 5-8.

SCG_{DV} in morphology.

In addition to morphology, the fiducial points of RAW and SCG_{DV} are compared by evaluating the locations of AO_{RAW} and $AO_{SCG_{DV}}$ for heart beats in a 110-s time window, including the mean and standard deviation (STD) of AO_{RAW} and $AO_{SCG_{DV}}$ locations, and root mean square deviation (RMSD) between locations of AO_{RAW} and $AO_{SCG_{DV}}$. To reduce the effect of random noise on the location of fiducial points, every five beats of RAW and SCG_{DV} in the 110-s time window are averaged to obtain new RAW and SCG_{DV} beats [45, 46], respectively. $AO_{SCG_{DV}}$ is detected from the timing of the minimum or maximum absolute magnitude in the first 200 ms of the new SCG_{DV} beat [42, 47]. The peak of the new RAW that is closest to the corresponding $AO_{SCG_{DV}}$ is selected as AO_{RAW}. The evaluation results of AO_{RAW} and $AO_{SCG_{DV}}$ locations for all eight subjects are shown in Table 3.2 and discussed below. Here, evaluation of AC location is not implemented since it is still a challenge to automatically and accurately annotate $AC_{SCG_{DV}}$ for beat-to-beat analysis over a long period of time.

As expected, the number of beats (N) in the fixed time window is different for different subjects due to different heartbeat rates. For 7 of 8 subjects, the mean values of AO_{RAW} locations are within 2 ms of $AO_{SCG_{DV}}$, similar to the comparison in Table 3.1. Note there is a slight difference between the mean of AO_{RAW} or $AO_{SCG_{DV}}$ location of all new beats and AO_{RAW} or $AO_{SCG_{DV}}$ location of the ensemble averaged waveform of all beats in Table 3.1, due to different calculation methods.

The STDs of AO_{RAW} locations are larger than those of $AO_{SCG_{DV}}$ locations for all human subjects. This may be the results of inadvertent artificial movements during the test, such as coughs, swallow activity and gestures. These movements have more influence on RAWs than on the contact SCG signals since radar signals are more sensitive to the body movements than accelerometers.

The RMSDs of 6 subjects are less than 2 ms, which is defined as a variation tolerance in automatic fiducial point annotation [31]. Thus, AO_{RAW} of these six subjects can correctly

estimate $AO_{SCG_{DV}}$ within the acceptable variation tolerance. For the other two subjects, RMSDs exceed 3 ms, especially subject 3 whose RMSD is over 4 ms, which might be due to the aforementioned artificial movements.

Thus, the analysis above demonstrates that the RAW can effectively represent the SCG_{DV} in both morphology and timing features in the frequency band of 18-35 Hz.

3.3 Time Shift of Fiducial Points under Perturbation

The time shift of fiducial points can represent the abnormality of the heartbeat [48], and some perturbations can be applied to induce this shift as these perturbations bring variability in cardiac activity. Based on our preliminary work in [49], RAWs have the capability of estimating the time shift direction of signal peaks due to the perturbation of handgrip or cold pressor. However, since the time shifts caused by handgrip and cold pressor were small and the analysis was conducted in a frequency band that is prone to low frequency interference such as harmonics and signal distortion, the results were inconclusive. Thus, a further investigation is conducted to verify whether the RAW can capture the time shift due to physiological perturbation.

As described in the experimental setup, after the precordial vibrations were recorded, each subject was asked to make a 90-second stepping exercise. This intense exercise could lead to significant changes of the cardiac activity, resulting in obvious time shift of waveform peaks.

The ensemble averages of both RAW and SCG_{DV} in the "rest" and "recovery" states are shown in Figs. 5 and 6 for all subjects. The gray line "rest" corresponds to the ensemble average of 30-second measurement before exercise and the black line "recovery" is the ensemble average over the 30-second recording after exercise. Signals recorded during exercise are disregarded, as the RAWs are severely interrupted by the human movement and are unable to provide effective information.

In Figs. 3.5 and 3.6, the "rest" waveforms have significant longer periods than of the

Table 3.3: Time shifts of AO_{RAW} and $AO_{SCG_{DV}}$ (unit: ms).

Subject	No.1	No.2	No.3	No.4	No.5	No.6	No.7	No.8
SCG_{DV}	6	3	17	17	4	13	9	7
RAW	8	6	12	15	4	13	9	6

corresponding "recovery" waveforms, which reflects that the intense exercise greatly accelerates the heartbeat rate and brings obvious time shift of waveform peaks. After the exercise, the peaks of both SCG_{DV} and RAW exhibit time shift to the left, which demonstrates that the RAW can be used to correctly estimate the shift direction of waveform peaks.

Time shift of waveform peaks can be used to estimate the change of STIs, and the time shift of AO point corresponds to the change in PEP. As PEP is modulated primarily by sympathetic nervous system (SNS) and a decrease in PEP is associated with an increase in SNS activity and myocardial contractility [50], changes in PEP can be potentially used to evaluate the cardiac activity and predict cardiac diseases. The time shifts of AO_{RAW} and $AO_{SCG_{DV}}$ for all 8 subjects are shown in Table 3.3.

The left shift of AO indicates a decrease in PEP. Each subject in Table 3.3 shows a different decrease of PEP under the perturbation of exercise, which may be due to the health condition and the intensity of exercise for the subject. The decrease of PEP derived from RAW is within 2 ms of that determined from SCG_{DV} for six out of eight subjects, and deviates 3 ms for one subject. This demonstrates that the RAW, similar to SCG_{DV}, can capture cardiac changes in response to the exercise perturbation, and can be used to effectively represent the variability of PEP. A special case in Table 3.3 is subject 3, which is in accordance with its relatively worse performance in terms of the cross correlation coefficient and RMSD. As mentioned before, involuntary activities, such as cough and swallow, may have decreased the performance of RAW for that subject.

3.4 Conclusion

The microwave Doppler radar can detect cardiac activities contained in the precordial vibrations without attaching any sensor to the skin surface. In the frequency band 18-35 Hz, the cross correlation coefficients between RAW and SCG_{DV} are over 0.9 for 5 of the 8 subjects and a minimum of 0.72 for one subject who may have experienced interference during the experiment, representing their high similarity in morphology. For the fiducial points in the 110-second cardiac signal, the RAW can correctly provide the locations of AO_{RAW} with a root mean square deviation from $AO_{SCG_{DV}}$ less than 2 ms for 6 of the 8 subjects. In addition, compared with SCG_{DV}, the RAW can provide correct time shift directions of peaks for all subjects after going through the perturbation of stepping exercise, and estimate the decrease of PEP with an error within 2 ms for 6 out of the 8 subjects. These results demonstrate that the RAW can effectively represent SCG_{DV} and capture change of cardiac activities responding to physiological perturbation.

However, some differences still exist between RAW and SCG_{DV}, which might be ascribed to the fact that the radar-based approach records precordial vibrations within an area covered by the antenna instead of at a specific location as that of the contact approach. Additionally, a limitation of only male subjects exists in this experimental setup and the measurement is not purely non-contact since we still need to use ECG for the beats segmentation. Female subjects and subjects at different ages are necessary to further verify the effectiveness of radar approach. Independent annotation of fiducial points in RAW without ECG should be explored to achieve a completely non-contact measurement.

CHAPTER 4
THE SCG FEATURE EXTRACTION FROM RADAR SIGNAL WITHOUT CONCURRENT ECG

The similarity between the RAW and dorso-ventral SCG (SCG_{DV}) in the frequency band 18-35 Hz has been verified in the previous chapter. The high similarity in morphology and the fiducial points demonstrates the feasibility of using the microwave Doppler radar for remote sensing of the SCG. In the previous analysis of the RAW, a concurrent ECG is required to segment the RAW and search for the SCG features, such as the fiducial point and the corresponding systolic time intervals (STIs). However, the detection of ECG requires to attach sensors on the skin surface. To achieve completely non-contact detection of SCG using microwave Doppler radar, it is desired to design a feature extraction approach from RAW without concurrent ECG. In this chapter, such a standalone feature extraction method is developed to extract SCG features from RAW.

The rest of the chapter is organized as follows. Section 4.1 discusses the methodology of the approach. Section 4.2 exhibits the experimental results and discusses the performance of the methodology. Section 4.3 gives the conclusion.

4.1 Methodology of Standalone Feature Extraction

4.1.1 Data Acquisition

The microwave Doppler radar system had the same setup as that described in [51], and antennas were 50 cm away from the human subject as shown in Fig. 4.1. The I/Q radar signals were recorded from the radar system through the AD7770 data acquisition unit (DAQ). The ECG was also recorded using a BN-RSPEC and a MP150WSW DAQ (BioPAC Systems, Inc., Goleta, CA, USA) as a reference signal for heartbeat segmentation

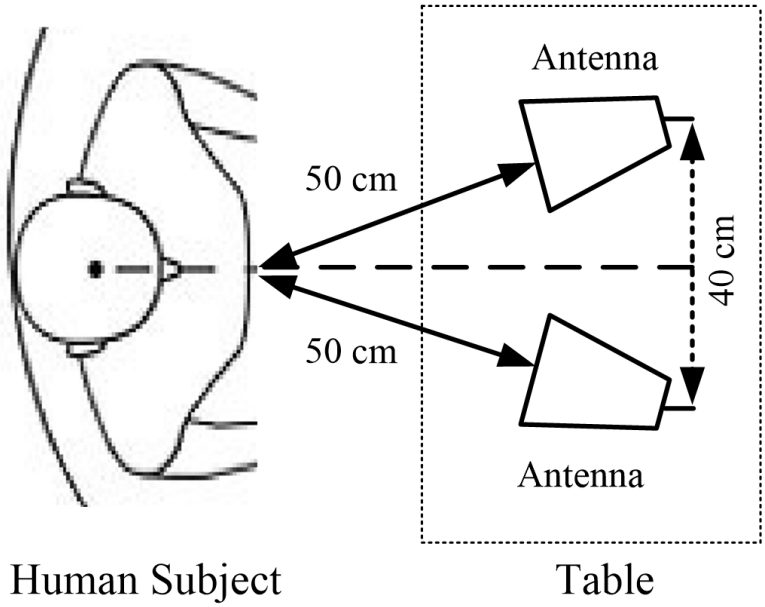

Figure 4.1: Radar system setup for detecting the cardiac signals.

and fiducial point detection. The MP150WSW and AD7770 DAQs were synchronized to sample the ECG and radar signals simultaneously with the same sampling rate of 1000 samples/second.

A total of 22 individuals volunteered to participate in the experimental measurement, including 10 female adults (Age: 32.40$\pm$10.81 years, Height: 163.88$\pm$2.80 cm, and Weight: 55.75$\pm$4.61 kg) and 12 male adults (Age: 34.17$\pm$10.60 years, Height: 177.38$\pm$5.01 cm, and Weight: 77.61$\pm$7.09 kg). Before the experiments, all the participants were informed of the experimental procedures, and signed the consent forms (approved by the Georgia Tech Institutional Review Board). Each of the volunteers was asked to sit on the chair for 120 seconds for acquiring the cardiac signals in the rest state with normal breathing. Additionally, the subjects were asked to stay still to reduce motion artifacts during the measurements, such as gestures, swallow activity and other body movements.

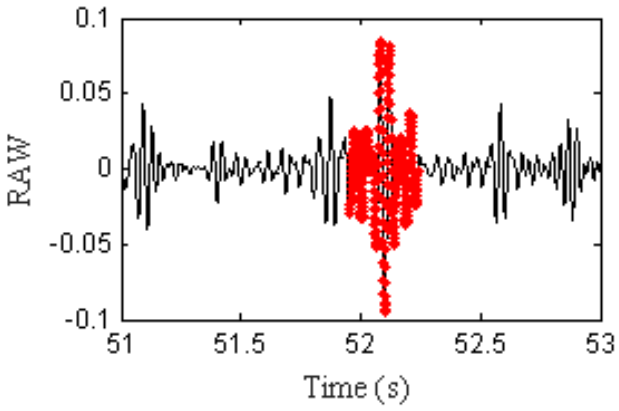

Figure 4.2: Interference in the RAW signal, with interference marked with red dots.

4.1.2 Signal Processing and Reference Signal for RAW

Pre-processing and Linear Filtering

The radar displacement signals were obtained from the recorded I/Q radar signals through the arctangent approach [18]. Then the RAW signal was obtained by taking the second derivative of radar displacement signal, which is an acceleration signal similar to SCG_{DV} [51]. The first and last 10 seconds were disregarded to remove the possible interferences at the beginning and end of the recording process. Thus, RAW signals of 100 seconds were analyzed for each subject.

Severe interferences due to motion artifacts such as unintentional body movement and coughs can distort the RAW signal and make it impossible to extract effective cardiac information. Typically, these interferences could result in a much higher power level than the normal cardiac signals [52]. A sliding window of length 500 ms and a threshold twice the median value of the power envelope were used to mark the interfered signals, as shown in Fig. 4.2. These marked interfered signals were discarded before further analysis.

After removing the segments corrupted with obvious motion artifacts, both the ECG and RAW signals were filtered with finite impulse response (FIR) filters (Kaiser window) to remove noises with pass bands of 3-45 Hz and 18-35 Hz, respectively. The pass band of 18-35 Hz was selected for filtering RAW signal based on the previous work by Xia et

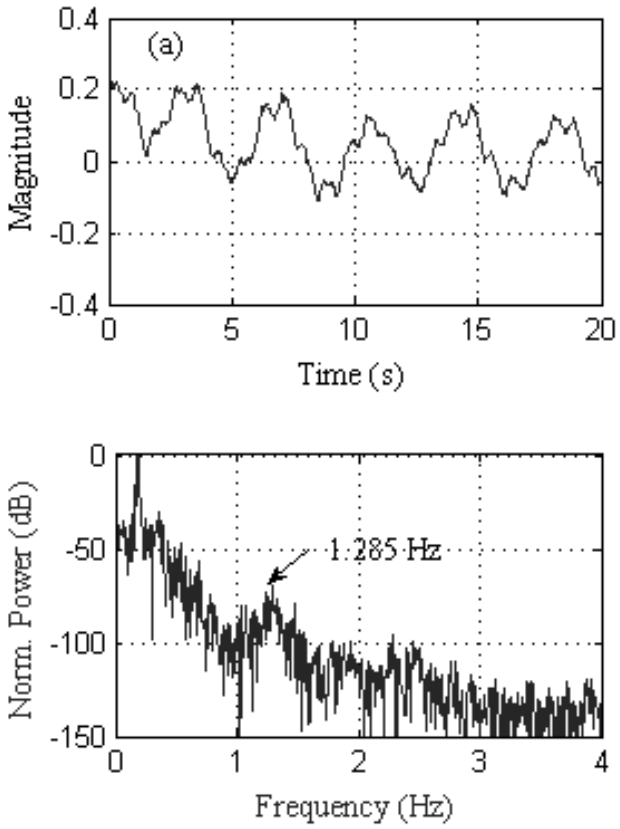

Figure 4.3: Radar displacement signal in (a) the time domain, and (b) the frequency domain.

al. [51]. It was demonstrated that the RAW signal in the pass band of 18-35 Hz had a good similarity to SCG_{DV} in morphology and timing features.

Generation of Reference Signal

A reference signal was derived to delineate the RAW signals. This reference signal was named as radar displacement signal of heartbeat (RDH), which is the displacement signal corresponding to the heartbeat that is much smaller than and is superimposed on the respiration signal as shown in Fig. 4.3 (a). To extract the RDH signal, a complex Fourier transform (CFT) was first applied to the recorded radar displacement signals to eliminate the harmonics and signal distortion in the spectrum [17]. As shown in Fig. 4.3 (b), the spectrum can clearly show the heartbeat component at 1.285 Hz without the surrounding interferences. By searching for the highest peak within the frequency band 0.8 Hz-2.5 Hz

where the heartbeat frequency generally locates [53], the heartbeat frequency (f_{hb}) could be identified. Then, a FIR filter with 0.2-Hz pass band centering on the heartbeat frequency $[f_{hb} - 0.1, f_{hb} + 0.1]$ was applied to the radar displacement signals to extract the RDH signal. This indicates the maximum allowable change of heart rate for the duration of the radar signal that uses a single RDH reference signal is 6 beats per minute. For general applications, wherein the heart rate may vary more than 6 beats per minute over time, the radar recording may be segmented into multiple sections so that the variation of heart rate is within 6 beats per minute within each section. Then a RDH signal could be extracted from each of the multiple sections using the proposed approach.

4.1.3 Window Selection for Masking Systolic Profile and Searching Fiducial Point AO

For determining the AO location in SCG, the ECG R-wave is typically used as the reference, and the peak of SCG with the maximum absolute magnitude within a 200-ms fixed window is considered as the AO location [42, 47]. This method was applied to RAW, the radar SCG signal, to obtain the accurate AO locations for evaluating the proposed method, which was denoted as $\mathrm{AO_{ECG}}$.

In the proposed method that uses the RDH signal as a reference signal, two windows were determined to mask the systolic profile and search the AO point, respectively. Based on our observation, the peaks of RDH (PRDH) might be at either side of the ECG R-wave. The locations of PRDH relative to the ECG R-wave should be evaluated to correctly build a 300-ms time window for locating the systolic profile. The relative locations of PRDH with respect to the ECG R-wave were analyzed for all heartbeats of each subject. The corresponding standard deviation (STD) and mean value of the interval between PRDH and ECG R-wave could determine the 95% confidence interval and a number *offset1*, which determines a 300-ms time window [*PRDH-offset1, PRDH-offset1+300*] that can mask the major portion of the systolic profile in general cases. After masking the systolic profile in RAW, the envelope of the profile ($\mathrm{ENV_{RDH}}$) was derived through a third order integration

of the masked RAW, and the peak of ENV_{RDH} ($PENV_{RDH}$) should be very close to the AO point [32]. The $PENV_{RDH}$ was found around the location of the corresponding AO_{ECG} which is considered as the true location of AO. The relative location of $PENV_{RDH}$ with respect to AO_{ECG} was evaluated to determine a general search window for AO. The STD and the mean value of the interval between $PENV_{RDH}$ and AO_{ECG} were analyzed to obtain the 95% confidence interval, which could determine an *offset2*. A 200-ms time window [$PENV_{RDH}$-*offset2*, $PENV_{RDH}$-*offset2+200*] can be built to search for the AO_{RDH}. The peak of RAW with the maximum absolute magnitude in this 200-ms fixed window is considered as the AO, denoted as AO_{RDH}. The process for identifying the AO_{RDH} is as shown in Algorithm 1.

Algorithm 1 Identify the fiducial point AO_{RDH}

1: Locate the peaks of RDH (*PRDH*)
2: Use *PRDH* to build 300-ms windows, [*PRDH-offset1, PRDH-offset1+300*]
3: Within the 300-ms window, mask the systolic profile
4: Integrate the masked profile to get its envelope ENV_{RDH}
5: Locate the peaks of ENV_{RDH} ($PENV_{RDH}$)
6: Use $PENV_{RDH}$ to build 200-ms windows, [$PENV_{RDH}$-*offset2*, $PENV_{RDH}$-*offset2+200*]
7: Within the 200-ms window, search for the maximum and obtain AO_{RDH}

Another method using radar acceleration envelopes (RAE) was applied to detect AO based on the work for contact SCG waveform proposed by Khosrow-khavar et al. [35]. In this approach, the peaks of RAE (PRAE) are at least 50 ms before the ECG R-wave, and therefore a fixed window of 300 ms with respect to PRAE [PRAE, PRAE+300] was chosen to mask the systolic profile. Then the envelope of systolic profile (ENV_{RAE}) and its peak location ($PENV_{RAE}$) were derived so that the AO point can be determined using the feature extraction and classification algorithm proposed in [35]. The AO location determined using this method was denoted as AO_{RAE}.

4.1.4 Ensemble Averaged Waveform and LVET

Compared with AO, the automatic delineation of AC is more challenging due to the variations in amplitude and timing of the AC peaks in each heart beat cycle for the conventional SCG [31]. The signal quality of RAW including the amplitude and timing features is affected more by interference and noise when compared with SCG acquired from the contact sensor approach. Thus, the AC points were manually extracted from RAW, which is the first encountered maximum for the diastolic profile [29]. The AC point represents the start of diastole when the pressure inside the ventricle has dropped causing the aortic valve to close abruptly.

For each subject, the 100-second RAW signal was first segmented into heartbeats using four reference points: ECG R-wave, AO_{ECG}, AO_{RAE} and AO_{RDH} separately. The performance of adopting these different reference points were compared afterwards in Section 4.2.4. All the heartbeats were averaged with ensemble averaging techniques to reduce uncorrelated noise [54]. Then, four ensemble averaged RAW heartbeats were obtained for each subject.

After averaging, the AC point on each ensemble averaged waveform was manually marked. The AC_R, AC_{ECG}, AC_{RAE} and AC_{RDH} represent the ACs identified in the ensemble averaged waveforms segmented by ECG R-wave, AO_{ECG}, AO_{RAE} and AO_{RDH}, respectively. LVET was then determined by calculating the AO-AC interval. The LVETs derived from the ensemble averaged waveforms obtained by using ECG R-wave, AO_{ECG}, AO_{RAE} and AO_{RDH} as reference points were denoted as $LVET_R$, $LVET_{ECG}$, $LVET_{RAE}$ and $LVET_{RDH}$, respectively.

4.1.5 Interbeat Interval from AO

Tadi et al. has shown that AO-AO interval of SCG can be used to obtain beat to beat interval (BBI) with a high accuracy when compared with corresponding ECG R-to-R interval [55]. Apart from estimating STIs, studies were also conducted to explore the efficacy of using

the AO points delineated from the RAW signal to estimate BBI. The BBIs calculated using the AO_{ECG}, AO_{RAE} and AO_{RDH} were denoted as BBI_{ECG}, BBI_{RAE} and BBI_{RDH}, respectively. Those BBI values were also compared with the gold standard BBI that is the ECE R-to-R interval and was denoted as BBI_R.

4.2 Experimental Evaluation

4.2.1 The Performance of the Reference Signal RDH

A visual comparison of RAE and RDH with corresponding ECG and RAW signal is given in Fig. 4.4. The RDH signal was compared with the ECG and RAE signals to evaluate its performance. Fig. 4.4 (a) shows an example of good-quality RAW signal whereas Fig. 4.4 (b) gives an example of poor-quality RAW signal. In both cases, the RAE and RDH signals show the same number of cardiac cycles as that of ECG, and each cycle has a major peak that could potentially be used as a reference point similar to the ECG R-wave. The RDH signal has peak locations different from the RAE signal, and contains less tiny fluctuations.

It is obvious that the cardiac cycles cannot be accurately determined from only a RAE signal derived from the relatively low-quality radar signal, as shown in Fig. 4.4 (b). The time interval between adjacent peaks is affected due to the noise and the interferences, and the effectiveness of RAE is severely degraded. This was also demonstrated in [34]. For example, in Fig. 4.4 (b), the fifth peak in RAE is less than 400 ms from its previous peak and should be disregarded, and thus this cardiac cycle could not be identified by RAE. In contrast to the RAE signal, the RDH signal in Fig. 4.4 (b) is showing to be less affected by the noise and can still indicate the cardiac cycles correctly. Since the center frequency of the band pass filter, described in section 4.1.2, is an estimation of the averaged heartbeat, the band pass filtering step reduces the influence of sudden interference.

To further evaluate the performance of RDH and RAE in representing the cardiac cycle quantitatively, the number of detected cardiac cycles using the ECG, RAE and RDH signals was compared for each of the 22 subjects. ECG is the gold standard for identifying cardiac

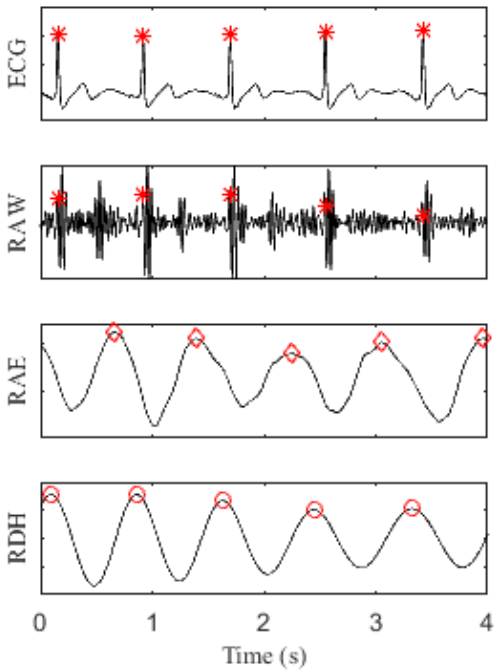

(a) A high-quality RAW

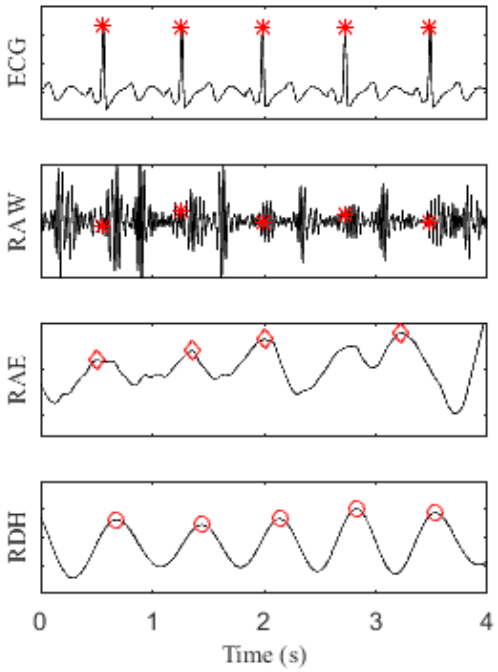

(b) A low-quality RAW

Figure 4.4: ECG, RAE and RDH for the RAW with red stars representing ECG R-peaks, red diamonds indicating the peaks of RAE, and red circles showing the peaks of RDH.

Table 4.1: The detection ratios of cardiac cycles of RAE and RDH.

Subject No.	N	r_{RAE}	r_{RDH}		Subject No.	N	r_{RAE}	r_{RDH}
F01	129	0.96	1.00		M01	113	0.84	0.99
F02	135	0.94	1.00		M02	110	1.00	1.00
F03	102	0.75	0.98		M03	131	0.98	1.00
F04	105	1.00	1.00		M04	125	0.97	1.00
F05	125	0.79	1.00		M05	109	0.93	1.00
F06	128	0.98	1.00		M06	120	0.97	1.00
F07	97	0.70	0.99		M07	124	0.87	1.00
F08	124	0.93	1.00		M08	103	0.80	1.00
F09	98	0.77	1.00		M09	133	0.91	0.99
F10	159	0.84	0.96		M10	157	0.82	0.98
					M11	162	0.88	1.00
					M12	143	0.80	1.00

Note: F and M stand for female and male subjects, respectively. For example, F1 represents the female subject 1.

cycles in healthy people without arrhythmias, and number of cardiac cycles in ECG is denoted as N. The ratio between the number of detected cardiac cycles in RAE and N, r_{RAE}, and the ratio between that in RDH and N, r_{RDH}, are listed in Table 4.1.

As shown in Table 4.1, the RDH signal provides a high average detection ratio of cardiac cycles, 0.995. Among the 22 subjects, it detects the same number of cardiac cycles as that from ECG for 16 subjects, and the detection ratio is over 0.96 for the other 6 subjects. In comparison, the RAE signal achieves an average detection ratio of 0.883, lower than that of RDH, and provides the same number of cardiac cycles as that from ECG for only 2 subjects. Thus, the RDH signal could represent the number of cardiac cycles accurately, and would be promising to locate the systolic profile and the fiducial point.

4.2.2 The Determination of the Time Window

For the heartbeats with PRDH before and after the ECG R-wave, the STD and mean value of the interval between PRDH and ECG R-wave were analyzed to determine the *offset1* value and get the time window [*PRDH-offset1, PRDH-offset1+300*] for masking the systolic profile. Table 4.2 summarizes the number of beats in which PRDH is on the left or

Table 4.2: Evaluation of time interval between PRDH and ECG R-wave.

Subject No.	Age	BMI	Left			Right		
			NL_{PRDH}	Mean (ms)	STD (ms)	NR_{PRDH}	Mean (ms)	STD (ms)
F01	23	19.2	112	-65.77	37.39	17	33.18	31.11
F02	29	21.2	7	-63.71	42.50	128	92.42	48.09
F03	24	22.1	90	-92.02	58.42	10	71.80	115.37
F04	45	22.0	2	-9.50	10.61	103	135.16	42.00
F05	32	19.0	45	-19.40	15.39	113	31.59	22.04
F06	27	19.6	96	-31.46	18.78	32	8.47	6.46
F07	51	22.9	80	-101.04	84.42	13	56.00	81.71
F08	46	20.1	105	-68.63	46.77	19	45.26	57.48
F09	22	22.0	62	-69.26	53.57	36	74.06	65.30
F10	25	19.4	87	-105.36	79.58	65	149.82	111.93
M01	49	21.1	81	-99.96	70.88	31	58.81	68.36
M02	39	23.0	11	-25.82	26.85	99	75.23	33.82
M03	22	25.8	46	-37.78	26.27	85	50.52	38.33
M04	29	26.4	43	-37.35	44.92	82	40.54	30.17
M05	45	28.1	103	-74.06	37.14	6	30.50	19.31
M06	27	24.5	2	-4.00	0.00	118	68.08	35.32
M07	38	27.4	82	-31.79	24.29	42	20.14	21.37
M08	54	24.8	70	-75.49	57.60	33	34.12	25.71
M09	27	23.0	31	-50.16	55.44	101	61.30	41.01
M10	23	24.2	13	-158.15	111.19	141	108.01	54.77
M11	28	24.1	60	-41.57	58.81	102	52.38	53.95
M12	29	23.7	0	0.00	0.00	143	71.87	20.51

Note: Left and Right indicate the PRDH on the left and right of ECG R-wave, respectively.

right of corresponding ECG R-wave (NL_{PRDH} and NR_{PRDH}, respectively) for each subject as well as the mean and STD values of those intervals.

Based on the statistical analysis of confidence interval [56, 57], the 95% confidence interval determined the *offset1* to be 91.3 ms, and a 300-ms time window [*PRDH-91.3, PRDH+208.7*] was selected for masking the systolic profile. Table 4.2 shows that 18 out of 22 subjects have mean values within 91.3 ms, and thus the window could mask the systolic profile in general cases.

After determining the time window for masking the systolic profile, $PENV_{RDH}$ was obtained from the envelope of the masked systolic profile. The intervals between $PENV_{RDH}$

Table 4.3: Evaluation of time interval between $PENV_{RDH}$ and AO_{ECG}.

Subject No.	Left			Right		
	NL_{ENV}	Mean (ms)	STD (ms)	NR_{ENV}	Mean (ms)	STD (ms)
F01	80	-14.34	19.86	45	5.20	4.87
F02	29	-27.10	31.60	77	39.82	29.41
F03	60	-58.10	68.31	33	9.09	6.87
F04	10	-36.70	49.58	64	31.89	27.29
F05	50	-38.50	31.18	100	15.28	14.44
F06	37	-33.84	45.38	81	25.94	17.45
F07	55	-60.78	68.77	21	16.86	10.41
F08	49	-50.63	109.74	33	35.24	26.30
F09	71	-19.73	35.66	20	8.20	15.77
F10	32	-105.03	91.37	38	24.13	31.84
M01	53	-64.55	82.83	35	29.31	28.39
M02	57	-12.58	14.92	44	12.09	21.01
M03	67	-51.32	60.84	47	25.87	19.17
M04	36	-62.61	40.86	54	41.35	28.42
M05	51	-28.22	41.08	51	8.10	12.57
M06	56	-14.77	22.60	59	13.27	12.79
M07	50	-55.88	64.73	47	34.26	28.55
M08	70	-29.97	38.70	14	19.36	14.73
M09	72	-50.54	46.67	51	30.20	25.29
M10	26	-44.85	58.29	47	41.68	42.45
M11	77	-46.25	46.65	57	27.28	26.28
M12	83	-3.92	8.64	53	2.11	1.96

Note: Left and Right indicate the $PENV_{RDH}$ on the left and right of AO_{ECG}, respectively.

and AO_{ECG} were evaluated to determine the time window [$PENV_{RDH}$-*offset2*, $PENV_{RDH}$-*offset2*+*200*]. Table 4.3 shows the mean and STD values of the intervals and the number of $PENV_{RDH}$ points on the left (NL_{ENV}) or right (NR_{ENV}) of AO_{ECG} points for each subject.

As shown in Table 4.3, $PENV_{RDH}$ may locate on the right of the AO_{ECG}, with an averaged mean value of 23 ms and STD of 23 ms or on the left with an averaged mean value of 39 ms and STD of 53 ms. The *offset2* was determined to be 32.6 ms by calculating the 95% confidence interval, and a 200-ms time window of [$PENV_{RDH}$-*32.6*, $PENV_{RDH}$+*167.4*] was selected to search for AO_{RDH}.

Table 4.4: The detection ratios of AO_{RAE} and AO_{RDH}.

Subject No.	AO_{RAE}	AO_{RDH}		Subject No.	AO_{RAE}	AO_{RDH}
F01	0.60	0.98		M01	0.38	0.82
F02	0.49	0.85		M02	0.79	0.96
F03	0.24	0.94		M03	0.34	0.90
F04	0.46	0.77		M04	0.52	0.98
F05	0.56	0.99		M05	0.61	0.97
F06	0.44	0.97		M06	0.81	0.99
F07	0.27	0.88		M07	0.30	0.90
F08	0.44	0.87		M08	0.52	0.96
F09	0.53	0.95		M09	0.39	0.97
F10	0.14	0.65		M10	0.38	0.55
				M11	0.51	0.96
				M12	0.55	0.99

4.2.3 Evaluation of the Fiducial Point AO

The detection ratios of AO_{RAE} and AO_{RDH} for each subject were assessed to demonstrate the detection accuracy. Here, the detection ratio indicates the percentage of number of AO_{RAE} or AO_{RDH} that are at the same locations as that of the corresponding AO_{ECG}. The results for 10 female and 12 male subjects are presented in Table 4.4.

Based on the results in Table 4.4, AO_{RDH} achieves an average detection ratio of 90%. Among all the 22 subjects, 20 subjects have the detection ratios over 75%, in which 15 of them are over 90%. Only 2 subjects have the detection ratios between 50% and 75%. For the case of AO_{RAE}, the average detection ratio is 47% and only 2 subjects could represent the AO_{ECG} with a detection ratio over 75%. Among the other 20 subjects, for 8 subjects the detection ratios are between 50% and 75%, for 11 subjects the ratios are between 25% and 50%, and for the subject F10 the detection ratio is below 25%. The results demonstrate that AO_{RDH} could achieve a good representation of AO_{ECG}, and improve the average detection ratio by 43% when compared with AO_{RAE}.

The superior performance of AO_{RDH} compared with AO_{RAE} is due to the high quality of the RDH signal that leads to a higher detection ratio of cardiac cycles, as demonstrated in Section 4.2.1. This in turn helps to obtain more accurate systolic profiles using RDH,

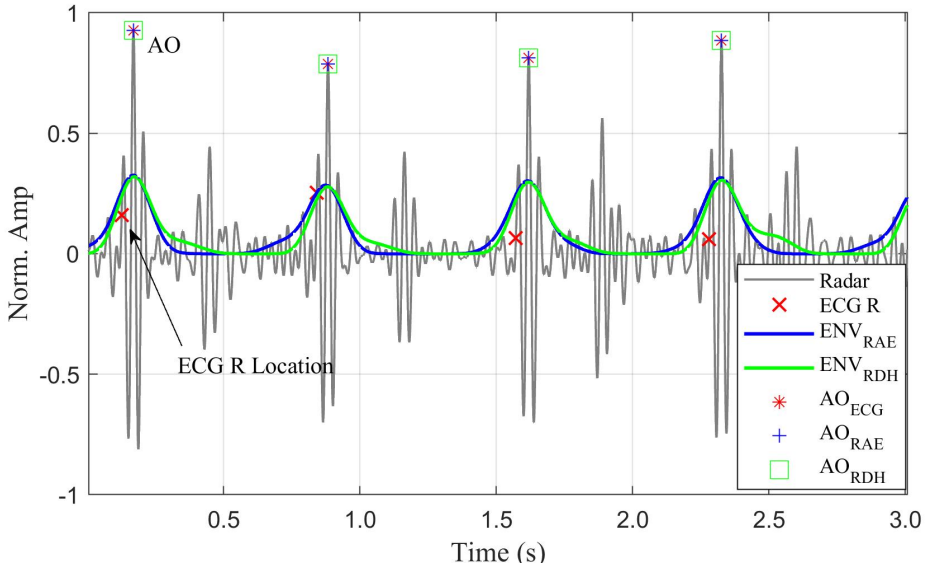

(a) High-quality RAW

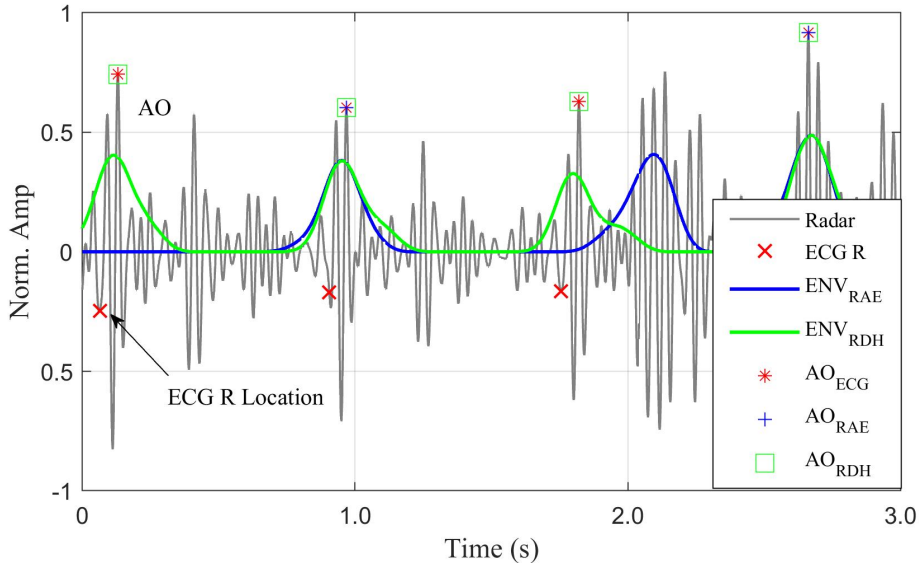

(b) Low-quality RAW

Figure 4.5: Detection of fiducial point AO using ECG, RAE and RDH for radar signals.

which is further demonstrated visually in Fig. 4.5. In Fig. 4.5 (a), a high-quality RAW signal is presented with the corresponding AO_{ECG}, AO_{RAE} and AO_{RDH} marked. In addition, the ECG R-wave location, ENV_{RAE} and ENV_{RDH} were also marked and displayed. The figure shows that each ECG R-wave locates before the corresponding AO, while the peaks of ENV_{RAE} and ENV_{RDH} are very close to the corresponding AO point. The AO localization

methods based on the peaks of ENV_{RAE} and ENV_{RDH}, as discussed above, can accurately locate AO_{RAE} and AO_{RDH}, respectively, which are at the same locations as that of AO_{ECG}. However, when the signal quality of RAW decreases, as shown in Fig. 4.5 (b), the RAE approach fails to detect some AO points while the RDH approach could still reliably identify all AO points, which demonstrates the robustness of the RDH approach to the noise.

4.2.4 Evaluation of the Ensemble Averaged Waveform and LVET

The ensemble averaged waveform for one subject is shown in Fig. 4.6. Fig. 4.6 (a) is the ensemble average of the beats segmented using the ECG R-wave. The fiducial points AO and AC are clearly observed, and the ensemble average exhibits high signal quality. The waveforms in Figs. 4.6 (b), (c) and (d) correspond to the ensemble average of beats segmented using AO_{ECG}, AO_{RAE} and AO_{RDH}, respectively.

The morphology of Fig. 4.6 (b) is very similar to that of Fig. 4.6 (a), except that the starting point is AO_{ECG} instead of ECG R-wave. After removing the part before AO_R of Fig. 4.6 (a) and the corresponding number of points at the end of Fig. 4.6 (b), the averaged waveforms in Figs. 4.6 (a) and (b) have a cross correlation coefficient of 0.97. The high similarity of the averaged waveforms indicates that the beat segmentation with AO could also effectively represent the ensemble averaged waveform.

The averaged waveform in Fig. 4.6 (d) has a cross correlation coefficient of 0.99 to that in Fig. 4.6 (b), which is higher than the coefficient of 0.95 between the waveforms in Figs. 4.6 (b) and (c). Thus, compared with Fig. 4.6 (c), the averaged waveform in Fig. 4.6 (d) has higher similarity to Fig. 4.6 (b) in morphology, especially the diastolic profile. This is because the AO_{RDH} has a higher detection ratio, and thus reduces the number of beats that are not starting from the correct AO locations. The beats starting from inaccurate AO points degrade the morphology of the ensemble averaged waveform, as observed in Fig. 4.6 (b) at around 200 ms.

To evaluate the performance of using different reference signals for estimating LVETs,

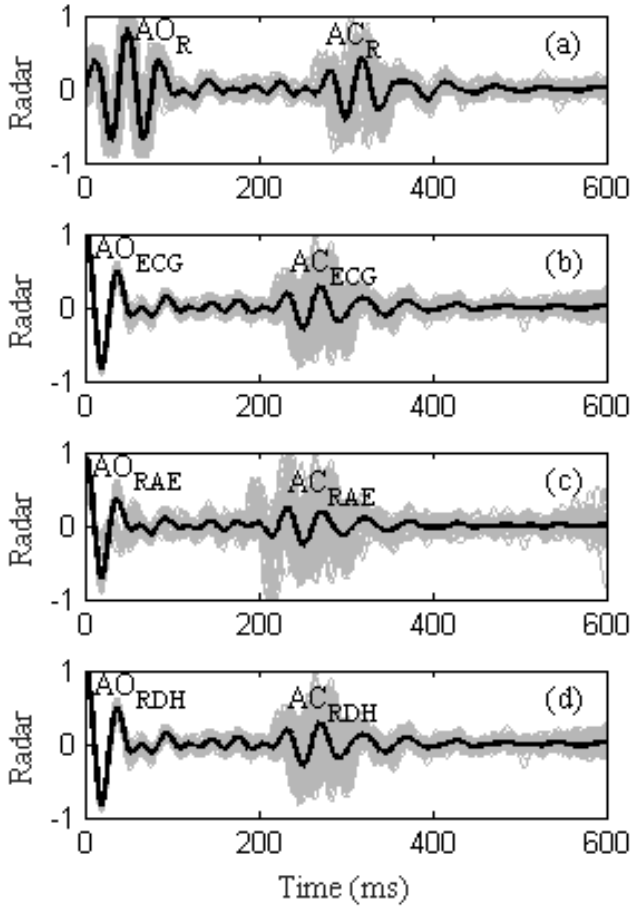

Figure 4.6: The averaged RAW waveform starting from (a) ECG R-wave, (b) AO_{ECG}, (c) AO_{RAE} and (d) AO_{RDH}.

LVETs for each subject were calculated from AOs and ACs marked on the corresponding ensemble averaged waveforms. The comparison of LVETs obtained using four reference signals/points (ECG R-wave, AO_{ECG}, AO_{RAE} and AO_{RDH}) are given in Table 4.5.

For subjects F03, F10 and M07, ACs could not be identified from the ensemble averaged RAW waveforms and thus the corresponding LVETs are not available in Table 4.5. For the other 19 subjects, the $LVET_R$ are detected and the range is from 207 ms to 360 ms. Compared with the $LVET_R$, the $LVET_{ECG}$ is within 2 ms of $LVET_R$ for 14 subjects and within 5 ms for 2 subjects. For the other 3 subjects, ACs are undetectable on the ensemble averaged waveform due to the limited quality of RAW, and thus $LVET_{ECG}$ are not avail-

Table 4.5: The LVET derived from the ensemble averaged RAW (Unit: ms).

Subject No.	$LVET_R$	$LVET_{ECG}$	$LVET_{RAE}$	$LVET_{RDH}$
F01	335	338	338	338
F02	290	295	295	295
F03	N/A	N/A	N/A	N/A
F04	319	320	323	318
F05	280	278	280	279
F06	294	295	295	295
F07	360	359	357	361
F08	287	N/A	N/A	N/A
F09	346	347	347	347
F10	N/A	N/A	N/A	N/A
M01	323	323	324	323
M02	291	290	290	291
M03	280	N/A	N/A	N/A
M04	307	306	N/A	306
M05	286	288	288	288
M06	277	277	278	277
M07	N/A	N/A	N/A	N/A
M08	315	317	316	317
M09	256	258	257	258
M10	259	260	260	261
M11	207	N/A	N/A	N/A
M12	271	270	271	270

able. This indicates that the beat segmentation with AO can be used to estimate LVET with limited errors.

The $LVET_{RDH}$ has almost the same results as that of the $LVET_{ECG}$. For each detected $LVET_{ECG}$, the corresponding $LVET_{RDH}$ is within 2 ms. The $LVET_{RAE}$ could also achieve good performance, but F04 has a deviation over 2 ms and the method does not provide a LVET value for M04. These results demonstrate that $LVET_{RDH}$ could perform as well as $LVET_{ECG}$, and has better performance than $LVET_{RAE}$.

4.2.5 Evaluation of Interbeat Interval from AO

BBIs calculated from AO-AO intervals are compared with the gold standard BBI_R for one subject with a 30-second plot shown in Fig. 4.7. The variation of the BBI_R and BBI_{ECG} with time demonstrates the respiratory trends congruent with physiological mechanisms of respiratory sinus arrhythmia [58]. The BBI_{RAE} and BBI_{RDH} also indicate the similar results and follow the respiratory trends. In Fig. 4.7, the BBI_{RDH} are the same as the BBI_R except the two points at the beginning of the plot, while the BBI_{RAE} has relatively large errors at 7 points. This is also exhibited in their RMSDs from the BBI_R, which are 6.55 ms and 64.52 ms for BBI_{RDH} and BBI_{RAE}, respectively.

To further demonstrate the accuracy of BBI_{ECG}, BBI_{RAE} and BBI_{RDH}, they are compared with the gold standard BBI_R. The corresponding RMSDs are calculated and denoted as $RMSD_{ECG}$, $RMSD_{RAE}$ and $RMSD_{RDH}$, respectively, with the results shown in Table 4.6.

The BBI_{ECG} is first compared with the BBI_R to demonstrate the accuracy of BBI_{ECG} in representing the gold standard BBI_R. A large variation of the $RMSD_{ECG}$ is observed for different subjects in Table 4.6. The $RMSD_{ECG}$ for 5 subjects are within 20 ms, but are over 50 ms for other 11 subjects. The average $RMSD_{ECG}$ for all the subjects is 42.0 ms, which is about 5 ms larger than the results of SCG stated in [55]. The relatively large deviation is due to the additional interference in the RAW, which results in an inaccurate annotation of AO and thus introduces difference between the AO-AO and the R-R intervals.

Table 4.6: The RMSDs of BBI_{ECG}, BBI_{RAE} and BBI_{RDH} from BBI_R (Unit: ms).

Subject No.	$RMSD_{ECG}$	$RMSD_{RAE}$	$RMSD_{RDH}$
F01	14.94	33.23	16.69
F02	54.22	86.47	57.35
F03	11.10	52.31	36.58
F04	44.29	59.30	55.27
F05	45.99	72.30	48.35
F06	46.03	83.99	51.47
F07	48.31	88.78	60.09
F08	53.78	59.22	56.12
F09	10.04	48.98	12.33
F10	41.89	64.76	63.42
M01	58.73	135.09	85.54
M02	22.96	67.84	33.64
M03	66.04	114.13	100.01
M04	58.00	77.77	70.61
M05	30.49	44.35	42.42
M06	18.19	39.34	30.08
M07	71.65	114.40	93.50
M08	37.70	50.72	41.29
M09	67.60	72.46	71.87
M10	52.99	65.25	64.45
M11	65.54	89.33	69.25
M12	3.81	12.89	3.81

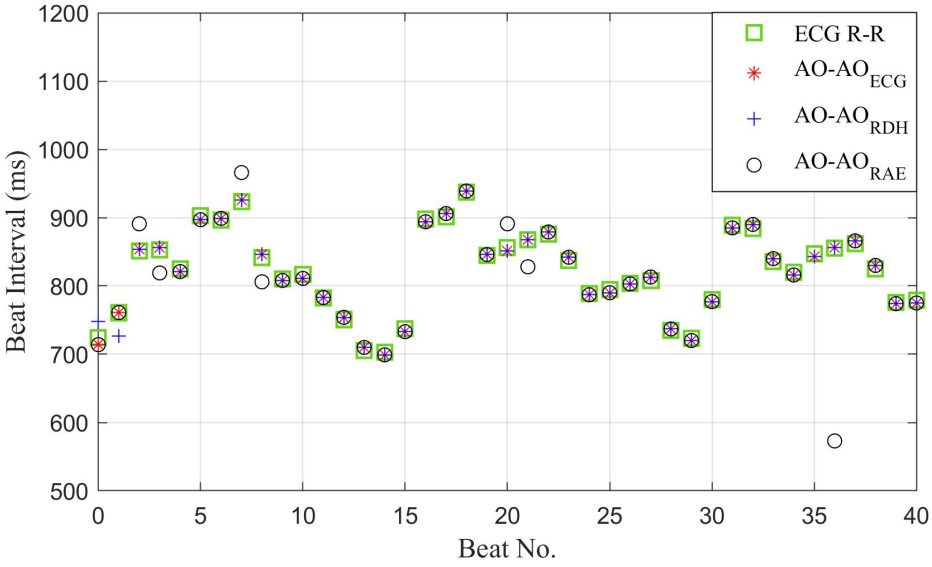

Figure 4.7: Beat-to-beat intervals calculated from AO for one subject.

The averages of $RMSD_{RAE}$ and $RMSD_{RDH}$ are 69.68 ms and 52.92 ms, respectively. Compared with $RMSD_{RAE}$, the $RMSD_{RDH}$ exhibits lower deviations for all the subjects. This indicates that the deviations of BBI_{RDH} from BBI_R are less than that of BBI_{RAE}, and BBI_{RDH} could achieve a better representation of BBI_R. The BBI_{RDH} could estimate the BBI_R and provide remote sensing of the BBI.

The deviation of BBI_{ECG}, BBI_{RAE} and BBI_{RDH} from BBI_R might be due to wrong annotation of AO for poor-quality RAW, especially when the RAW signal was interfered by small interference that makes it difficult to correctly locate AO. After marking the BBI_{ECG} that has deviations over 20 ms from the corresponding BBI_R, the locations of wrong annotations can be found. To evaluate the performance of BBI_{RDH} with less interference, BBI_{ECG}, BBI_{RAE} and BBI_{RDH} at these locations are removed, which leads to the improved $RMSD_{ECG}$, $RMSD_{RAE}$ and $RMSD_{RDH}$ as shown in Table 4.7.

After removing the large deviations, $RMSD_{ECG}$ are decreased to below 10 ms for all the subjects, and the average is 3.82 ms. Compared with the corresponding RMSDs in Table 4.6, $RMSD_{RAE}$ and $RMSD_{RDH}$ in Table 4.7 are also decreased. The averages of $RMSD_{RAE}$ and $RMSD_{RDH}$ are 43.92 ms and 20.12 ms, respectively, which implies a much

Table 4.7: The RMSDs of BBI_{ECG}, BBI_{RAE} and BBI_{RDH} from BBI_R after removing large deviations (Unit: ms).

Subject No.	$RMSD_{ECG}$	$RMSD_{RAE}$	$RMSD_{RDH}$
F01	2.64	31.85	8.64
F02	4.12	33.54	32.12
F03	2.12	35.47	22.68
F04	2.40	25.88	20.99
F05	3.23	39.14	3.27
F06	4.01	52.23	24.54
F07	3.67	74.30	18.65
F08	1.95	27.93	20.31
F09	3.45	24.36	10.47
F10	2.72	63.66	8.25
M01	4.30	69.17	26.50
M02	2.66	38.85	2.69
M03	9.95	51.72	38.15
M04	4.62	55.11	27.71
M05	3.21	32.74	19.95
M06	3.06	27.96	17.88
M07	5.53	91.44	42.97
M08	2.51	39.66	13.52
M09	4.00	35.26	34.39
M10	4.15	55.20	34.43
M11	6.02	42.88	10.68
M12	3.81	12.03	3.81

better performance for a high quality RAW signal.

4.3 Conclusion

In this chapter, an approach for detecting the AO from RAW without the concurrent ECG is presented to enable fully non-contact detection and analysis of SCG. The approach is based on a RDH signal that is derived from the radar displacement signal. The peaks of the RDH signals are used as reference points to locate the systolic profiles of RAW with a fixed time window. Then the peaks of the envelopes of the located systolic profiles are used as reference points for searching the AO_{RDH}. The results show that the AO_{RDH} have detection ratios over 75% for 20 out of 22 subjects, achieving a high estimation of AO points. The $LVET_{RDH}$ obtained from the ensemble averaged RAW is within 2 ms of the $LVET_{ECG}$. Additional analysis of the BBI reveals that the RDH-based approach could provide a non-contact detection of the BBI with an average RMSD of 52.92 ms, and the RMSD could be reduced to 20.01 ms after removing the large deviations or the heartbeats with relatively high interferences.

CHAPTER 5
THE REMOVAL OF CLUTTER EFFECT

In the previous chapters, the noise suppression improves the signal quality of the radar signals, and the SCG feature such as the fiducial points has been derived from the RAW without concurrent ECG. This provides great convenience for the remote sensing and analysis of the SCG signal. However, the background clutters still affect the signal quality. They are the microwave signals reflected from the backgrounds, containing no effective information. To better represent the SCG signal with the radar signals, this chapter focuses on the analysis of clutter effect on the signal quality and the clutter removal strategies.

The rest of the chapter is organized as follows. Section 5.1 analyzes the clutter effect in the microwave Doppler radar system. Then the FMCW radar system is analyzed and set up for the removal of clutters in section 5.2. Section 5.3 concludes the chapter.

5.1 Clutter Effect in Microwave Doppler Radar

5.1.1 Theoretical Analysis of Clutter Effect

Clutters are stationary background reflection of the microwave Doppler radar system, which carries no effective cardiac information, and they generate DC offset after being mixed with local oscillator signal (the transmitted carrier). Assuming the amplitude ratio between the clutter and the microwave signal carrier is r, the wave received by the radar includes the clutters and the effective microwave signal carrier,

$$m_r(t) = sin(\omega t + \phi_v(t)) + rsin(\omega t + \phi_c) \tag{5.1}$$

where ω is the angular frequency of the microwave carriers, and $\phi_v(t)$ and ϕ_c are the phases introduced by the chest wall vibration and the clutters, respectively.

After being mixed with the local oscillator, if neglecting the residual phase noise, the baseband signal can be expressed as equation (5.2).

$$B_{sig}(t) = sin[\phi_v(t)] + rsin(\phi_c) \tag{5.2}$$

where $\phi_v(t) = 4\pi[d_0 + x(t)]/\lambda_c$ according to the equation (2.11), and ϕ_c is a constant phase introduced by the clutters.

Further analysis of (5.2) shows that if $r \ll 1$, the clutter is very small. Then equation (5.2) approximately equals to $sin(\phi_v(t))$, which can be expressed as $\phi_v(t)$ based on the phase demodulation. This indicates that very low clutter has limited effects on the vital sign signal. However, if $r \gg 1$, the clutter dominates the received wave. Then equation (5.2) can be approximated by $rsin(\phi_c)$, and the term representing the vital sign signal $\phi_v(t)$ is lost, which demonstrates that high clutters can severely degrade the vital sign signal in the radar system.

For a relatively moderate clutter level, the clutters have effect on the vital sign signal. To further analyze the effect, equation (5.2) is represented as

$$\begin{aligned} B_{sig}(t) = (1+r)sin[\frac{\phi_v(t)+\phi_c}{2}]cos[\frac{\phi_v(t)-\phi_c}{2}] \\ + (1-r)cos[\frac{\phi_v(t)+\phi_c}{2}]sin[\frac{\phi_v(t)-\phi_c}{2}] \end{aligned} \tag{5.3}$$

where $\phi_v(t) = \phi_x(t) + \phi_{d0}$. $\phi_x(t) = 4\pi x(t)/\lambda_c$ and $\phi_{d0} = 4\pi d_0/\lambda_c$ are defined in equation (2.6). Since $\phi_x(t)$ is a small angle, equation (5.3) can be approximated to

$$B_{sig}(t) \approx \phi_x(t)cos\phi_{d0} + [\frac{\phi_x(t)}{2}]^2[-sin\phi_{d0} + rsin\phi_c] + (sin\phi_{d0} + rsin\phi_c) \tag{5.4}$$

The proof of equation (5.4) is given in the Appendix B.1. This approximation indicates that, depending on the value of ϕ_c, the clutter could influence the vital sign signal $\phi_x(t)$,

especially the high order harmonics of $\phi_x(t)$.

Moreover, the arctangent demodulation approach has often been adopted to eliminate the harmonics effects on the radar signal [18], which can effectively extract the vital sign signals without introducing additional respiration and heartbeat harmonics by using I/Q demodulation. Assuming the baseband signals in the I and Q channels are $cos[\phi_x(t)+\phi_{d0}]$ and $sin[\phi_x(t)+\phi_{d0}]$ respectively, the baseband signal $B'_{sig}(t)$ extracted from the arctangent demodulation is the vital sign signal $\phi_x(t)$, as shown below.

$$\begin{aligned} B'_{sig}(t) &= arctan\{\frac{sin[\phi_x(t)+\phi_{d0}]}{cos[\phi_x(t)+\phi_{d0}]}\} \\ &= \phi_x(t)+\phi_{d0} \end{aligned} \tag{5.5}$$

where, $\phi_x(t)$ can be extracted by simply removing the constant component ϕ_{d0}.

However, if the I and Q channels have clutters, the arctangent demodulation can no longer extract the accurate vital sign signal since

$$B'_{sig}(t) = arctan\{\frac{sin[\phi_x(t)+\phi_{d0}]+DC_{QC}}{cos[\phi_x(t)+\phi_{d0}]+DC_{IC}}\} \tag{5.6}$$

where, DC_{QC} and DC_{IC} are introduced by the clutters of the Q and I channels. Due to the phase ϕ_{d0} introduced by the average distance between the antenna and the subject, $sin[\phi_x(t)+\phi_{d0}]$ and $cos[\phi_x(t)+\phi_{d0}]$ in the I and Q channels usually contain DC terms. The proof is given in Appendix B.2. So, it is difficult to simply use a filter to eliminate the clutter DC component in both I and Q channels before the arctangent demodulation. In addition, since the vital sign signals have very low frequency, for example, the respiration locates at 0.2-0.5 Hz, the small frequency difference between the signal and clutter raises additional challenges for filter design. Therefore, it is critical to develop an effective clutter removal method to improve the radar vital sign signal quality and capture the subtle features reflecting real cardiac activities.

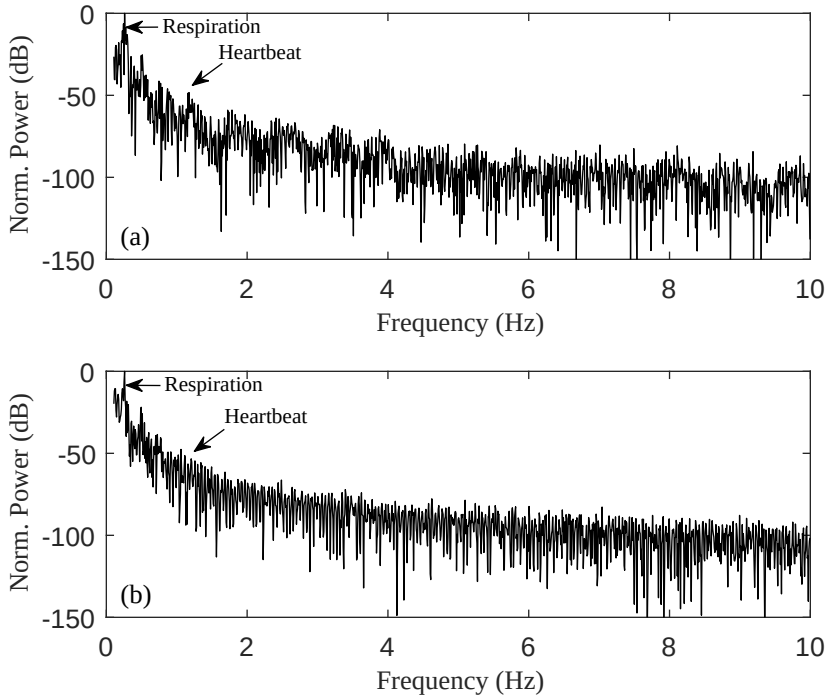

Figure 5.1: Spectra of radar signals for subject 1 with (a) low clutter level and (b) high clutter level

5.1.2 Experimental Setup

The antenna of the microwave Doppler radar system in [59] is 50 centimeters away from the chest wall, facing the dorso-ventral direction of the subject, and the transmission power is approximately 6 dBm. Six healthy young adults (age 26-29) participated in the studies (approved by Georgia Tech IRB). During the testing, each subject first remained still in the chair for 30 seconds, then performed an isometric hand grip exercise for 60 seconds, and then, after releasing the hand grip, maintained a resting state for 30 seconds. During the testing, the subjects remained quiet and avoided body movements to the extent possible. To acquire SCG and radar signals simultaneously, the radar system was synchronized with a high resolution accelerometer (356A32, PCB Piezotronics, Depew, NY, USA) attached at the sternum of the subjects. Electrocardiogram (ECG) signals were also measured as a reference.

Restricted by the equipment in our lab, the power level of background reflection was not measured. We only qualitatively evaluate the effect of clutter on the STI feature extraction under the physiological perturbation by creating high and low clutter levels in the experiments. The high and low clutter levels are achieved by adjusting the distance to the background walls. A short distance to the walls can result in a strong reflection back to the receive antenna, raising the power level of clutter.

5.1.3 Experimental Evaluation of Clutter Effect

The spectra of radar signals for subject 1 collected under high and low clutter levels are shown in Fig. 5.1. The results show that, under a high clutter level, the magnitudes of respiration and heartbeat signals are weakened, especially the frequency component corresponding to heartbeat, which is barely visible. Additionally, there are less high frequency components in Fig. 5.1 (b) comparing with Fig. 5.1 (a). These results indicate that the high clutter level can significantly deteriorate the quality of the radar signal, which is used to reflect the vital sign information.

The radar detected signals are segmented to single heartbeat cycles referring to the ECG signal, and the beat cycles are averaged to obtain the waveforms shown in Fig. 5.2. Baseline, test and recovery represent the initial 30-second rest state, 60-second hand grip and 30-second rest state after hand grip, respectively. As subjects 1, 3, 5 and 6 have similar results while subjects 2 and 4 represent a different outcome, only measurements of subjects 1 and 2 are shown in Fig. 5.2.

As shown in Fig. 5.2, the waveform collected by the contact accelerometer has a better signal quality than that of the radar signal. This may be due to various sources of interference corrupting the radar signals, such as minor body movements, and phase demodulation induced respiration harmonics and signal distortion.

With the high clutter level, the waveforms of both subject 1 and 2, as shown in Fig. 5.2(c), are significantly different from the accelerometer waveform, exhibiting no effective

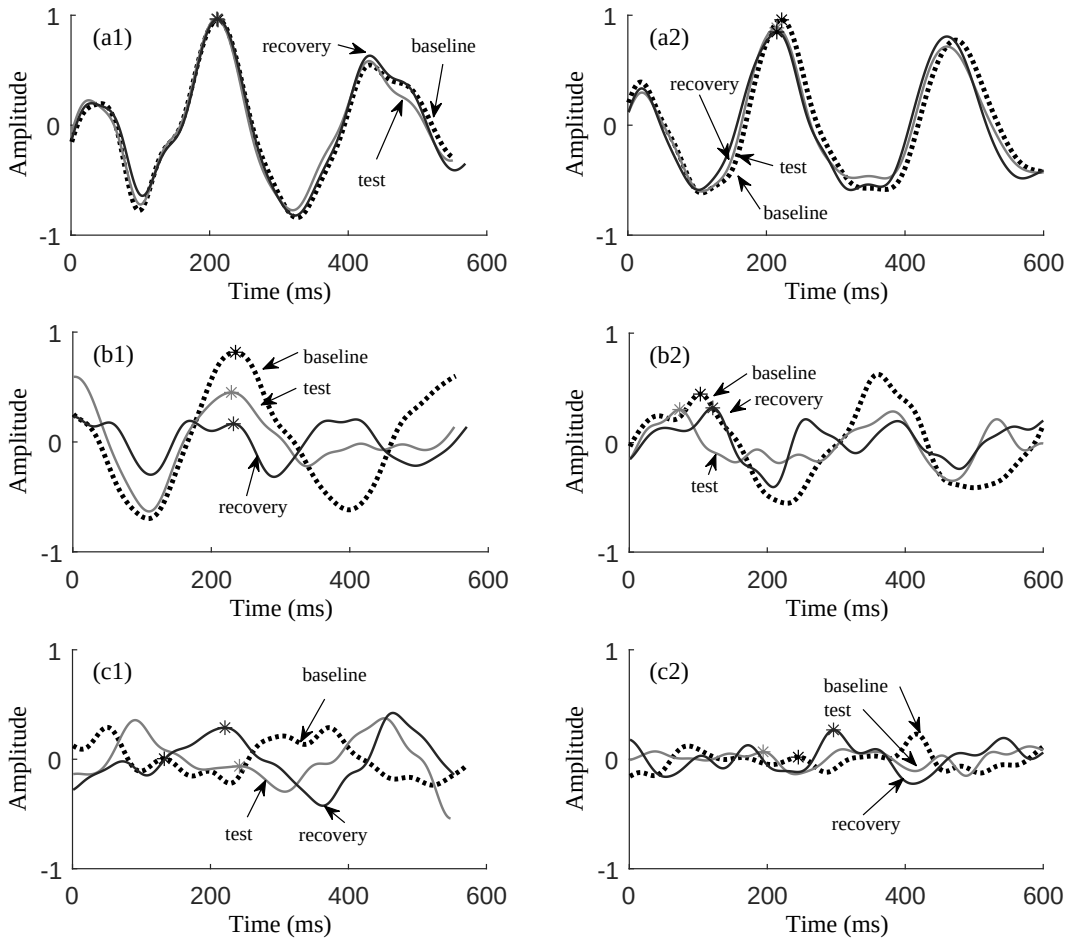

Figure 5.2: Waveforms of subject 1 (left) and subject 2 (right) with the handgrip challenge for (a) contact accelerometer (b) noncontact radar with low clutter level (c) noncontact radar with high clutter level

information. Under the low clutter level, the deviation directions of peak point under and after hand grip are the same as that detected by the accelerometer for subject 1, but they are not correct for subject 2. This may because that clutter or other interference factors has more significant influence on the waveform of subject 2. Nevertheless, the waveform of subject 2 at the low clutter level still has a morphology more in line with expectations than the waveform at the high clutter level.

Thus, a high clutter level can completely deteriorate the SCG waveforms collected by the noncontact radar system. In addition, even a low clutter level may reduce the similarity in waveform shapes between the radar signals and accelerometer signal, which may further

lead to incorrect detection of the deviation direction of STIs using the noncontact system. Therefore, it is important to design a clutter removal strategy to increase the measurement accuracy of the noncontact radar waveforms so that the cardiovascular behavior can be effectively captured.

5.2 The FMCW Radar System for Clutter Removal

5.2.1 Theoretical Analysis

In our preliminary analysis and experimental test in section 5.1, clutters introduce severe interference to the radar signals, causing the degradation of signal, such as the loss of morphology and the systolic features. A scheme is necessary to remove the effect of clutters. FMCW radar has been widely used in the detection of the target range and the relative velocity. The good noise performance and the range discrimination capability make it a promising candidate for removing clutters in a non-contact cardiac signal detection system.

Generally, the FMCW radar generates a wave with continuous phase, and the frequency linearly varying with time, which can have frequency modulation pattern of ramp (sawtooth) or triangular. Thus, with a frequency modulation pattern of ramp, the frequency of the FMCW radar within a period can be represented as

$$f(t) = f_0 + \gamma * (t - kT), kT \leq t \leq (k+1)T \tag{5.7}$$

where, f_0 is the initial frequency of the FMCW signal, γ represents the slope of the frequency ramp, k is an integer, and T stands for the period of the FMCW signal. As shown in equation (5.7), the minimum and maximum frequencies are f_0 and $f_0 + \gamma T$, respectively. Thus, the bandwidth of the FMCW signal can be expressed as

$$B = \gamma T \tag{5.8}$$

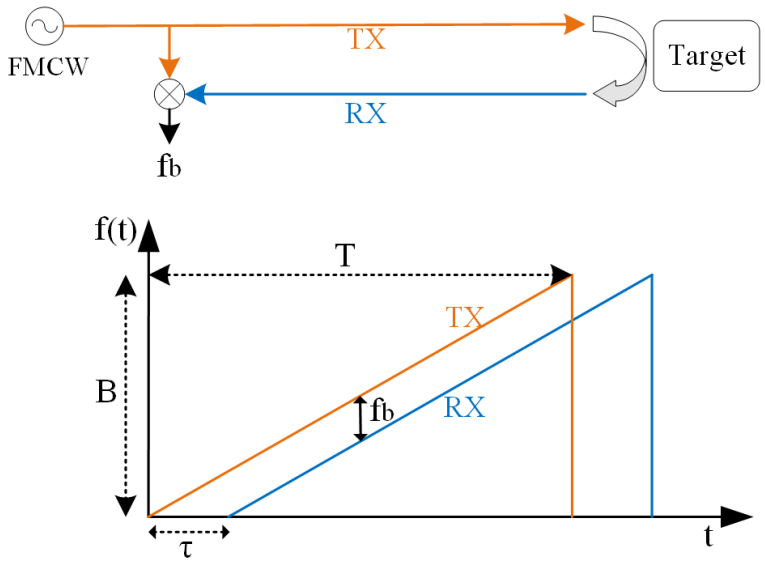

Figure 5.3: The detection of the range through the FMCW radar system.

Correspondingly, the slope of the FMCW can be calculated through $\gamma = BW/T$.

Integrating the frequency $f(t)$ over time can reveal the phase of a FMCW signal within a period $[kT, (k+1)T]$.

$$\phi(t) = 2\pi \int_{kT}^{t} f(t)dt \tag{5.9}$$

$$= 2\pi(f_0 t + \frac{1}{2}\gamma t^2)|_{kT}^{t} \tag{5.10}$$

$$= 2\pi f_0(t - kT) + \pi\gamma(t - kT)^2 \tag{5.11}$$

where, $kT \leq t \leq (k+1)T$.

The FMCW wave with phase $\phi(t)$ is transmitted to the target for the range and relative velocity measurement, and then received by the FMCW radar system. Assuming the distance between the radar and the target to be R_0, the round trip delay should be $\tau = 2R_0/c$, where c is the speed of the light in the vacuum. The mixing of the received and transmitted FMCW signals generates a beat signal of frequency f_b. As shown in Fig. 5.3, according to

the triangle similarity postulates and theorems, there exists

$$\frac{\tau}{T} = \frac{f_b}{B} \Rightarrow R_0 = \frac{cT}{2B} f_b = \frac{c}{2\gamma} f_b \tag{5.12}$$

The measurement of the frequency of the beat signal can detect the distance R_0 between the radar and the target, as c, T and B are constant during the detection.

In equation (5.12), the accuracy of the range R_0 depends on the measurement of the beat frequency f_b. Thus, the range resolution relies on the frequency resolution of f_b, and can be written as

$$\delta R = \frac{cT}{2B} f_{min} \tag{5.13}$$

where, δR_0 is the range resolution of FMCW radar, and f_{min} represents the frequency resolution.

The frequency resolution is given by $f_{min} = f_s/N$, where f_s is the sampling frequency of the beat signal and N is the number of samples [60]. The resolution f_{min} of the FMCW radar can be expressed as

$$f_{min} = \frac{f_s}{N} = \frac{1}{NT_s} = \frac{1}{T} \tag{5.14}$$

where, the sampling time $T_s = 1/f_s$, and $T = NT_s$. $f_{min} = f_s/N$ shows that a high frequency resolution can be achieved through increasing the number of samples N. However, this cannot be achieved for a FMCW radar, as f_{min} is a constant $1/T$.

Combine the equations (5.13) and (5.14), and the range resolution δR of a FMCW radar can be calculated.

$$\delta R = \frac{c}{2B} \tag{5.15}$$

The range resolution only depends on the bandwidth of the FMCW radar, which indicates that a large bandwidth can contribute to a high range resolution.

The FMCW radar can identify the distance between the radar and the target with a range resolution of δR, and thus any distance in the range $[R_1 - \delta R, R_1 + \delta R]$ is detected as R_1.

If the vital sign signal exists in the range bin $[R_1 - \delta R, R_1 + \delta R]$, the clutters reflected from the distances outside this range can be isolated, which achieves the removal of the clutters. Thus, the FMCW radar can be applied to reduce the clutter effect in the vital sign detection, and the acquisition of the cardiac signal, such as the SCG.

However, if there exist clutters and cardiac signals in the range $[R_1 - \delta R, R_1 + \delta R]$, the clutters cannot be isolated from the cardiac signals as they are in the same range bin. Thus, the amount of clutters on the cardiac signal can be controlled through adjusting the range resolution, which is determined by the bandwidth of the FMCW radar.

5.2.2 Data Acquisition

The principle of FMCW radar in the vital sign signal detection is similar to that discussed in section 2.1.1, except that the frequency is $f(t)$ in equation (5.7) instead of the f_c in section 2.1.1. Assuming the average distance between the subject and the radar contributes a beat signal with frequency f_b, the vital sign signal can be extracted from the phase of the beat signal [61],

$$B(t) = \sigma exp\{j[\frac{4\pi\gamma R(\tau_s)t}{c} + \frac{4\pi f_0 R(\tau_s)}{c} + \Delta\phi]\} \tag{5.16}$$

where, σ is the amplitude of the beat signal, $\Delta\phi$ represents the residual phase, τ_s is the slow-time, and the range $R(\tau_s)$ can be assumed to be constant during each period of the transmitted FMCW ramp. Here, the slow-time phase of the beat signal represents the vital sign, which means the phase of a beat signal corresponding to a ramp can represent a point of the vital sign signal, as shown in Fig. 5.4. A high rate of the frequency ramp can contribute to a high sampling rate of the vital sign signal.

Based on the above analysis, a FMCW radar system (AWR1642BOOST, Texas Instruments, Dallas, TX, USA) was set up to detect the vital sign signals, especially the cardiac signal RAW. The FMCW radar works at 76 GHz to 81 GHz with 4 GHz available bandwidth, and the transmitter power is 12.5 dBm. The on-board antenna has a gain of 10 dB. The radar system was positioned 50 cm from the subject, with the antenna facing the hu-

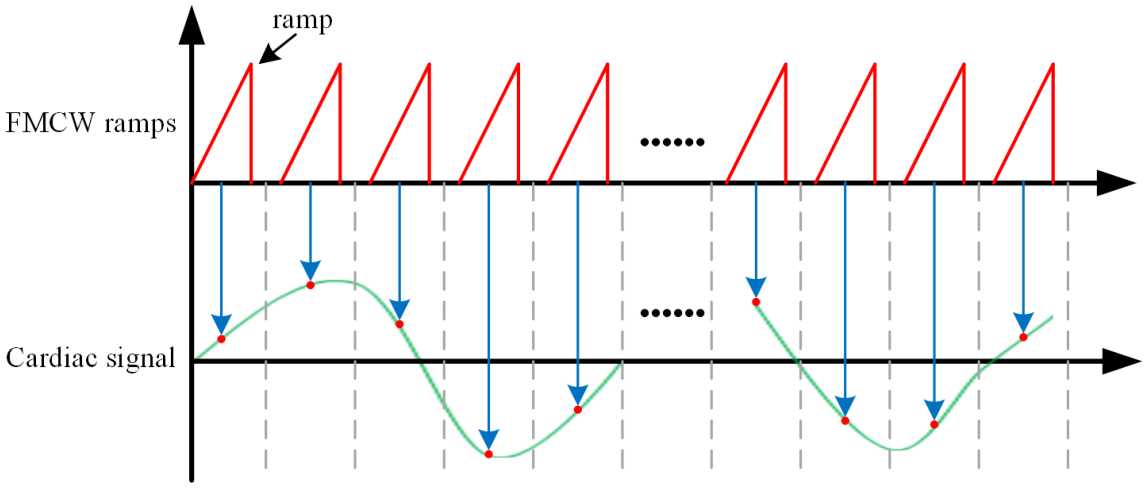

Figure 5.4: The signal acquisition with a FMCW radar.

man subject, as illustrated in Fig. 5.5. A DCA1000EVM data capture card was configured to sample the beat signal of the FMCW radar, with a sampling rate up to 600 Mbps.

The radar system was configured to work at 4 GHz, 2 GHz, 1 GHz, 0.5 GHz, and 0.25 GHz, and to control the amount of clutters in the FMCW radar detection, which corresponds to a range resolution of 3.75 cm, 7.5 cm, 15 cm, 30 cm, and 60 cm, respectively. With a large range resolution number, a high amount of clutters was introduced. For example, the FMCW radar with a range resolution of 60 cm (0.25 GHz bandwidth), suffers more clutters than the radar with a range resolution of 3.75 cm (4 GHz bandwidth).

One healthy subject (Gender: male; Age: 30 years; Height: 186 cm; and Weight: 80 kg) volunteered to participate in the experiment. The volunteer was informed of the experimental procedures and signed the consent form (approved by the Georgia Tech Institutional Review Board) before the experiment. The five bandwidths were applied for one data acquisition, and the subject sat on a chair for 40 seconds at each bandwidth. Then the recordings were repeated for six times. During the data recording, the subject was asked to keep still and reduce activities such as gestures and intentional body movements.

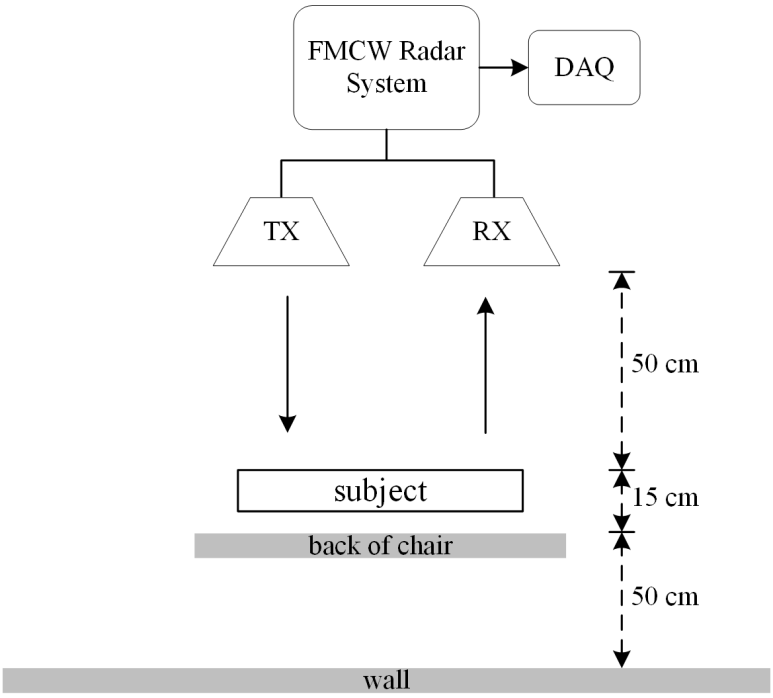

Figure 5.5: Block diagram of the FMCW radar detection system. TX, transmission antenna; RX, receiver antenna; DAQ, data acquisition unit.

5.2.3 Experimental Evaluation

The beat signal of the FMCW radar system was recorded, and the slow-time vital sign signal was then extracted from its phase. Finite impulse response (FIR) filter (Kaiser window) with a passband of 0.2-40 Hz was applied to the vital sign signal to remove the out-of-band noise and interference. The time domain signal and its corresponding spectrum with the 4-GHz FMCW bandwidth are shown in Fig. 5.6.

In Fig. 5.6, the detected signals exhibit pretty good respiration signal at the FMCW bandwidth 4 GHz, which illustrates that the introduced clutters have limited influence on the detection of the respiration signal. The spectrum indicates a clear heartbeat component, which can be easily identified in the frequency range $[0.8, 2.5]$ Hz.

Additional results were obtained for the FMCW bandwidths of 2 GHz, 1 GHz, 0.5 GHz, and 0.25 GHz, and they are shown in Figs. 5.7 and 5.8. The respiration signals in Fig. 5.7 still have very good signal quality. However, the respiration signals are severely deteriorat-

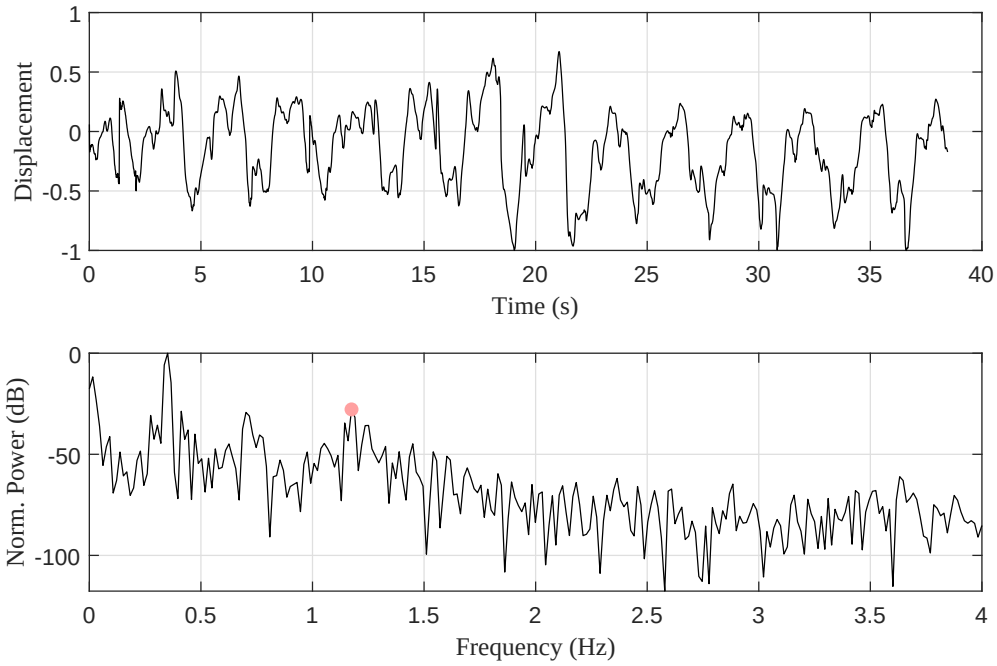

Figure 5.6: The vital sign signal in the time domain and the frequency domain with FMCW bandwidth 4 GHz.

ed in Fig. 5.8. At FMCW bandwidths 0.5 GHz and 0.25 GHz, the range resolutions are 30 cm and 60 cm, respectively. High level clutters were introduced by the back of the chair and the wall based on the system setup in Fig. 5.5.

Further analysis of their spectra shows that the heartbeat component is gradually degraded with the decrease of the FMCW bandwidth or the increase of the clutters. At the bandwidths 0.5 GHz and 0.25 GHz, the frequency component cannot be correctly identified, especially at 0.25 GHz.

To demonstrate the performance of the RAW and the similarity to dorso-ventral SCG, a FIR bandpass filter (Kaiser window) with a passband of 18-35 Hz was applied. The RAW waveforms at different FMCW bandwidths are shown in Figs. 5.9 and 5.10.

The RAW waveform in Fig. 5.9 can clearly demonstrate the cardiac cycles, and the systolic and diastolic profiles, which can be further used to identify the AO and AC, thus the systolic time intervals. At such a FMCW bandwidth of 4 GHz, the range resolution is

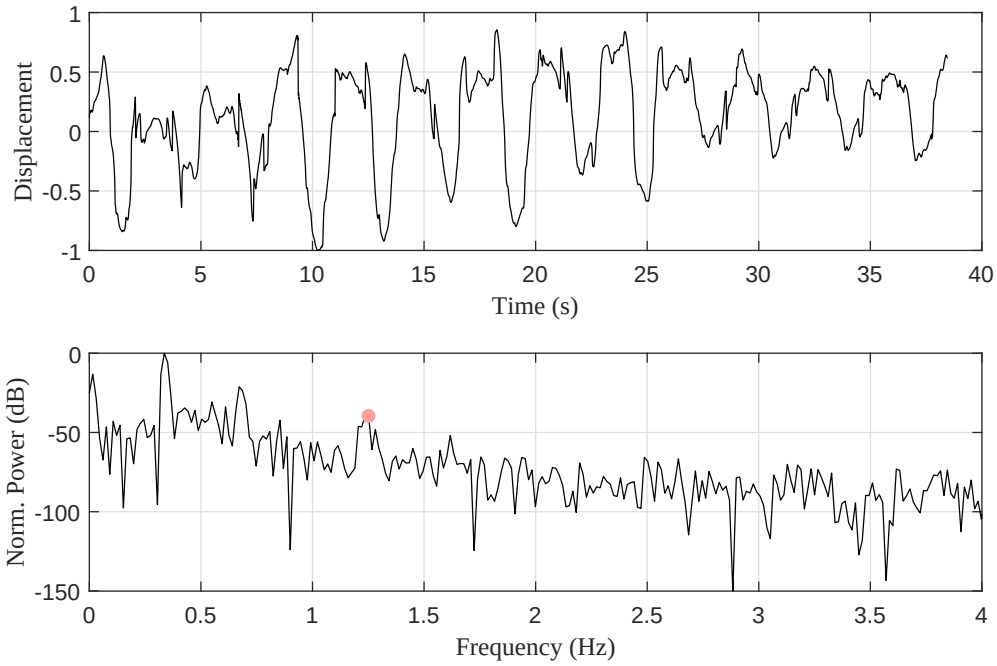

(a) FMCW bandwidth 2 GHz

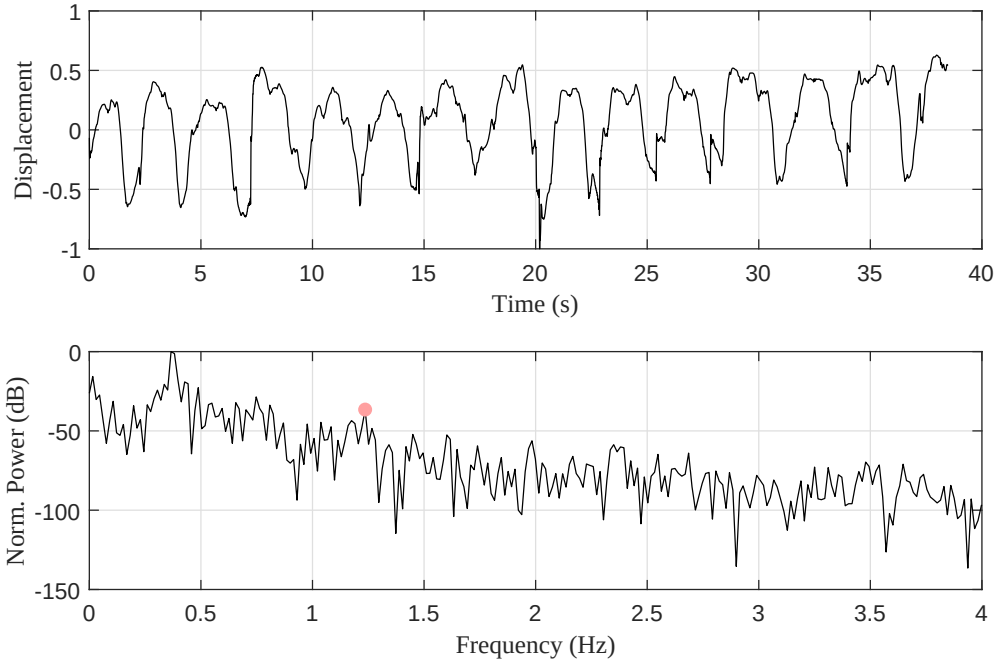

(b) FMCW bandwidth 1 GHz

Figure 5.7: The vital sign signal in the time domain and the frequency domain with FMCW bandwidths 2 GHz and 1 GHz.

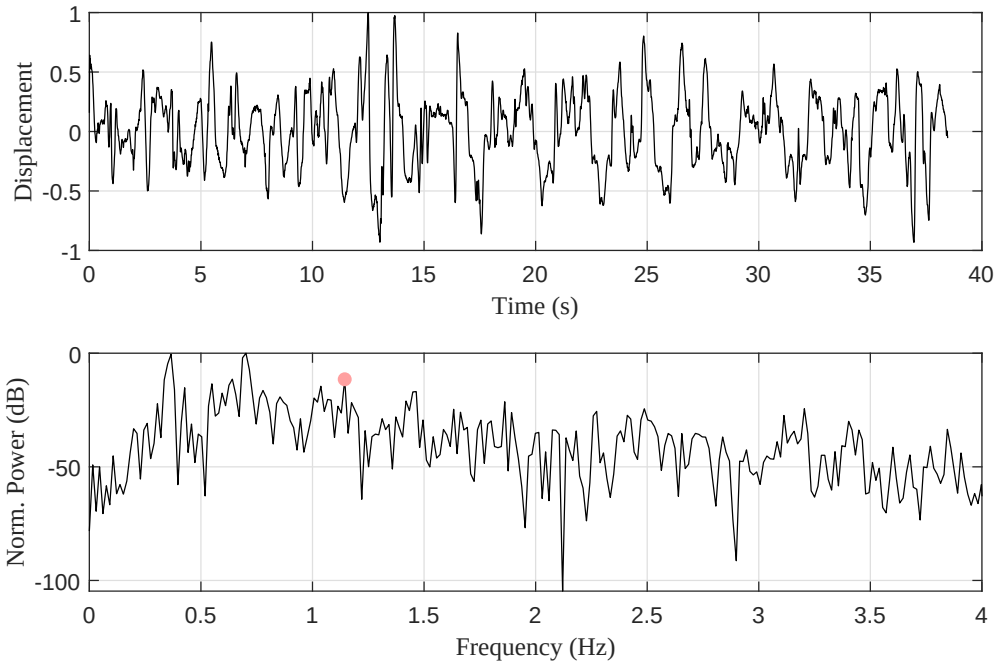

(a) FMCW bandwidth 0.5 GHz

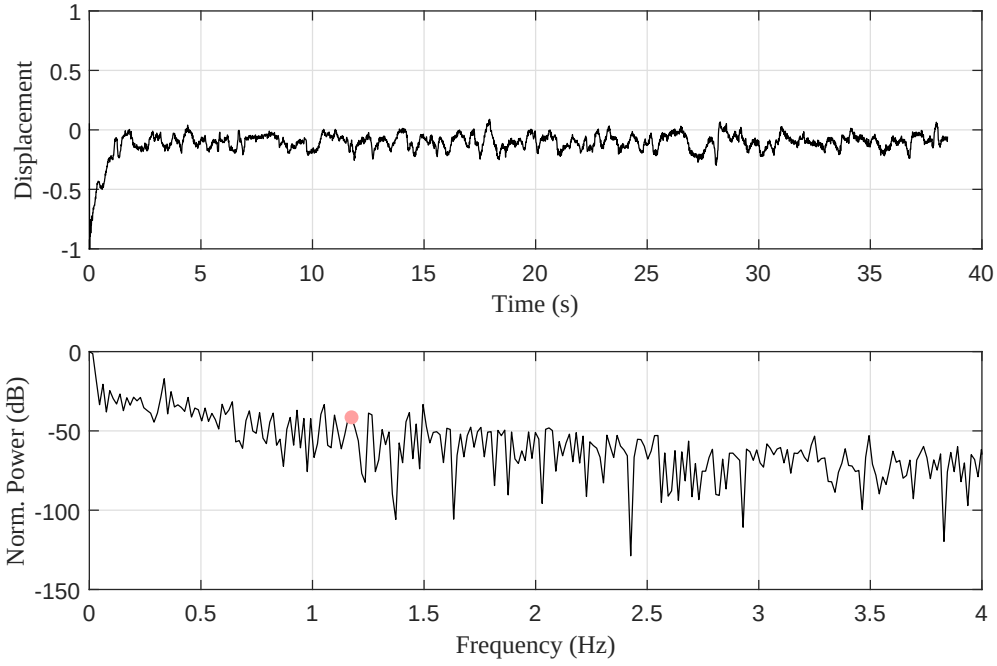

(b) FMCW bandwidth 0.25 GHz

Figure 5.8: The vital sign signal in the time domain and the frequency domain with FMCW bandwidths 0.5 GHz and 0.25 GHz.

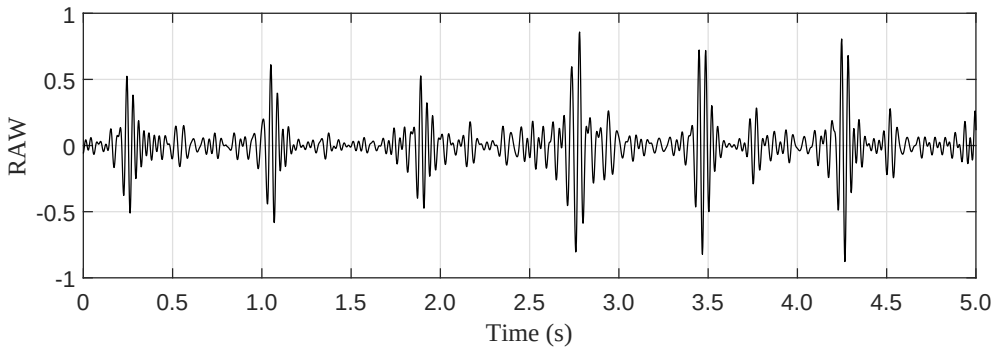

Figure 5.9: The RAW waveform using the FMCW bandwidth 4 GHz.

only 3.75 cm, and the clutters outside of the range bin $[R-3.75, R+3.75]$ cm are isolated, where R is the average distance between the radar and the subject.

At FMCW bandwidths of 2 GHz and 1 GHz, the RAW can still exhibit the cardiac cycles and demonstrate the dorso-ventral SCG features. However, the signal quality has been degraded, and the systolic or diastolic profiles are not as good as those in Fig. 5.9. When the FMCW bandwidth decreases to 0.5 GHz and 0.25 GHz, the RAW waveforms are severely deteriorated, and no effective cardiac information can be extracted from the RAW waveform.

The above analysis shows that there exists a high level clutter in the environment that can severely deteriorate the cardiac signal quality, as shown by the cardiac signals collected by the FMCW radar with the bandwidth of 0.25 GHz. In such an environment with high clutter level, the FMCW radar with a proper bandwidth can isolate the clutters with an excellent performance, and remove clutters from the cardiac signals. As the capability of the clutter isolation relies on the range resolution or the bandwidth of the FMCW radar, a wide band FMCW radar is desired to enhance the clutter removal performance.

5.3 Conclusion

In this chapter, the clutter effect on the cardiac signal in the microwave Doppler radar detection is discussed, and the FMCW radar is presented for the clutter removal. Theoretical

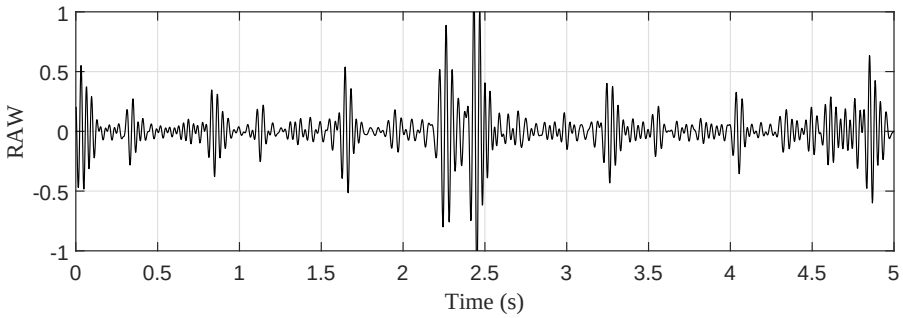

(a) FMCW bandwidth 2 GHz

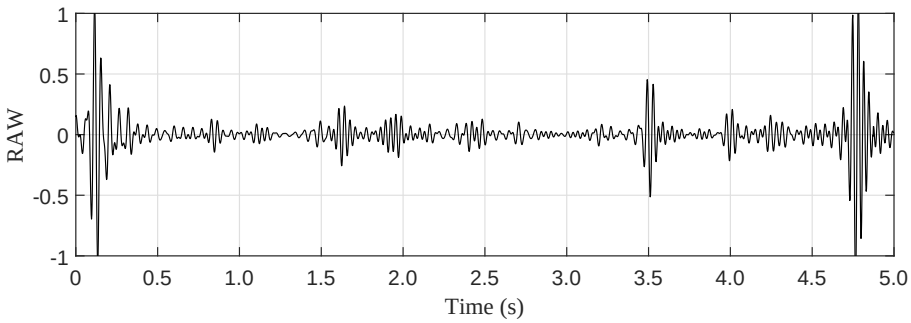

(b) FMCW bandwidth 1 GHz

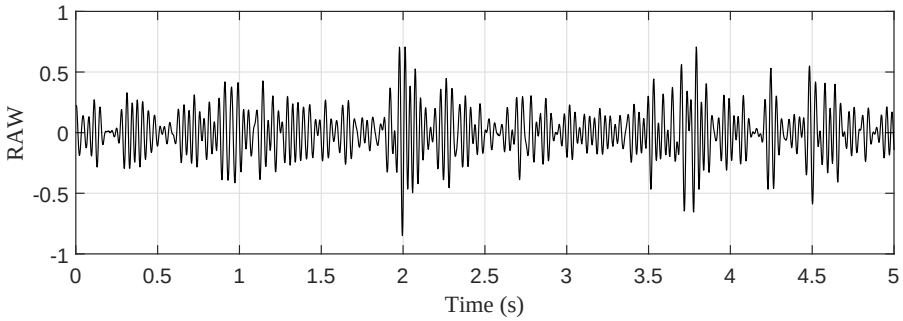

(c) FMCW bandwidth 0.5 GHz

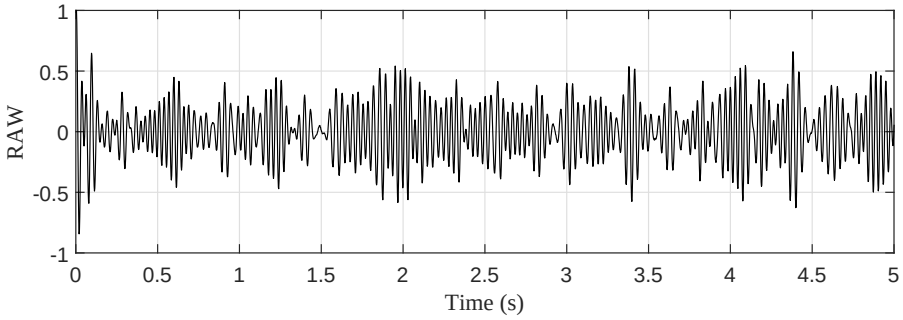

(d) FMCW bandwidth 0.25 GHz

Figure 5.10: The RAW waveform using different FMCW bandwidths.

and experimental analysis reveals that the clutters bring significant influence to the cardiac signal quality, especially under high-level clutters. Due to the range-isolation capability, the FMCW radar is a promising technique to reduce the clutter effect. It can eliminate the clutters that are not at the same distance as the detected signal. A significant improvement of the spectrum and transient waveform demonstrates the effectiveness of the FMCW radar. However, it cannot remove the clutters reflected from the backgrounds that are at the same distance of the human subject. In addition, a FMCW radar of a wide frequency bandwidth is desired to achieve a better performance of the clutter removal.

CHAPTER 6
CONCLUSIONS AND FUTURE WORK

6.1 Conclusions

The thesis focuses on the remote sensing of the seismocardiogram (SCG) signal through a microwave Doppler radar system. Several circuit designs and radar signal processing techniques are developed to improve the accuracy and robustness of the radar signal, and derive the effective cardiac features from the radar signals.

For the hardware design of the radar system, a noise suppression scheme is proposed in Chapter 2 for the microwave Doppler radar system to improve the noise performance of the baseband radar signal, and thus the quality of the cardiac signal. Dual carriers and PLL are proposed to automatically reduce the residual phase noise and the path noise. One carrier is designed to detect and suppress the noises in the PLL, providing a clean transmission path for the other carrier. Then the vital sign signal contained in the phase of the second carrier can be obtained with low noise. The design can improve the SNR by about 12 dB at 10-Hz frequency offset, and increase the detection distance of the weak heartbeat signal.

For the radar signal processing, studies are conducted to explore the radar signal characteristics, and experimentally verifies the effective representation of the dorso-ventral SCG within the frequency band 18-35 Hz in Chapter 3. The cross correlation coefficients and the RMSDs are calculated to analyze the similarity of the morphology and the location of the fiducial points, respectively. Additionally, an experiment is designed to illustrate the accuracy of the radar acceleration waveform (RAW) in estimating the decrease of pre-ejection period (PEP) for the subjects subjected to physiological perturbations. The theoretical and experimental analysis reveals the high similarity of the RAW to the SCG, illustrating an effective SCG detection through the microwave Doppler radar.

In addition, a standalone method is developed to extract SCG features from RAW without relying on concurrent ECG in Chapter 4, and the complete non-contact detection and analysis of the SCG is achieved. A radar displacement signal of heartbeat (RDH) is derived from radar displacement signal, and the time windows are located using the RDH peaks. The systolic profiles and the AO points of the RAW are then located, and the detection ratios of AO are over 75% for 20 out of 22 subjects. The ensemble averaged RAWs and the beat to beat intervals (BBIs) are calculated. Additional analysis of the BBI reveals that the RDH-based approach could provide a non-contact detection of the BBI with an average RMSD of 52.92 ms, and the RMSD could be reduced to 20.01 ms after removing the large deviations or the heartbeats with relatively high interferences. The RDH-based approach can detect the AO with high accuracy, and promote the complete non-contact measurement of SCG using the radar system.

Additional hardware design of the radar system is explored for the clutter removal in Chapter 5. The clutter effect on the cardiac signal collected by the microwave Doppler radar is analyzed. The FMCW radar is investigated for the clutter removal. Due to the range-isolation capability, the FMCW radar can reduce the clutter effect and eliminate the clutters that are not at the same distance of the detected signal. A significant improvement of the clutter performance can be achieved through a large frequency bandwidth.

6.2 Future Work

The potential future work for the remote sensing of the SCG through the microwave Doppler radar system is discussed.

For the hardware design of the system, clutter removal strategy can be improved through implementing the FMCW radar system. The design of a wide frequency band FMCW radar can significantly improve its capability of isolating the clutters, and thus enhance the signal quality and the reliability of the radar detection of cardiac signals. Wide frequency band can be achieved with the advanced design of FMCW signal generator, which may require

wideband voltage controlled oscillator and the loop filter. This could cause an increased cost of the FMCW radar. The photonic generation of the FMCW signal should be a promising approach for a wide band FMCW signal. The extremely high frequency optical carrier brings great convenience to frequency modulate waves with wide band, and thus the optical system could generate frequency modulated microwave or millimeter wave signals of large bandwidth.

For the radar signal processing, antennas with better directivity can be applied to explore the effect of detection area on the cardiac signal. As the radar system can acquire the signals from the entire plane of the chest wall, the baseband radar signal may be able to reveal more cardiac activities than the SCG. Additional exploration of eliminating the random movement, such as the matching pursue and machine learning techniques can be conducted to increase the accuracy and robustness of the RAW. Moreover, developing machine learning techniques for analyzing the normal cardiac signals can help identify the normal cardiac signals from the interfered signals, and also give an estimation to the status of the human subject, such as the rest state and the exercise state.

Appendices

APPENDIX A

PROOF FOR CHAPTER 2

A.1 Effect of the Auxiliary Path

In order to analyze the effect of auxiliary path on the noise performance of the vital sign signal, we firstly assume the amplitude ratio between the auxiliary path and received signal is α. Thus, the IF port (point 4) of frequency down-converter in Fig. 2.4 has an output signal,

$$\begin{aligned} v_4 &= \underbrace{sin(\theta_a) + sin(\theta_b)}_{reflected} + \underbrace{\alpha sin(\vartheta_a) + \alpha sin(\vartheta_b)}_{auxiliary} \\ &= \underbrace{sin(\theta_a) + \alpha sin(\vartheta_a)}_{v_6(t)} + \underbrace{sin(\theta_b) + \alpha sin(\vartheta_b)}_{v_7(t)} \end{aligned} \tag{A.1}$$

where, $\theta_a = \omega_v t + (\omega_a + \omega_v)\tau + \phi_v + \varphi_n$, $\theta_b = (\omega_b - \omega_a + \omega_v)t + (\omega_b + \omega_v)\tau + (\phi_b - \phi_a + \phi_v + \varphi_n)$, $\vartheta_a = \omega_v t + (\omega_a + \omega_v)\hat{\tau} + \phi_v + \hat{\varphi_n}$ and $\vartheta_b = (\omega_b - \omega_a + \omega_v)t + (\omega_b + \omega_v)\hat{\tau} + (\phi_b - \phi_a + \phi_v + \hat{\varphi_n})$. Here, ϑ_a and ϑ_b are the phases of carrier a and carrier b in the auxiliary path. $\hat{\tau}$ and $\hat{\varphi_n}$ represent the delay and noise introduced by the auxiliary path, and they can be neglected as the auxiliary path is very short.

Through the mathematical transform, $v_6(t)$ can be rewritten as

$$v_6 = (1 + \alpha)sin(x_a)cos(y_a) + (1 - \alpha)cos(x_a)sin(y_a) \tag{A.2}$$

where, $x_a = (\theta_a + \vartheta_a)/2$, $y_a = (\theta_a - \vartheta_a)/2$.

In the short distance ($\alpha \ll 1$), $1 + \alpha \approx 1 - \alpha$. Thus, $v_6(t)$ will be $v_6 = sin(x_a + y_a) = sin(\theta_a)$, which implies the auxiliary path doesn't influence the vital sign detection. If the ratio α is increasing to 1, $v_6 = 2sin(x_a)cos(y_a)$. The cosine term is the slow amplitude

fluctuation, and amplitude noise of the new VCO can be neglected in the PLL. v_6 is locked to the reference signal v_5, so $\varphi_6 = x_a = 8(\omega_{ref}t + \phi_{ref})$, thus

$$v_7 = 2sin[8\phi_{ref} + \frac{\omega_b - \omega_a}{2}(\tau + \hat{\tau}) + \phi_b - \phi_a] \tag{A.3}$$

where $\hat{\tau}$ is the delay introduced by auxiliary path, and it's much smaller than τ. When the ratio is around 1, the effect of auxiliary path can be neglected. So the performance of vital sign is not degraded in the short distance.

As the detection distance extends, the effect of auxiliary path on vital sign will appear. In the long distance ($\alpha \gg 1$), $v_6 = \alpha sin(x_a - y_a) = sin(\vartheta_a)$, the loop is totally locked through the auxiliary path. The system can hardly detect the vital sign signal.

The lower the power of the auxiliary path, the better. But it should be enough to provide a -10 dBm of v_6, required by the datasheet of PFD used in our system. To achieve a -10 dBm of v_6, the auxiliary path should be -18 dBm which is the minimum power required to lock the loop when there is no RX received signal. The auxiliary path guarantees a stable detection when the amplified reflected signal is even lower than -18 dBm.

APPENDIX B

PROOF FOR CHAPTER 5

B.1 Proof of Equation 5.4

According to equation (5.3), the baseband vital sign signal can be further represented as

$$\begin{aligned} B_{sig}(t) = (1+r)sin[\frac{\phi_x(t)+\phi_c^+}{2}]cos[\frac{\phi_x(t)-\phi_c^-}{2}] \\ + (1-r)cos[\frac{\phi_x(t)+\phi_c^+}{2}]sin[\frac{\phi_x(t)-\phi_c^-}{2}] \end{aligned} \tag{B.1}$$

where, $\phi_c^+ = \phi_c + \phi_{d0}$ and $\phi_c^- = \phi_c - \phi_{d0}$. Expand the sine and cosine terms in equation (B.1), then

$$\begin{aligned} B_{sig}(t) = (1+r)[sin\frac{\phi_x(t)}{2}cos\frac{\phi_c^+}{2} + cos\frac{\phi_x(t)}{2}sin\frac{\phi_c^+}{2}][cos\frac{\phi_x(t)}{2}cos\frac{\phi_c^-}{2} + sin\frac{\phi_x(t)}{2}sin\frac{\phi_c^-}{2}] \\ + (1-r)[cos\frac{\phi_x(t)}{2}cos\frac{\phi_c^+}{2} - sin\frac{\phi_x(t)}{2}sin\frac{\phi_c^+}{2}][sin\frac{\phi_x(t)}{2}cos\frac{\phi_c^-}{2} - cos\frac{\phi_x(t)}{2}sin\frac{\phi_c^-}{2}] \end{aligned} \tag{B.2}$$

As $\phi_x(t)$ is a small angle, equation (B.2) can be approximated based on the small angle approximation.

$$\begin{aligned} B_{sig}(t) \approx (1+r)[\frac{\phi_x(t)}{2}cos\frac{\phi_c^+}{2} + sin\frac{\phi_c^+}{2}][cos\frac{\phi_c^-}{2} + \frac{\phi_x(t)}{2}sin\frac{\phi_c^-}{2}] \\ + (1-r)[cos\frac{\phi_c^+}{2} - \frac{\phi_x(t)}{2}sin\frac{\phi_c^+}{2}][\frac{\phi_x(t)}{2}cos\frac{\phi_c^-}{2} - sin\frac{\phi_c^-}{2}] \end{aligned} \tag{B.3}$$

Here, $cos[\phi_x(t)/2] \approx 1$. Equation (B.3) can be re-written as

$$\begin{aligned} B_{sig}(t) &\approx \phi_x(t)cos\frac{\phi_c^+ - \phi_c^-}{2} + (\frac{\phi_x(t)}{2})^2[sin\frac{\phi_c^- - \phi_c^+}{2} + rsin\frac{\phi_c^- + \phi_c^+}{2}] \\ &+ [sin\frac{\phi_c^+ - \phi_c^-}{2} + rsin\frac{\phi_c^+ + \phi_c^-}{2}] \\ &= \phi_x(t)cos\phi_{d0} + [\frac{\phi_x(t)}{2}]^2[-sin\phi_{d0} + rsin\phi_c] + (sin\phi_{d0} + rsin\phi_c) \end{aligned} \tag{B.4}$$

B.2 Proof of Equation 5.6

Assume equation (5.2) represents the Q channel signal, then the I and Q channel signals are shown as below.

$$I_B(t) = cos[\phi_x(t) + \phi_{d0}] + rcos\phi_c \tag{B.5}$$

$$Q_B(t) = sin[\phi_x(t) + \phi_{d0}] + rsin\phi_c \tag{B.6}$$

where, $\phi_x(t) = 4\pi x(t)/\lambda_c$ and $\phi_{d0} = 4\pi d_0/\lambda_c$ are defined in equation (2.6).

Define $DC_{QC} = rsin\phi_c$, and $DC_{IC} = rcos\phi_c$, which are constants corresponding to DC voltages at the output of the demodulator. $Q_B(t)$ is further represented as

$$\begin{aligned} Q_B(t) &= sin[\frac{4\pi x(t)}{\lambda_c} + \frac{4\pi d_0}{\lambda_c}] + DC_{QC} \\ &= sin\frac{4\pi x(t)}{\lambda_c} cos\frac{4\pi d_0}{\lambda_c} + cos\frac{4\pi x(t)}{\lambda_c} sin\frac{4\pi d_0}{\lambda_c} + + DC_{QC} \\ &\approx \frac{4\pi x(t)}{\lambda_c} cos\frac{4\pi d_0}{\lambda_c} + \{1 * sin\frac{4\pi d_0}{\lambda_c} + DC_{QC}\} \end{aligned} \tag{B.7}$$

In equation (B.7), $4\pi x(t)/\lambda_c$ is a small angle due to the slight vibration on the chest wall. After the small angle approximation, the first term represents the chest wall vibration or the vital sign signal with a ratio related to the averaged distance d_0, and the second term is a constant which is a DC voltage in the demodulator. This DC voltage contains the DC voltage resulting from the signal detection and the clutters. Thus, a simple high-pass filtering cannot remove the DC resulted from the clutters.

Similar result is obtained for the I channel signal $I_B(t)$. The DC voltage also comes from the signal detection and the clutters, which brings difficulty to remove the clutters through a simple filter.

$$I_B(t) \approx \frac{4\pi x(t)}{\lambda_c} * sin\frac{4\pi d_0}{\lambda_c} + \{1 * cos\frac{4\pi d_0}{\lambda_c} + DC_{IC}\} \tag{B.8}$$

APPENDIX C

EXPERIMENTAL EQUIPMENT

The experimental equipments for the research project include

1. Microwave signal generator, providing the stable and low-noise microwave signals at multiple frequencies
    - PNA Network Analyzer: Agilent N5222A
    - Swept Signal Generator: HP 83622B
2. Antenna, transmitting and receiving microwave signals
    - Broadband Horn Antenna 2.0-18.0 GHz: A-INFOMV LB-20180-SF
3. DC power supply, providing the multi-level DC power supply
    - Dual output DC power supply: Agilent E3648A
4. Matlab: signal processing and simulation tools
    - Matlab: Mathworks Matlab 2016b

These experimental equipments are already available in the laboratory.

REFERENCES

[1] U. Morbiducci, L. Scalise, M. De Melis, and M. Grigioni, "Optical vibrocardiography: a novel tool for the optical monitoring of cardiac activity," *Annals of biomedical engineering*, vol. 35, no. 1, pp. 45–58, 2007.

[2] L. Scalise and U. Morbiducci, "Non-contact cardiac monitoring from carotid artery using optical vibrocardiography," *Medical engineering & physics*, vol. 30, no. 4, pp. 490–497, 2008.

[3] K.-M. Chen, Y. Huang, J. Zhang, and A. Norman, "Microwave life-detection systems for searching human subjects under earthquake rubble or behind barrier," *IEEE transactions on biomedical engineering*, vol. 47, no. 1, pp. 105–114, 2000.

[4] C. Gu, C. Li, J. Lin, J. Long, J. Huangfu, and L. Ran, "Instrument-based noncontact doppler radar vital sign detection system using heterodyne digital quadrature demodulation architecture," *IEEE Transactions on Instrumentation and Measurement*, vol. 59, no. 6, pp. 1580–1588, 2010.

[5] C. Li, J. Ling, J. Li, and J. Lin, "Accurate doppler radar noncontact vital sign detection using the relax algorithm," *IEEE Transactions on Instrumentation and Measurement*, vol. 59, no. 3, pp. 687–695, 2010.

[6] L. Liu and S. Liu, "Remote detection of human vital sign with stepped-frequency continuous wave radar," *IEEE journal of selected topics in applied earth observations and remote sensing*, vol. 7, no. 3, pp. 775–782, 2014.

[7] O. Postolache, P. S. Girão, R. N. Madeira, and G. Postolache, "Microwave fmcw doppler radar implementation for in-house pervasive health care system," in *Medical Measurements and Applications Proceedings (MeMeA), 2010 IEEE International Workshop on*, IEEE, 2010, pp. 47–52.

[8] G. Wang, C. Gu, T. Inoue, and C. Li, "Hybrid fmcw-interferometry radar system in the 5.8 ghz ism band for indoor precise position and motion detection," in *Microwave Symposium Digest (IMS), 2013 IEEE MTT-S International*, IEEE, 2013, pp. 1–4.

[9] A Lazaro, D Girbau, R Villarino, and A Ramos, "Vital signs monitoring using impulse based uwb signal," in *Microwave Conference (EuMC), 2011 41st European*, IEEE, 2011, pp. 135–138.

[10] L. Chioukh, H. Boutayeb, D. Deslandes, and K. Wu, "Noise and sensitivity of harmonic radar architecture for remote sensing and detection of vital signs," *IEEE*

Transactions on Microwave Theory and Techniques, vol. 62, no. 9, pp. 1847–1855, 2014.

[11] C. Li, Z. Peng, T.-Y. Huang, T. Fan, F.-K. Wang, T.-S. Horng, J.-M. Muñoz-Ferreras, R. Gómez-García, L. Ran, and J. Lin, "A review on recent progress of portable short-range noncontact microwave radar systems," *IEEE Transactions on Microwave Theory and Techniques*, vol. 65, no. 5, pp. 1692–1706, 2017.

[12] C. Li, J. Cummings, J. Lam, E. Graves, and W. Wu, "Radar remote monitoring of vital signs," *IEEE Microwave Magazine*, vol. 10, no. 1, pp. 47–56, 2009.

[13] A. Droitcour, V. Lubecke, J. Lin, and O. Boric-Lubecke, "A microwave radio for doppler radar sensing of vital signs," in *Microwave Symposium Digest, 2001 IEEE MTT-S International*, IEEE, vol. 1, 2001, pp. 175–178.

[14] A. D. Droitcour et al., "Non-contact measurement of heart and respiration rates with a single-chip microwave doppler radar," PhD thesis, Citeseer, 2006.

[15] A. D. Droitcour, O. Boric-Lubecke, V. M. Lubecke, J. Lin, and G. T. Kovacs, "Range correlation and i/q performance benefits in single-chip silicon doppler radars for noncontact cardiopulmonary monitoring," *IEEE Transactions on Microwave Theory and Techniques*, vol. 52, no. 3, pp. 838–848, 2004.

[16] Y. Xiao, J. Lin, O. Boric-Lubecke, and M Lubecke, "Frequency-tuning technique for remote detection of heartbeat and respiration using low-power double-sideband transmission in the ka-band," *IEEE Transactions on Microwave Theory and Techniques*, vol. 54, no. 5, pp. 2023–2032, 2006.

[17] C. Li and J. Lin, "Complex signal demodulation and random body movement cancellation techniques for non-contact vital sign detection," in *Microwave Symposium Digest, 2008 IEEE MTT-S International*, IEEE, 2008, pp. 567–570.

[18] B.-K. Park, O. Boric-Lubecke, and V. M. Lubecke, "Arctangent demodulation with dc offset compensation in quadrature doppler radar receiver systems," *IEEE transactions on Microwave theory and techniques*, vol. 55, no. 5, pp. 1073–1079, 2007.

[19] Y. Hong, S.-G. Kim, B.-H. Kim, S.-J. Ha, H.-J. Lee, G.-H. Yun, and J.-G. Yook, "Noncontact proximity vital sign sensor based on pll for sensitivity enhancement," *IEEE transactions on biomedical circuits and systems*, vol. 8, no. 4, pp. 584–593, 2014.

[20] S. W. Kim, S. B. Choi, Y.-J. An, B.-H. Kim, D. W. Kim, and J.-G. Yook, "Heart rate detection during sleep using a flexible rf resonator and injection-locked pll sensor," *IEEE Transactions on Biomedical Engineering*, vol. 62, no. 11, pp. 2568–2575, 2015.

[21] H.-R. Chuang, H.-C. Kuo, F.-L. Lin, T.-H. Huang, C.-S. Kuo, and Y.-W. Ou, "60-ghz millimeter-wave life detection system (mlds) for noncontact human vital-signal monitoring," *IEEE Sensors Journal*, vol. 12, no. 3, pp. 602–609, 2012.

[22] T.-H. Tsai, B.-Y. Shiu, C.-L. Ho, and J. Lin, "A vital sign radar receiver with integrated a/d converter and dynamic clutter cancellation," in *Radio-Frequency Integration Technology (RFIT), 2016 IEEE International Symposium on*, IEEE, 2016, pp. 1–3.

[23] J.-M. Muñoz-Ferreras, G. Wang, C. Li, and R. Gómez-García, "Mitigation of stationary clutter in vital-sign-monitoring linear-frequency-modulated continuous-wave radars," *IET Radar, Sonar & Navigation*, vol. 9, no. 2, pp. 138–144, 2015.

[24] H.-R. Chuang, Y. Chen, and K.-M. Chen, "Automatic clutter-canceler for microwave life-detection systems," *IEEE Transactions on Instrumentation and Measurement*, vol. 40, no. 4, pp. 747–750, 1991.

[25] J. L. Geisheimer and E. F. Greneker, "Applications of neural networks to the radar-cardiogram (rcg)," in *Applications and Science of Computational Intelligence II*, International Society for Optics and Photonics, vol. 3722, 1999, pp. 368–378.

[26] J. Thijs, J Muehlsteff, O Such, R Pinter, R Elfring, and C. Igney, "A comparison of continuous wave doppler radar to impedance cardiography for analysis of mechanical heart activity," in *Engineering in Medicine and Biology Society, 2005. IEEE-EMBS 2005. 27th Annual International Conference of the*, IEEE, 2006, pp. 3482–3485.

[27] S. J. Mazlouman, K. Tavakolian, A. Mahanfar, and B. Kaminska, "Contact-less assessment of in-vivo body signals using microwave doppler radar," in *Biomedical Engineering*, InTech, 2009.

[28] K. Tavakolian, "Characterization and analysis of seismocardiogram for estimation of hemodynamic parameters," PhD thesis, Applied Science: School of Engineering Science, 2010.

[29] F. Khosrow-Khavar, K. Tavakolian, A. P. Blaber, J. M. Zanetti, R. Fazel-Rezai, and C. Menon, "Automatic annotation of seismocardiogram with high-frequency precordial accelerations," *IEEE journal of biomedical and health informatics*, vol. 19, no. 4, pp. 1428–1434, 2015.

[30] C. Yang, S. Tang, and N. Tavassolian, "Utilizing gyroscopes towards the automatic annotation of seismocardiograms," *IEEE Sens. J*, vol. 17, no. 7, pp. 2129–2136, 2017.

[31] G. Shafiq, S. Tatinati, W. T. Ang, and K. C. Veluvolu, "Automatic identification of systolic time intervals in seismocardiogram," *Scientific reports*, vol. 6, p. 37 524, 2016.

[32] F. Khosrow-Khavar, K. Tavakolian, and C. Menon, "Moving toward automatic and standalone delineation of seismocardiogram signal," in *Engineering in Medicine and Biology Society (EMBC), 2015 37th Annual International Conference of the IEEE*, IEEE, 2015, pp. 7163–7166.

[33] A. Laurin, F Khosrow-Khavar, A. Blaber, and K. Tavakolian, "Accurate and consistent automatic seismocardiogram annotation without concurrent ecg," *Physiological measurement*, vol. 37, no. 9, p. 1588, 2016.

[34] F. Khosrow-Khavar, "Automatic and non-invasive delineation of the seismocardiogram signal for the estimation of cardiac time intervals with applications in diastolic timed vibration and early stage hemorrhage detection," PhD thesis, Applied Sciences: School of Engineering Science, 2016.

[35] F. Khosrow-Khavar, K. Tavakolian, A. Blaber, and C. Menon, "Automatic and robust delineation of the fiducial points of the seismocardiogram signal for noninvasive estimation of cardiac time intervals," *IEEE Transactions on Biomedical Engineering*, vol. 64, no. 8, pp. 1701–1710, 2017.

[36] J. Zanetti, M. Poliac, and R. Crow, "Seismocardiography: waveform identification and noise analysis," in *Computers in Cardiology 1991, Proceedings.*, IEEE, 1991, pp. 49–52.

[37] G.-C. Hsieh and J. C. Hung, "Phase-locked loop techniques. a survey," *IEEE Transactions on industrial electronics*, vol. 43, no. 6, pp. 609–615, 1996.

[38] A. Hajimiri, "Noise in phase-locked loops," in *2001 Southwest Symposium on Mixed-Signal Design (Cat. No. 01EX475)*, IEEE, 2001, pp. 1–6.

[39] T. Akiyama, H. Matsuzawa, E. Haraguchi, T. Ando, and Y. Hirano, "Phase stabilized rf reference signal dissemination over optical fiber employing instantaneous frequency control by vco," in *Microwave Symposium Digest (MTT), 2012 IEEE MTT-S International*, IEEE, 2012, pp. 1–3.

[40] D. Sun, Y. Dong, H. Shi, Z. Xia, Z. Liu, S. Wang, W. Xie, and W. Hu, "Distribution of high-stability 100.04 ghz millimeter wave signal over 60 km optical fiber with fast phase-error-correcting capability," *Optics letters*, vol. 39, no. 10, pp. 2849–2852, 2014.

[41] Z. Xia and Y. Zhang, "Bandwidth of non-contact vital sign detection with a noise suppression phase locked loop," in *Nanosensors, Biosensors, and Info-Tech Sensors*

and Systems 2016, International Society for Optics and Photonics, vol. 9802, 2016, p. 980 215.

[42] H. Ashouri and O. T. Inan, "Automatic detection of seismocardiogram sensor misplacement for robust pre-ejection period estimation in unsupervised settings," *IEEE Sensors Journal*, vol. 17, no. 12, pp. 3805–3813, 2017.

[43] P. Castiglioni, A. Faini, G. Parati, and M. Di Rienzo, "Wearable seismocardiography," in *Engineering in Medicine and Biology Society, 2007. EMBS 2007. 29th Annual International Conference of the IEEE*, IEEE, 2007, pp. 3954–3957.

[44] P. Castiglioni, P. Meriggi, F. Rizzo, E. Vaini, A. Faini, G. Parati, G. Merati, and M. Di Rienzo, "Cardiac sounds from a wearable device for sternal seismocardiography," in *Engineering in Medicine and Biology Society, EMBC, 2011 Annual International Conference of the IEEE*, IEEE, 2011, pp. 4283–4286.

[45] C. Yang, S. Tang, and N. Tavassolian, "Utilizing gyroscopes towards the automatic annotation of seismocardiograms," *IEEE Sensors Journal*, vol. 16738, p. 1, 2016.

[46] A. D. Wiens, A. Johnson, and O. T. Inan, "Wearable sensing of cardiac timing intervals from cardiogenic limb vibration signals," *IEEE Sensors Journal*, vol. 17, no. 5, pp. 1463–1470, 2017.

[47] A. Q. Javaid, H. Ashouri, A. Dorier, M. Etemadi, J. A. Heller, S. Roy, and O. T. Inan, "Quantifying and reducing motion artifacts in wearable seismocardiogram measurements during walking to assess left ventricular health," *IEEE Transactions on Biomedical Engineering*, vol. 64, no. 6, pp. 1277–1286, 2017.

[48] K. Tavakolian, A. P. Blaber, B. Ngai, and B. Kaminska, "Estimation of hemodynamic parameters from seismocardiogram," in *Computing in Cardiology, 2010*, IEEE, 2010, pp. 1055–1058.

[49] Z. Xia, A. M. Carek, O. T. Inan, and Y. Zhang, "Comparison of noncontact and accelerometer based cardiogenic chest wall movement signals: a preliminary study," in *38th Annual International Conference of the IEEE Engineering in Medicine and Biology Society*, IEEE, 2016.

[50] M. T. Allen, J. Fahrenberg, R. M. Kelsey, W. R. Lovallo, L. J. Doornen, et al., "Methodological guidelines for impedance cardiography," *Psychophysiology*, vol. 27, no. 1, pp. 1–23, 1990.

[51] Z. Xia, M. M. H. Shandhi, O. T. Inan, and Y. Zhang, "Non-contact sensing of seismocardiogram signals using microwave doppler radar," *IEEE Sensors Journal*, 2018.

[52] M. J. Tadi, T. Koivisto, M. Pänkäälä, A. Paasio, T. Knuutila, M. Teräs, and P. Hänninen, "A new algorithm for segmentation of cardiac quiescent phases and cardiac time intervals using seismocardiography," in *Sixth International Conference on Graphic and Image Processing (ICGIP 2014)*, International Society for Optics and Photonics, vol. 9443, 2015, 94432K.

[53] S. Ivashov, V. Razevig, A. Sheyko, and I. Vasilyev, "Detection of human breathing and heartbeat by remote radar," in *Progress in Electromagnetic Research Symposium*, vol. 2004, 2004.

[54] G. Shafiq, S. Tatinati, and K. C. Veluvolu, "Automatic annotation of peaks in seismocardiogram for systolic time intervals," in *2016 38th Annual International Conference of the IEEE Engineering in Medicine and Biology Society (EMBC)*, IEEE, 2016, pp. 2672–2675.

[55] M. J. Tadi, E. Lehtonen, T. Hurnanen, J. Koskinen, J. Eriksson, M. Pänkäälä, M. Teräs, and T. Koivisto, "A real-time approach for heart rate monitoring using a hilbert transform in seismocardiograms," *Physiological measurement*, vol. 37, no. 11, p. 1885, 2016.

[56] S. Nakagawa and I. C. Cuthill, "Effect size, confidence interval and statistical significance: a practical guide for biologists," *Biological reviews*, vol. 82, no. 4, pp. 591–605, 2007.

[57] M. J. Gardner and D. G. Altman, "Confidence intervals rather than p values: estimation rather than hypothesis testing.," *Br Med J (Clin Res Ed)*, vol. 292, no. 6522, pp. 746–750, 1986.

[58] K. Pandia, O. T. Inan, G. T. Kovacs, and L. Giovangrandi, "Extracting respiratory information from seismocardiogram signals acquired on the chest using a miniature accelerometer," *Physiological measurement*, vol. 33, no. 10, p. 1643, 2012.

[59] Z. Xia and Y. Zhang, "Dual-carrier noncontact vital sign detection with a noise suppression scheme based on phase-locked loop," *IEEE Transactions on Microwave Theory and Techniques*, vol. 64, no. 11, pp. 4003–4011, 2016.

[60] J. Svensson, *High resolution frequency estimation in an fmcw radar application*, 2018.

[61] G. Wang, J.-M. Munoz-Ferreras, C. Gu, C. Li, and R. Gomez-Garcia, "Application of linear-frequency-modulated continuous-wave (lfmcw) radars for tracking of vital signs," *IEEE Transactions on Microwave Theory and Techniques*, vol. 62, no. 6, pp. 1387–1399, 2014.

VITA

Zongyang Xia received the B.S. and M.E. degrees in Electrical Engineering from Shanghai Jiao Tong University, Shanghai, China, in 2011 and 2014, respectively, and the M.S. degree in Electrical and Computer Engineering from Georgia Institute of Technology, Atlanta, GA, USA, in 2014. In the Fall 2014, he started his doctoral program in School of Electrical and Computer Engineering at Georgia Institute of Technology. His research focuses on the remote sensing of cardiac signals using radar system, including the electrical hardware design, RF circuit design, and radar signal processing.

Publications

- **Z. Xia**, M. H. Shandhi, O. T. Inan, and Y. Zhang, The Delineation of Fiducial Points for Non-contact Radar Seismocardiogram Signals without Concurrent ECG, will be submitted to IEEE Journal of Biomedical and Health Informatics.
- Y. Li, **Z. Xia**, and Y. Zhang, Standalone Systolic Profile Detection of non-contact SCG Signal with LSTM Network, IEEE Sensors Journal, accepted, (2019).
- **Z. Xia**, M. H. Shandhi, O. T. Inan, and Y. Zhang, Non-Contact Sensing of Seismocardiogram Signals Using Microwave Doppler Radar, IEEE Sensors Journal, vol.18, no.14, pp.5956-5964 (2018).
- **Z. Xia**, and Y. Zhang, Dual-Carrier Noncontact Vital Sign Detection with a Noise Suppression Scheme Based on Phase Locked loop, IEEE Transactions on Microwave Theory and Techniques, Vol. 64, No.11, pp. 4003-4011 (2016).
- **Z. Xia**, M. H. Shandhi, O. T. Inan, and Y. Zhang, Interference and Removal of Respiration Harmonics on Noncontact Seismocardiogram Signals, 11th International Workshop on Structural Health Monitoring (IWSHM), Stanford, CA (2017).

- **Z. Xia**, and Y. Zhang, Bandwidth of non-contact vital sign detection with a noise suppression phase locked loop, in SPIE Smart Structures and Materials + Nondestructive Evaluation and Health Monitoring, 2016, Las Vegas, NV (2016).

- **Z. Xia**, A. M. Carek, O. T. Inan, and Y. Zhang, Comparison of Noncontact and Accelerometer Based Cardiogenic Chest Wall Movement Signals: A Preliminary Study, 38th Annual IEEE Engineering in Medicine and Biology Conference (EMBC), Orlando, FL (2016).

- M. H. Shandhi, **Z. Xia**, O. T. Inan, and Y. Zhang, Clutter Effect on the Noncontact Seismocardiogram Signals Measured Using Microwave Radars, 11th International Workshop on Structural Health Monitoring (IWSHM), Stanford, CA (2017).

Patents

- Y. Zhang, and **Z. Xia**, Multi-Carrier Noncontact Signal Detection with Noise Suppression Based on a Phase-Locked Loop, U.S. Patent Application 16/060,781, filed December 27, 2018.